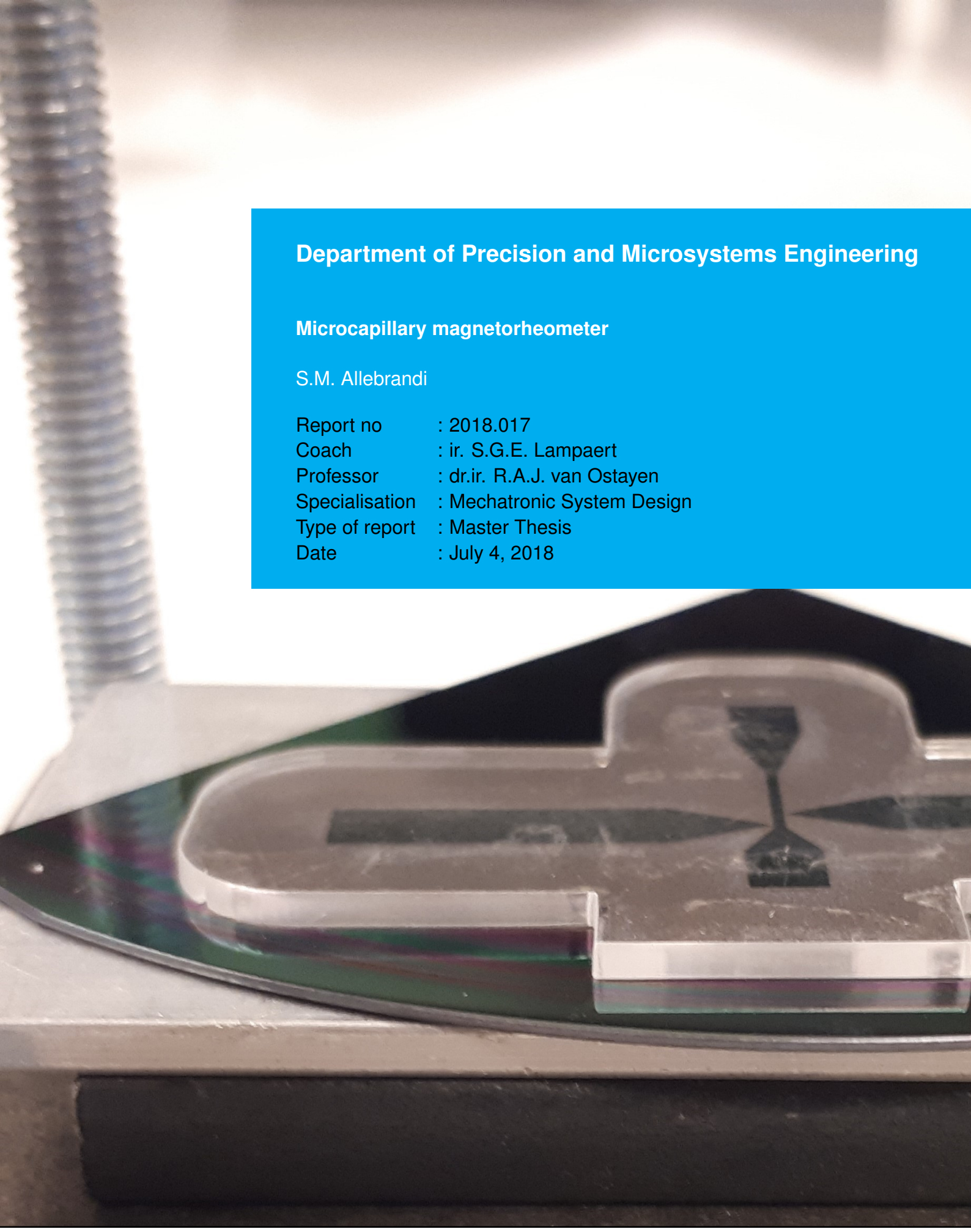

Department of Precision and Microsystems Engineering

Microcapillary magnetorheometer

S.M. Allebrandi

Report no : 2018.017
Coach : ir. S.G.E. Lampaert
Professor : dr.ir. R.A.J. van Ostayen
Specialisation : Mechatronic System Design
Type of report : Master Thesis
Date : July 4, 2018

TU Delft Delft University of Technology

Challenge the future

Microcapillary magnetorheometer

by

S.M. Allebrandi

to obtain the degree of Master of Science

at the Delft University of Technology,

to be defended publicly on Monday July 16, 2018 at 13:45 AM.

Student number:	4161165	
Project duration:	November 1, 2016 – July 16, 2018	
Thesis committee:	ir. S. G. E. Lampaert,	TU Delft, supervisor
	dr. ir. R. A. J. Ostayen,	TU Delft, supervisor
	ir. J. W. Spronck,	TU Delft
	dr. ir. J. F. L. Goosen,	TU Delft
	dr. R. Delfos,	TU Delft

This thesis is confidential and cannot be made public until July 16, 2023.

An electronic version of this thesis is available at `http://repository.tudelft.nl/`.

TU Delft Delft University of Technology

Preface

From a young age I have been driven to understand how things work. From bicycles, to engines, to global warming. This drive for understanding brought me to the TU Delft at Mechanical Engineering, where I was given the tools to start understanding the world even better. I have enjoyed my time in Delft and have learned a lot about myself and what drives me and of course about engineering. The last step of my time in Delft was my thesis project. The dynamic world of magnetorheological fluids has amazed me as well as frustrated me. Through a long thesis where the results were earned through tiresome work and persistence. I am proud of the attained results.

I would like to thank Stefan Lampaert for his support and supervision during the thesis. His ever enthusiastic attitude brought energy to the project and gave me the push I needed. I would also like to thank Ron van Ostayen for his supervision. I would like to thank the lab managers for their support and their quick response to provide me with the materials and the tools I needed. I would like to thank the people from the office for the cheerful atmosphere they created, with record amounts of coffee breaks and walks. Lastly, I would like to thank my parents who have supported me through the entire process.

Sander Allebrandi
Delft, July 2018

List of symbols

Parameter	Definition	Unit
α	Cone angle	rad
A	Area	m^2
β	Viscosity temperature sensitivity	$\Delta\eta/\mathrm{K}$
B	Magnetic field density	T
γ	Surface tension	$\mathrm{N\,m^{-1}}$
γ_{gyr}	Gyromagnetic ratio	$\mathrm{Hz\,T^{-1}}$
$\dot{\gamma}$	Shear rate	$\mathrm{s^{-1}}$
$\dot{\gamma}_{\mathrm{app}}$	Apparent shear rate	$\mathrm{s^{-1}}$
$\dot{\gamma}_{\mathrm{true}}$	True shear rate	$\mathrm{s^{-1}}$
$\dot{\gamma}_{\mathrm{target}}$	Targeted shear rate	$\mathrm{s^{-1}}$
c	Specific heat capacity	$\mathrm{J\,kg^{-1}\,K^{-1}}$
c_s	Speed of sound	$\mathrm{m\,s^{-1}}$
d	Delay	s
d_h	Hydraulic diameter	m
ϵ	Emissivity	-
Φ	Magnetic flux	Wb
f	Frequency	Hz
F	Force	N
$\mathscr{F}$	Magnetomotive force	At
g	gravitational constrant	$\mathrm{m\,s^{-2}}$
h	Gap height	m
h_t	Heat transfer coefficient	$\mathrm{W\,m^{-2}\,K^{-1}}$
H	Magnetic field strength	$\mathrm{A\,m^{-1}}$
η	Viscosity	Pas
I	Current	A
k	Thermal conductivity	$\mathrm{W\,K^{-1}\,m^{-1}}$
K	Loss factor	-
L	Total length	m
L_{e}	Entrance length	m
L_{meas}	Measuring length	m
L_{ex}	Exit length	m
M	Torque	Nm
μ	Friction factor	-
μ_r	Relative permeability	-
μ_0	Magnetic constant	$\mathrm{H\,m^{-1}}$
N	Number of windings	-
Na	Nahme-Griffith number	-

Parameter	Definition	Unit
P	Pressure	Pa
P_{heat}	Power	W
P_{e}	Entrance pressure	Pa
$P_{\mathrm{meas,in}}$	Measurement pressure at inflow	Pa
$P_{\mathrm{meas,out}}$	Measurement pressure at outflow	Pa
P_{ex}	Exit pressure	Pa
Q	Flow rate	$\mathrm{m^3\,s^{-1}}$
r	Radial coordinate	m
R	Radius of the edge	m
R_{e}	Electrical resistance	Ω
$\tilde{R}$	$\tilde{R}$ number	-
R_{in}	Inner radius	m
R_{out}	Outer radius	m
Ra	Rayleigh number	-
R_a	Arithmetic mean	m
Re	Reynolds number	-
$\mathscr{R}$	Reluctance	$\mathrm{H^{-1}}$
ρ	Density	$\mathrm{kg\,m^{-3}}$
σ	Stress	Pa
τ	Shear stress	Pa
T	Temperature	K
Ta	Taylor number	-
U	Voltage	V
u_x	Velocity in x direction	$\mathrm{m\,s^{-1}}$
u_y	Velocity in y direction	$\mathrm{m\,s^{-1}}$
u_z	Velocity in z direction	$\mathrm{m\,s^{-1}}$
ν	Kinematic viscosity	$\mathrm{m^2\,s^{-1}}$
ν_{mean}	Mean velocity	$\mathrm{m\,s^{-1}}$
ν_p	Particle velocity	$\mathrm{m\,s^{-1}}$
V	Velocity	$\mathrm{m\,s^{-1}}$
V_{slip}	Slip velocity	$\mathrm{m\,s^{-1}}$
w	Width	m
ω	Angular velocity	$\mathrm{rad\,s^{-1}}$
x	x coordinate	m
y	y coordinate	m
z	z coordinate	m

Abstract

The viscous behaviour of magnetic fluids at low shear rates (<10^5 s^{-1}) has been extensively discussed in literature. However, little is known about the behaviour at high shear rates(>10^5 s^{-1}), [1]. The behaviour at these shear rates is crucial for improving the performance of industrial applications such as bearings and viscous dampers, [2]. Parallel plate or cone plate rheometers are often used to measure the magnetorheological effect. These concepts have a theoretical shear rate limit of about 10^5 s^{-1}. For example, bearing applications easily reach shear rates above 10^6 s^{-1}, which means that these measurement systems are not suitable to predict the behaviour at the operational range. Therefore, other concepts, such as capillary or concentric cylinder rheometers, should be considered as solutions to reach the high shear rates. This paper presents the design of a capillary magnetorheometer capable of measuring magnetic fluids at shear rates over 10^6 s^{-1} under the influence of a homogeneous magnetic field.

Method

The analysed concepts for achieving high shear rates are: concentric cylinder, parallel plate, cone plate, slit capillary and round capillary. The physical limitations of these concepts identify their maximum performance. The best candidate, taking into account the feasibility of applying a magnetic field, determines the principle used in the design. The concepts are limited by radial migration, secondary flows, turbulence and viscous heating. Figure 1a presents the calculated maximum shear rates of the analysed concepts for a kerosene carrier fluid at a common characteristic gap height of 50 µm.

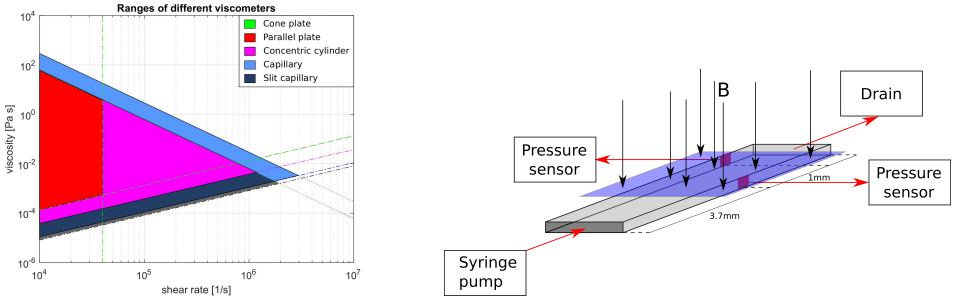

(a) Overlay of the ranges of different rheometer types.

(b) Measuring principle for the rheometer.

Figure 1: Comparison between measuring principle and a sketch of the chosen measurement principle.

Setup

The best performing concepts are capillary devices as they reach high shear rates with a reasonable gap height. Furthermore, their linear design simplifies the application of homogeneous magnetic fields, figure 1b. In addition, the continuous flow of new fluid minimizes the heat developed by viscous heating. A slit capillary prototype is used as rectangular microchannels are relatively simple to manufacture. The chip is made in PMMA through a hot embossing process. The chip is placed in a magnetic core.

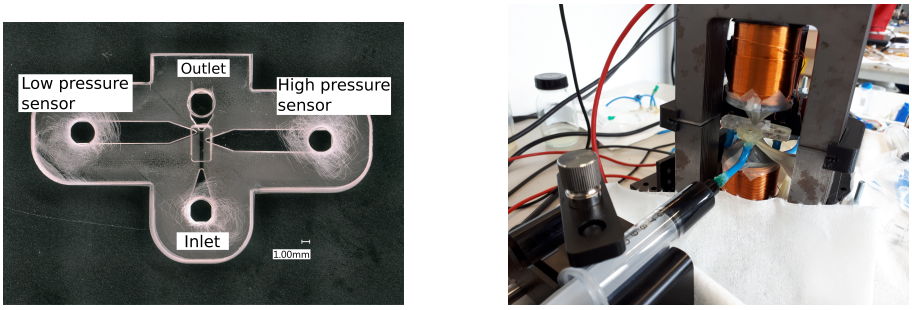

(a) Manufactured chip.

(b) Test setup with the chip in the magnetic core.

Figure 2: The manufactured chip and the test setup.

A produced prototype demonstrates the potential of the designed device. The fluid flows through a 4 mm long microchannel with a gap height of 30 µm. Figures 2a and 2b present the prototype which measures the pressure drop over a 1 mm length. Measurements with deionised water, Shell Tellus VX15 oil and Ferrotec EFH1 validate respectively the maximum shear rate, the accuracy and the ability to measure magnetic fluids.

Results

The deionised water test reached a shear rate of $1.16 \times 10^6\ s^{-1}$ with a maximum deviation of <8% to the estimated viscosity of deionised water, figure 3a. The measurement could not reach higher shear rates due to the stalling of the syringe pump used. Figure 3b presents the measurement with Shell Tellus VX 15 oil. The viscosity is validated using an Anton Paar MCR2 rheometer. The resulting maximum deviation of the prototype for the oil of <8%. Figure 4a presents the measurement with the magnetic fluid showing the magnetorheological behaviour using the Ferrotec EFH1. The graph shows small increases in pressure, thus increases in viscosity, due to the magnetic field.

Conclusions

A high shear rheometer capable of measuring magnetorheological fluids is designed, built and demonstrated. The device measures the viscosity with maximum deviation of 8% over a range of $10^4\ s^{-1}$ to $10^6\ s^{-1}$.

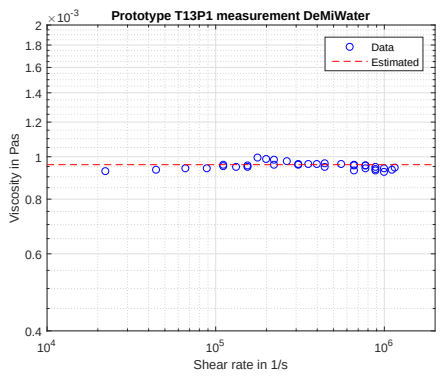

(a) Viscosity of deionized water at high shear rates.

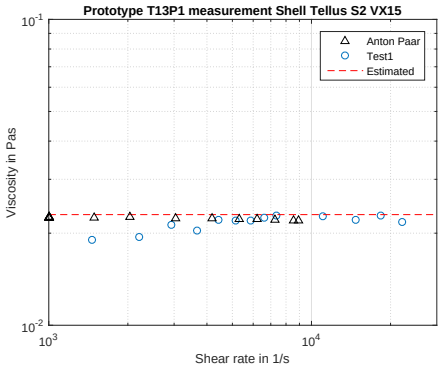

(b) Viscosity of Shell Tellus S2 VX15 at high shear rates.

Figure 3: Measurement results from deionized water and Shell Tellus S2 VX15.

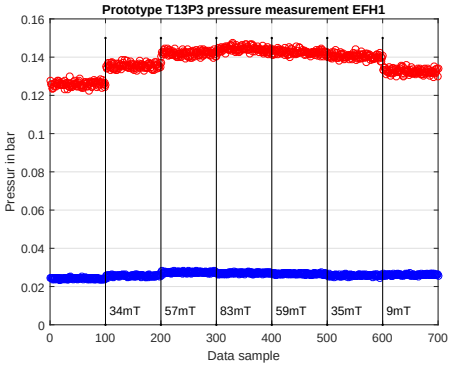

(a) Viscosity of magnetic fluid with different magnetic fields.

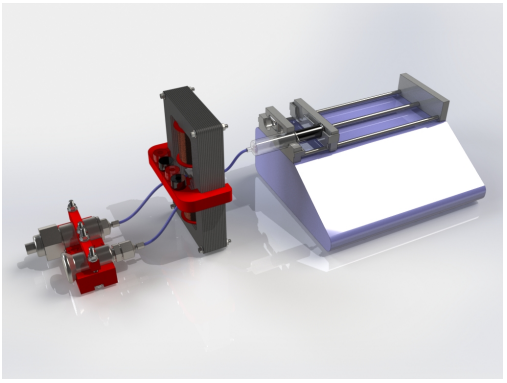

(b) 3D CAD render of total test setup.

Figure 4: Magnetorheological measurement and the test setup design.

Contents

Chapter 1

Project introduction

1.1 Background

In the 1940's magnetorheological fluids, (MR fluid), were first created by Jacob Rabinow. These MR fluids alter their rheological properties significantly under the influence of a magnetic field. The magnetic field changes the viscosity of the MR fluid such that it behaves as a solid if the applied stress is below the induced yield stress. In 1948 J. Rabinow patented the first application of a MR fluid, the MR clutch,[3]. Soon after he patented the MR force transmitter, [4]. The interest in MR fluids died out due to the simultaneous development of the electrorheological fluids, (ER fluid), which were thought to have more potential in industry, however, their breakthrough still remains illusive. The interest in MR fluids returned in the early 1990's. The main benefits of MR fluids compared to ER fluids are the higher yield stress that can be obtained with MR fluids. MR fluids generally have a larger temperature working range and the excitation for ER fluids is in the kiloVolt range while for the MR fluids the excitation is much lower, [5]. From then on the fluid quickly found new applications. Applications such as MR damper [6]. The MR damper was first developed by the Lord Corporation for truck seats and is still being used. The technology was further developed by General Motors in partnership with Delphi corporation to produce dampers for the automotive industry and made its début in production cars from Cadillac as MagneRide in 2002. MR dampers can now be found in high end cars such as Audi and Ferrari,[7]. Further applications such as the MR brake[8] as well as in bearing applications,[[9], [10]] and more,[[2], [5]]. In these systems the fluid flows at high speed however little knowledge is available about what happens to the fluid characteristics at these speeds. More information on the history and properties of MR fluids can be found in appendix C.

1.2 Problem definition

The variety of application has grown, however, the understanding of the fluid is still limited. One research area is the ultra high shear rheometry of MR fluids. This area is of interest as typical shafts and bearings are operating at these shear rates, ($10^5\ s^{-1}$ to $10^7\ s^{-1}$). Therefore the behaviour of MR fluids needs to be characterised at ultra high shear rates. Throughout the academical community a demand for the properties is rising, however, there are no means of measuring these shear rates. The main issue is that the magnetorheometers commercially available are not designed for ultra high shear rates.

These devices are designed to measure a large range of fluids and viscosities. These devices are mostly parallel plate or cone plate devices and have a modular design where inserts can be added to extend the functionality of the rheometer. This means they are limited to shear rates of $10^5\,s^{-1}$ [11], [12]. In the academic community, prior research has reached shear rates up to $10^5\,s^{-1}$ [[13], [1], [14]], however, the ultra high shear rates have not been reached. When focussing on rheometers able to reach ultra high shear rates there are rheometers available reaching shear rates of $10^7\,s^{-1}$. These devices are capillary rheometers [[15],[16]], tapered bearing simulation (TBS),[17] or concentric cylinder rheometers, [18]. However, these lack the ability to apply a magnetic field. For more information on rheometer types, see appendix B. To accommodate the desire from the academic world and to expand the application of MR fluids, a research is performed to design a magnetorheometer. This research focusses on developing a magnetorheometer for MR fluids to measure their viscosity under the influence of magnetic fields at ultra high shear rates. The design must be able to measure a range of shear rates and apply a variable magnetic field. In order to design such a device a literature review has been made to determine the state of the art in rheology. The physical processes and limitations were analysed to determine a working principle. The working principle was chosen while considering the external systems such as the magnetic field. The working principle was developed into a concept together with concepts for the external system. This concept was expanded into a detailed design and finally a proof of principle prototype was built. The research plan can be seen in figure 1.1.

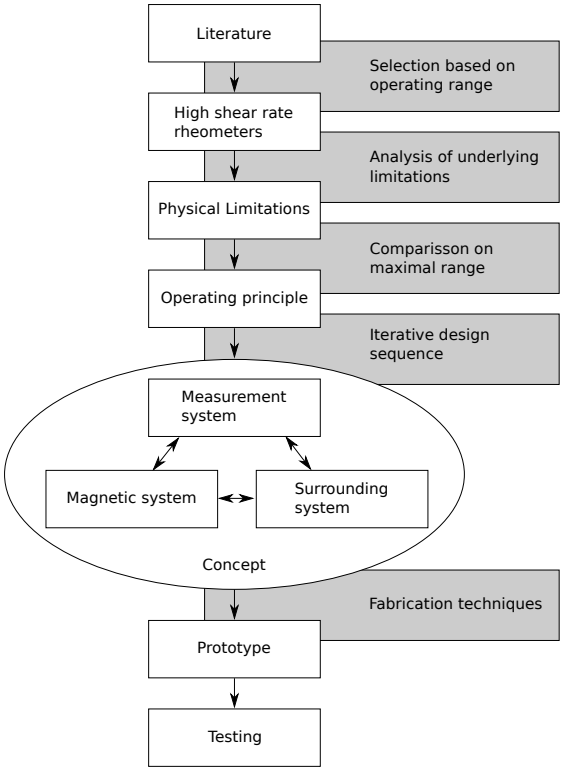

Figure 1.1: Project steps.

1.3 Structure of the thesis

Chapters 2 and 3 show the work done in this research project. Chapter 2 presents a theoretical based analysis of the upper measurement boundaries of different rheometers. A case study is applied to the analysis. Chapter 3 presents the main work done in this thesis. It describes the design, fabrication and testing of the magnetorheometer. These chapters should be seen as two papers which should be understandable for an academic reader without the rest of the thesis. Appendix F presents all the results found in the thesis. These are discussed in chapter 4. The thesis is concluded with recommendations for improvements and future research in chapter 5. In the appendix a short introduction to rheology and the MR fluids can be found, appendix A and C. More details on the design and fabrication can be found in appendices D, E.

Chapter 2

Theoretical boundaries of high shear rheometers

Theoretical boundaries of high shear rheometers

S.M. Allebrandi, S.G.E. Lampaert, R.A.J van Ostayen

July 4, 2018

Abstract

Rheometry is a delicate science. When choosing a rheometer, the main question is: what is the desired measuring range. However, the question should be: what is the measuring range for this specific fluid. Manufacturers of rheometers cannot provide a clear picture of what the range of an accurate measurement is. They merely provide the limitations of their components. Moreover, it is unclear what is limiting the accuracy of the measurement. Knowing what the theoretical limit of an accurate measurement is and what causes the limitation gives the opportunity to improve the measurement and stay within the boundaries of an accurate measurement. A tool is developed to provide a simple estimation of the range of an accurate measurement for different rheometer types. Firstly, the limiting factors of current measurement systems are analysed. These limiting factors are translated into boundary equations. The different devices are connected through a common characteristic length in order to compare them. The devices analysed are: cone plate rheometer, parallel plate rheometer, concentric cylinder rheometer, capillary rheometer and slit rheometer. The tool is applied to a case study to show the applicability. The case study shows that the capillary devices can reach higher shear rates compared to the other rheometers.

2.1 Introduction

Rheological measurements are delicate processes. A slight change in process parameters can alter the result drastically. Especially when measuring near the boundary of the rheometer. In this range the limitations of the measurement are hard to distinguish from the fluid behaviour. For example: the measurement of a shear thinning fluid. As the shear rate increases the viscosity reduces. A similar response is measured when a Newtonian fluid starts to warm up due to viscous heating. When measuring an unfamiliar fluid the measured behaviour can be easily misinterpreted, figure 2.1. There are multiple possible causes for the inaccuracies in viscosity measurements. By analysing the limitations, the causes can be identified and more importantly steps can be taken to extend the accuracy of the measurement. Currently, manufacturers only provide the limitation of the measuring components but do not provide the limitations of an accurate measurement. This causes errors in the resulting viscosities and unrepeatable measurements. No tool is available to easily determine the theoretical working range of a rheometer.

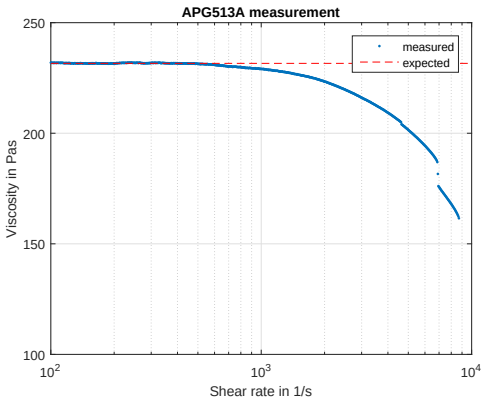

Figure 2.1: Measurement of APG513A crossing over the accurate measurement range.

This paper focusses on a physics based analysis of high shear rheometers, $10^4\,s^{-1}$ to $10^7\,s^{-1}$, to create a tool which derives the measuring ranges of rheometers and compares their performance.

2.2 Method

Firstly, the working principles of current rheometers are analysed. The inaccuracy of measurements originates from the model processing the measurement. These models do not fully incorporate all influences on the viscosity. From the working principles essential model assumptions are defined. By analysing these assumptions, model boundaries and model indicators can be defined. The set of model boundaries create a measuring range of a rheometer type. These ranges are set up for the analysed types of rheometers. Lastly, a characteristic length is used to couple the derived the measuring ranges of the rheometers. An assessment tool is created to a compare the rheometer types. The tool is applied to a case study to show its usefulness in assessing performances of rheometers. The case study used is the definition of a measuring principle for a high shear magnetorheometer.

2.3 High shear rheometers

There are many types of rheometers[1], however, not all of them will be able to reach the high shear rates. Due to the measuring principles and the physics involved the maximum shear rates accurately measurable can be assessed. Firstly the rheometry ranges are defined in 3 ranges which can be seen in table 2.1

Shear range	s^{-1}
Low	10^{-5} - 10^2
High	10^2 - 10^5
Ultra high	$\geq 10^5$

Table 2.1: Shear range definitions

The following rheometers are considered high shear rheometers. The first three devices are rotational rheometers and the last two are pressure driven flows. The geometrical definitions are defined in figure 2.2

1 Cone-plate
2 Parallel plate
3 Concentric cylinder
4 Round capillary
5 Slit capillary

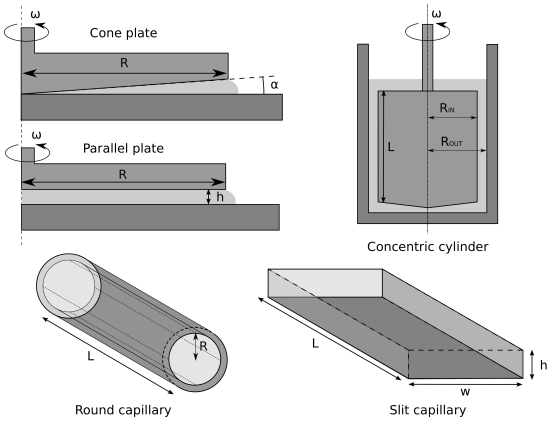

Figure 2.2: Geometrical definitions

2.4 Limitations

The goal of the measuring device is to determine the viscosity. The viscosity is determined by applying a displacement and measuring the force required or vice versa. These are converted through a model into the viscosity. The model assumes the following conditions for the measurement.

1 Unidirectional shear
2 Laminar flow
3 Wall adherence
4 Isothermal flow
5 Incompressible flow

Once the assumptions are untrue, errors enter the measurement. Each model assumption is discussed and its limitation derived.

[1] For information on rheometers and their working principles see appendix B

2.4.1 Unidirectional shear

Unidirectional shear means that no secondary flows are present. At high shear rates the measured fluid is moving at high speed. When the direction of this movement is not linear inertial forces act on the fluid. For example, in a rotational viscometer the fluid has to move in a circular path. The fluid wants to continue in a linear path, however, it must be forced into a rotation. The centrifugal force is countered by a viscous force. As long as this viscous force is dominant over the centrifugal force the flow is unidirectional. However once this is no longer true, the fluid starts moving outwards and unwanted flows occur. This inertial effect is present in all rotational devices, although there is a difference in how the rheometers counteract this inertial effect and thus what range they can measure before the effect dominates the measurement.

(a) Laminar flow (b) Turbulent flow

Figure 2.3: Secondary flow in a cone plate rheometer,[19]

Parallel plate and cone plate

In the case of these rotational devices the flow towards the outside is the first occurring secondary flow. At one plate the fluid will flow from inside to outside and at the other reversed. The secondary flow is initially laminar but can become turbulent. Figures [2.3a,2.3b] visualise the secondary flow. The images are taken from below a cone plate rheometer through a transparent bottom plate with ink being added through a tube into the boundary layer. A dimensionless number can be formed describing the onset of secondary flows, [19].

The secondary flow is characterised by the forces acting on a unit volume. The forces acting on this unit can be evaluated in a steady state in the radial direction. The dimensionless number $\widetilde{R}$ is created to give the ratio of these forces, equations [2.2, 2.3]. The $\widetilde{R}$ number is the Reynolds number in the radial direction.

$$\widetilde{R} = \frac{\text{Inetial forces}}{\text{Viscous forces}} \qquad \widetilde{R} = \frac{\rho\omega^2 r}{\left(\frac{\tau}{h}\right)} \tag{2.1}$$

$$\text{Cone plate:} \quad \widetilde{R} = \frac{\rho\omega^2 r}{\left(\frac{\eta\omega r}{h^2}\right)} = \frac{\rho\omega r^2\alpha^2}{\eta} \tag{2.2}$$

$$\text{Plate plate:} \quad \widetilde{R} = \frac{\rho\omega^2 r}{\left(\frac{\eta\omega r}{h^2}\right)} = \frac{\rho\omega h^2}{\eta} \tag{2.3}$$

When the critical $\widetilde{R}$ number is crossed, secondary flows will start flowing thus increasing the stress in the fluid. More stress measured means a higher measured viscosity. Non-Newtonian fluids will show stranger behaviour as the increased shear stress will alter the viscosity. The critical value of the $\widetilde{R}$ number for cone-plate and parallel plate is 6 according to [19].

At the edges of a cone plate or parallel plate device the forces on the unit volume are different. As these devices have open edges the centrifugal force is countered by the surface tension. There is the possibility that the centrifugal force overcomes the surface tension keeping the fluid between the plates. This phenomenon, known as radial migration, limits the range of the rheometer, [20]. The balance between the surface tension and the inertial forces results in a critical shear rate. This critical shear rate is fluid dependent and strongly dependent on the gap height. The equation for the critical shear rate can be found in equation 2.5,[20].

$$\frac{3}{20}\rho(\omega^2 R^2) > \frac{\gamma}{h} \tag{2.4}$$

$$\dot{\gamma}_{\text{app,c}} = \left(\frac{\omega R}{h}\right)_c = \sqrt{\frac{20\gamma}{3\rho h^3}} \tag{2.5}$$

The result of radial migration can be seen as a drop in measured torque. As there is less fluid the shear stress is reduced. Furthermore a hysteresis effect occurs. Repeating the measurement will result in lower torques measured due to the loss of fluid and thus a lower viscosity is measured.

Concentric cylinder

As with the cone plate and plate plate rheometers, the concentric cylinder is influenced by the centrifugal forces in the fluid. However, due to the fluid being forced into the outside cylinder, the fluid can not be flung out. A rising pressure gradient occurs between the inner and outer cylinder. This balance is not stable and when the rotational speed exceeds a certain point, secondary flows occur. This phenomenon was first studied by Geoffrey Ingram Taylor in 1923. Through dimensionless analysis a quantification of the relation between viscous forces and the inertial forces. He found the critical Taylor number at which Taylor vortices occur, figure 2.4. The Taylor number is defined in equation 2.6, [[21], [22]].

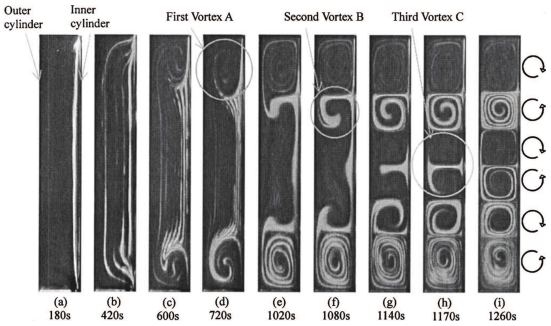

Figure 2.4: Forming process of Taylor vortices of Separan 110ppm, [21]

$$\mathrm{Ta} = \rho^2 \dot{\gamma}^2 \frac{(R_{\mathrm{out}} - R_{\mathrm{in}})^5}{R_{\mathrm{in}} \eta^2} \tag{2.6}$$

When increasing the angular velocity even more different more Taylor vortices occur. The Taylor vortices are initially laminar flows. The increased shearing in the fluid results in a higher torque measured and thus higher viscosities measured. For non-Newtonian fluids the extra shear affects the viscosity in the fluid. The critical Taylor number defines the first occurrence of the vortices and is 1700, [22].

2.4.2 Laminar flow

Laminar flow is required to determine the flow profile. The flow profile is used to determine the shear in the fluid. As the speed of the fluid increases, the laminar flow transitions into turbulent flow. Turbulence occurs due to layers of fluid moving at different speeds. Turbulence has been studied for many types of pipe flow. The capillary devices are pipe flows and therefore are limited to the onset of turbulence. The Reynolds number is used to quantify the balance between inertia forces and the viscous forces. The Reynolds number can be seen in equation 2.7.

$$\mathrm{Re} = \frac{\rho V D}{\eta} \tag{2.7}$$

For the capillary devices the Reynolds equation is transformed in the shape specific equations, equations [2.8, 2.9]. Turbulence creates extra stress in the fluid and chaotic flow. This increases the friction and results in higher viscosities measured. The critical Reynolds number defines the limit of the laminar flow. In literature the true microscale transition to turbulence is still discussed. Studies have found it occurs at Reynolds numbers of 200-500,[23]. The general assumption, concluded from different researches,[24], shows laminar flow below a Reynolds number of 1000 for microchannels.

$$\text{Round capillary:} \quad \mathrm{Re} = \frac{\rho V D}{\eta} = \frac{\rho \dot{\gamma} R^2}{2\eta} \tag{2.8}$$

$$\text{Rectangular capillary:} \quad \mathrm{Re} = \frac{\rho V h}{\eta} = \frac{2\rho \dot{\gamma} w h^2}{6\eta(w+h)} \tag{2.9}$$

Turbulence occurs in the rotational devices as well, although it forms after the instabilities discussed in the previous section. The Reynolds number is proportional to the speed of the fluid. This means turbulence starts occurring at the edges of the rotational devices. This starts as

chaotic flows which can be visualised with aluminium particle visualisation, figure 2.5.

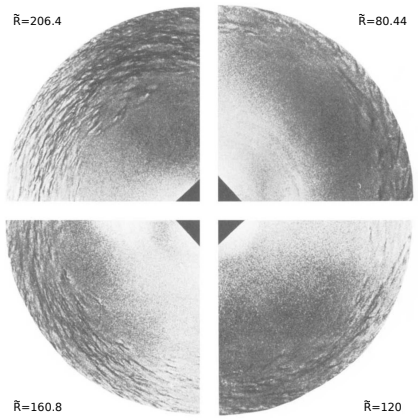

Figure 2.5: Turbulence in cone plate device. Clockwise for increasing $\widetilde{R}$ numbers,[19].

2.4.3 Wall adherence

A key assumption in continuum mechanics is the zero wall slip condition. This condition states that fluid in contact with a wall does not move along the wall. In reality, this is not always true. When the cohesion forces are stronger than the adhesion forces the fluid is pulled along the walls. The viscosity measured is then close to the viscosity of the carrier fluid. When wall slip occurs the flow profile is changed, figure 2.6. The true shear rate is lower than the apparent shear rate the model assumes. Therefore the viscosity is underestimated.

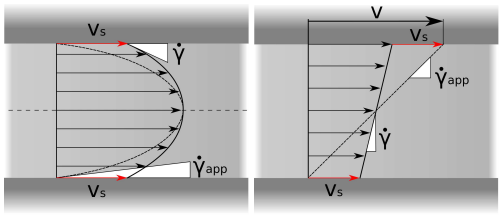

(a) Wall slip pressure driven flow. (b) Wall slip Couette flow.

Figure 2.6: Effect of wall slip on the flow profile. In red the slip velocity.

Depending on the fluid and wall material slip can occur. Slip can also be caused by other factors such as wall depletion. The larger particles are pushed out of the boundary layer. The smaller particles then form a lubricating layer along the walls. The shearing is then mostly applied to the boundary layers, figure 2.7.

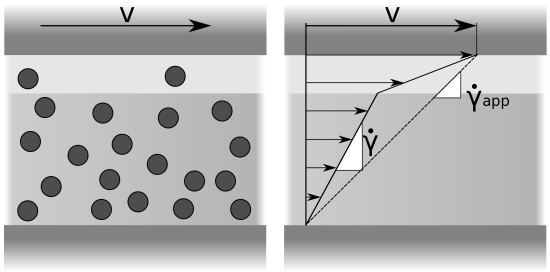

Figure 2.7: Wall depletion in suspensions.

Corrections have been developed since 1931 by Mooney. The Mooney analysis is applicable to all the analysed devises.[25]. The correction uses the data from multiple measurements with different gap heights but equal shear stresses. The flow rate measured is the actual flow rate caused by the viscosity plus the flow rate due to the wall slip. We assume the wall slip is only a function of the shear stress. By looking at the difference in the shear rate relative to the inverse of the characteristic length, we notice the mean velocity due to viscosity is proportional to the gap height. Thus resulting in a horizontal line. The wall slip velocity is only dependent on the shear stress which is constant. The slope of the shear rates at different gap heights with equal shear stress is, therefore, the slip velocity, [26]. Once the slip velocity is known, the true shear rate can be calculated. Equations 2.10 show the derivation for the slit rheometer. Similar analysis can be applied to the other rheometer types.

$$Q = \frac{wh^2\tau}{6\eta} = \frac{6v_{\text{mean}}}{h} \Rightarrow v_{\text{mean}} = \frac{\tau h}{6\eta} \tag{2.10}$$

$$\frac{6v_{\text{mean,true}}}{h} = \frac{6v_{\text{mean,meas}}}{h} - \frac{6v_{\text{slip}}}{h} \tag{2.11}$$

$$\dot{\gamma}_{\text{true}} = \dot{\gamma}_{\text{meas}} - 6\frac{v_s}{h} \tag{2.12}$$

The slip will not be taken into account in the determination of the measuring range as it is fluid and material dependent. Furthermore, current rheometers do not correct for wall slip.

2.4.4 Isothermal flow

Viscosity is strongly temperature dependent. Most rheometers are temperature controlled to measure this temperature dependence. As the shear rates increase more energy is put into the fluid. Part of this energy is converted into heat. This heat is dissipated through the fluid and eventually to the outside world or absorbed by the fluid increasing the fluid temperature. As the viscosity of a fluid is temperature dependent the heating of the fluid must be avoided. When the temperature starts influencing the viscosity the momentum equation of the Navier-Stokes equation becomes coupled to the energy equation making the prediction of the fluid flow complicated. An indicator for the significance of the heating of the fluid is given by the dimensionless Nahme-Griffith number. This number is the ratio between heat generation inside the fluid over the dissipation of the heat. As long as more heat is dissipated than generated due to viscous friction the effect is negligible. The Nahme-Griffith number is closely related to the Brinkman number which is used to quantify the effect a certain temperature change has on the viscosity. The formulas for the Nahme-Griffith number of the different rheometers types can be found in table 2.2.

Rheometer	**Nahme-Griffith**
	Na=
Cone plate	$\frac{\eta\beta(R\tan(\alpha))^2\dot{\gamma}^2}{k}$
Parallel plate	$\frac{\eta\beta h^2\dot{\gamma}^2}{k}$
Concentric cylinder	$\frac{\eta\beta(R_{\text{out}}-R_{\text{in}})^2\dot{\gamma}^2}{k}$
Slit capillary	$\frac{\eta\beta h^2\dot{\gamma}^2}{k}$
Round capillary	$\frac{\eta\beta R^2\dot{\gamma}^2}{4k}$

Table 2.2: Table showing the Nahme-Griffith number for different types of rheometers.[27]

When viscous heating is present, the viscosity is locally lowered. The measured viscosity is therefore reduced. The critical Nahme number is set to 1. In literature, a Nahme number of 1 is seen as the limit, however, the assumption of the wall temperature being equal to the fluid temperature is still adequate, [28].

2.4.5 Incompressible flow

The incompressibility of the fluid flow is crucial as in the model the density is not a function of the pressure. If this was the case the model would assume the incorrect volume flow through the system. Most fluids can be considered incompressible. Furthermore, the viscosity is assumed independent of the pressure. In reality, the pressure does influences the viscosity, however, this is limited. For most liquids the change due to pressure over a range from 0.1 MPa to 30 MPa has the same influence as a temperature change of 1 °C. This can therefore be neglected.

2.4.6 Pressure/speed limits

The system requires sensors. These sensors have their limitations as well. For example, a torque sensor will have a minimum torque and a maximum torque it can measure. The same is valid for a pressure sensor. The maximum torque that can be measured is converted in a maximum shear stress measurable. This maximum shear stress is then converted into a maximum viscosity at a given shear rate, resulting in the boundary of the measurement. The same is done for the lower limit. In the same way as the sensors are limited, the actuation is limited. For example the rotational speed cannot be infinitely low or infinitely high. These limitations create operation boundaries. Table 2.3 presents the limitation equations of the analysed devices.

Rheometer	Sensor	Actuation
	$\eta =$	$\dot{\gamma} =$
Cone plate	$\frac{3M}{\dot{\gamma}\pi R^3}$	$\frac{\omega R}{R\tan(\alpha)}$
Parallel plate	$\frac{2M}{\dot{\gamma}\pi R^3}$	$\frac{\omega R}{h}$
Concentric cylinder	$\frac{M}{\dot{\gamma}\pi R^2 L}$	$\frac{\omega(R_{\text{in}}+R_{\text{out}})}{2(R_{\text{out}}-R_{\text{in}})}$
Slit capillary	$\frac{wh}{2\dot{\gamma}(w+h)}\frac{\Delta P}{L}$	$\frac{6Q}{wh^2}$
Round capillary	$\frac{R}{2\dot{\gamma}}\frac{\Delta P}{L}$	$\frac{4Q}{\pi R^3}$

Table 2.3: Sensor and actuation boundaries.

2.5 Comparison

Taking into account all the discussed limitations in the previous section, the working area of the measurement principles can be predicted. This gives the ability to determine the working range of different rheometer types. The free geometrical variables are listed in table 2.4.

Device	Variable
Cone-plate	α R
Parallel plate	h R
Concentric cylinder	R_{in} R_{out} L
Slit capillary	h w L
Round capillary	R L

Table 2.4: Variables in de measurement systems.

The goal of the analysis is to compare the working principles to make a choice for the best design in a specific case. Therefore the devices have to be linked together. A way to do this is to match a characteristic dimension. In this case the characteristic length should be related to the shearing of the fluid. A re-occurring parameter in table 2.4 is the gap height. By linking the height of the gap, a link is made between the devices on the space where the shearing takes place.
The gap heights of the parallel plate, concentric cylinder and the slit capillary can be matched. This leaves the round capillary and the cone-plate rheometers. The round capillary can be matched with the slit capillary through the hydraulic diameter, equation 2.13. The cone-plate is linked by having the height at the edge of the cone be equal to the gap height. The radii will be matched as well.

$$d_h = \frac{4 \times \text{Cross sectional area}}{\text{Wetted perimeter}} = \frac{2wh}{w+h} \tag{2.13}$$

2.6 Case study

The limitations derived in the previous sections together with the linking characteristic dimension define the boundaries of the measurement systems. These equations are combined into a prediction tool which depicts the measuring ranges. The tool is applied to a case study to demonstrate its benefits and its use.

Case study The use of the derived system of equation is illustrated with a case study. The goal of the case study is to find the best suited measuring principle for magnetorheological fluids. The magnetorheological fluid has a kerosene base and needs to be measured at high shear rates, $10^6\,\text{s}^{-1}$. The gap height is taken as $50\,\mu\text{m}$.

Variables

Firstly, the remaining parameters from table 2.4 have to be defined. The values are taken from commercial rheometers, 2.5. The fluid being used is a kerosene based magnetorheological fluid. Therefore the properties of kerosene are used. Kerosene has a density of $1.07 \times 10^3\,\text{kg}\,\text{m}^{-3}$, thermal conductivity of $0.15\,\text{W}\,\text{K}^{-1}\,\text{m}^{-1}$, surface tension of $32\,\text{mN}\,\text{m}^{-1}$ and a sensitivity of $0.01\,\Delta\eta/\text{K}$.

Variable	Value
Cone radius	15 mm
Plate radius	15 mm
CC radius	15 mm

Table 2.5: Rheometer parameters.

2.6.1 Results

As an example the measuring range is calculated for a slit rheometer measuring kerosene, figure 2.8, with measuring length: 1 mm, gap height: 50 µm, width: 0.5 mm, maximum pressure: 40 bar, minimum pressure: 0.1 bar, maximum flow rate: 25 mL min^{-1} and minimum flow rate: 100 µL min^{-1}.

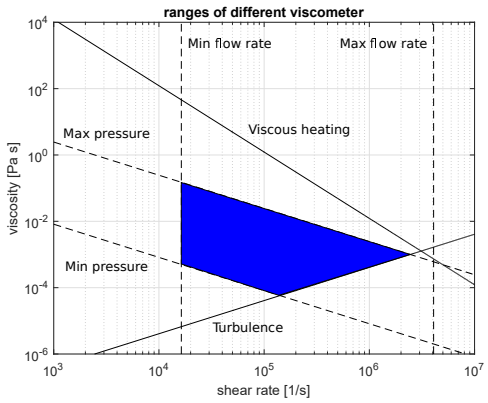

Figure 2.8: Example of the measuring range for a slit rheometer.

Results case study

The figures [2.9, 2.10, 2.11, 2.12, 2.13] show the working ranges. Where the coloured part is the valid measuring range.

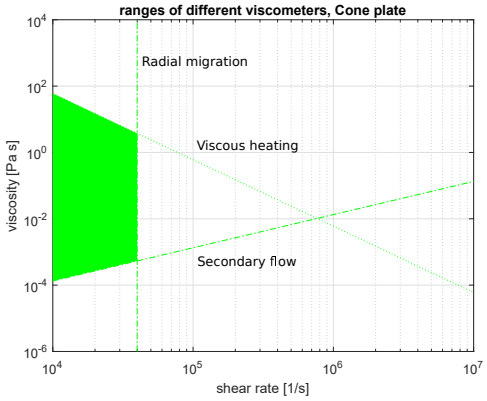

Figure 2.9: Working range cone plate rheometer

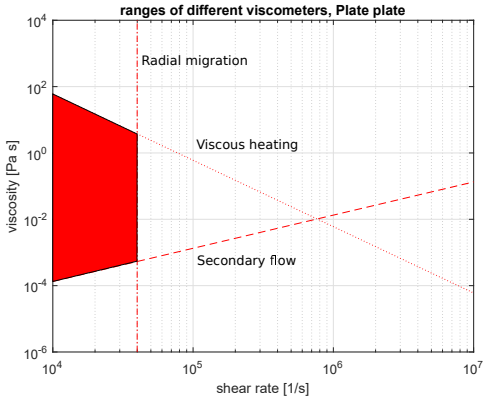

Figure 2.10: Working range parallel plate rheometer

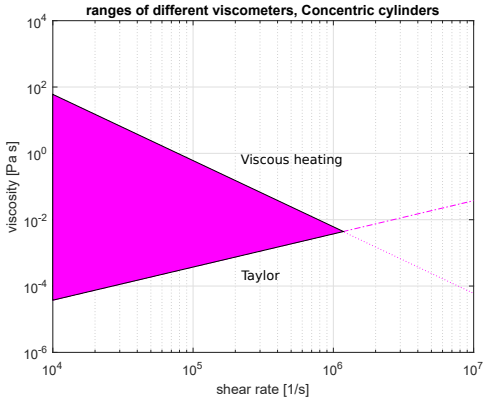

Figure 2.11: Working range concentric cylinder rheometer

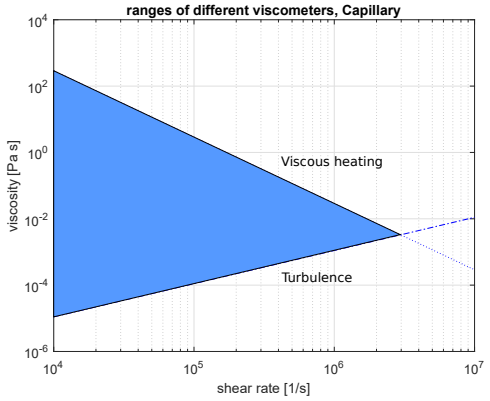

Figure 2.12: Working range capillary rheometer

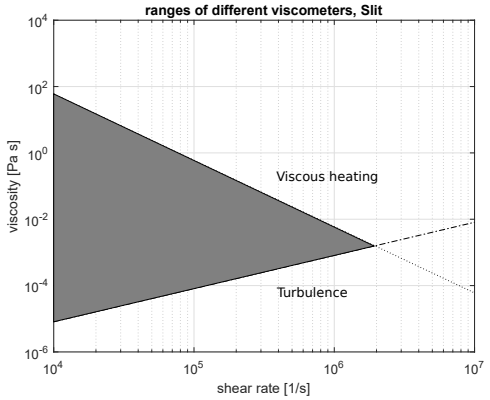

Figure 2.13: Working range slit rheometer

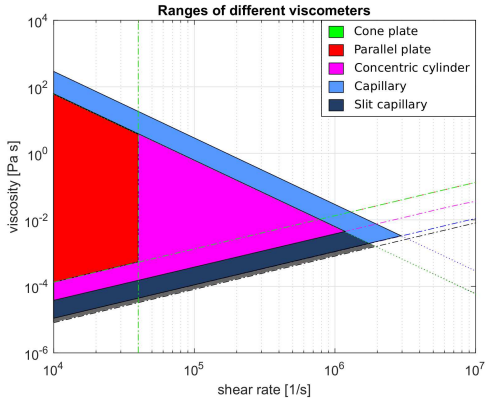

Figure 2.14: Overlay of the ranges of different rheometer types.

An overlay is made of the different ranges to give an impression of the best device for the case study, figure 2.14.

2.7 Discussion

The tool introduced uses limitations related to assumptions in the models for calculating the viscosity in the discussed rheometers. The limitations are taken from papers describing these effects on the rheometers. These descriptions have been adjusted to the other rheometers. The descriptions have been converted into the variables shear rate and viscosity to create the shear ranges.

2.7.1 Dimensionless numbers

The critical values for dimensionless parameters have been taken for the thin film situation. The $\widetilde{R}$ value has been taken from [19] which describes cone-plate systems. The assumption has been made that this value is equally valid for parallel plate rheometers. In literature various descriptions were found for the Taylor number. The used description is mostly applied to large gaps. The case study uses a small gap. Therefore, a description for thin gap Couette flow will describe the limit more accurate. The Reynolds number for the capillary rheometers has been given the maximum value of 1000 from [24]. The last dimensionless number is the Nahme number. The limiting value of this parameter is not clearly defined. Depending on the conductivity of the surrounding material and the heat transfer at the walls, the viscous heating could start at lower shear rates. However, the limit is equally limiting for each rheometer type and therefore does not have an influence on the comparison between the rheometers. It does have an influence on the range of the rheometers. Preferably the Nahme number should be kept below 1. Nahme numbers of $\mathcal{O}(1)$ are seen as adequate, [28].

2.7.2 Predicted ranges

The predicted ranges give an estimation of the limitations. The measuring ranges provide insight into where the limitation of a measurement lie in order to improve the system and avoid inaccurate measurements. Further research into the lower boundaries would give a full description of the measuring range.

2.7.3 Common gap height

The common gap height links the different rheometer types. This characteristic length has been chosen as it is a crucial parameter in the discussed limitations. Furthermore, the gap height is the main component in the definition of the shear rate and thus viscosity and is the main variable in all the dimensionless numbers.

2.7.4 Case study

The case study describes the design problem of chapter 3. Figure 2.14 gives a prediction of the measuring ranges for kerosene for the different rheometers with a common gap height of 50 µm. The graph shows that the capillary devices have a higher measuring range compared to the other rheometers. Therefore, the measuring principle for the magnetorheometer should be a capillary device.

2.7.5 Tool

This insight gives information on how to improve the measurement. Furthermore, the tool developed is useful for the untrained rheologist performing high shear measurements. When a rheologist uses a device with an unfamiliar fluid, he can use the tool to estimate the range, figure 2.8. With these limitations the rheologist can make sure he performs an accurate measurement.

2.8 Conclusion

The tool provides a simple overview of the performance of different rheometers. The tool shows an estimate of the maximum ranges. Using the common characteristic length, the rheometers can be compared. The tool provides insight into what is limiting the performance of a measurement and thus provides the opportunity to improve the measurement. The case study concluded that the capillary rheometers are able to reach higher shear rates.

2.9 Recommendations

Firstly, the tool should be fully tested. The limitations used are known quantities from literature. However, the accuracy of the tool should be tested. Furthermore, the limitations provided give the upper boundaries. The tool could be extended to give the lower boundaries as well. This would provide a full view of the measurement range of a rheometer for a chosen fluid.

Chapter 3

Capillary Rheometer for Magnetorheological Fluids

Capillary Rheometer for Magnetorheological Fluids

S.M. Allebrandi, S.G.E. Lampaert, R.A.J van Ostayen

July 4, 2018

Abstract

Magnetorheological fluids, (MR fluids) have been around since the 1940's. After their discovery many applications followed, such as the MR clutch and MR damper. In these applications the fluids are subjected to ultra high shear rates although no knowledge is available on what happens to the rheological properties under these conditions. In general, the characteristics determined on lower shear rates are extrapolated and used to design new devices. MR fluids have potential in the high tech and high precision applications and their properties need to be known in particular at shear rates around $10^6\,\mathrm{s}^{-1}$*. Commercially available magnetorheometers are not able to measure these fluids at ultra high shear rates and are limited to* $10^5\,\mathrm{s}^{-1}$*. Therefore a new magnetorheometer is required to measure ultra high shear rates. In this paper the physical limitations of current measuring principles are analysed and a concept is designed for ultra high shear rate rheometry in combination with a magnetic field. A prototype is fabricated and the techniques used are described. The prototype is tested and compared to a state of the art commercial rheometer. The test results of the prototype rheometer for MR fluids show its capability to measure fluids to a range of* $10^4\,\mathrm{s}^{-1}$ *to* $1.16\times10^6\,\mathrm{s}^{-1}$ *and the capability to measure the magnetorheological effect of magnetic fluids.*

3.1 Introduction

In the 1940's magnetorheological fluids, (MR fluid), were first created by Jacob Rabinow. These MR fluids alter their rheological properties,(viscosity), significantly under the influence of a magnetic field. In 1948 J. Rabinow patented the first application of a MR fluid, the MR clutch,[3]. Soon after he patented the MR force transmitter, [4]. From then on the fluid quickly found new applications. Applications such as magneto rheological damper [6], MR brake[8] as well as in bearing applications,[[9][10]] and more, [[2], [5]]. In these systems the fluid flows at high speed, though little knowledge is available about what happens to the fluid characteristics at these speeds. Prior research has reached shear rates up to $10^5\,\mathrm{s}^{-1}$, [[1], [13], [14]].

Commercial rheometers are not designed for high shear rates but to measure a large range of fluids and viscosities. These devices are mostly parallel plate or cone plate devices and have a modular design where inserts can be added to extend the functionality of the rheometer. However, they are limited in shear rate. Existing commercial equipment reaches $10^5\,\mathrm{s}^{-1}$ [11],[12]. There are rheometers available reaching shear rates up to $10^7\,\mathrm{s}^{-1}$. These are capillary rheometers [[15],[16]], tapered bearing simulation (TBS),[17] or concentric cylinder rheometers, [18]. However, these lack the ability to apply a magnetic field. Therefore there is a need for a new apparatus which is capable of reaching shear rates in the range of bearings and damper and is able to apply a magnetic field.

This paper focusses on the design of a magnetorheometer capable of measuring MR fluids to a shear rate of $10^6\,\mathrm{s}^{-1}$ under the influence of a homogeneous magnetic field of 1 T.

3.2 Method

Firstly, the current commercially available and research magnetorheometers are analysed. Secondly, the non-magnetorheometers are analysed for their characteristics in order to determine the requirements for a new rheometer. The requirements can be found in table 3.1.

Shear rate	10^6	s^{-1}
Magnetic field density	1	T
Repeatability	2	%
Accuracy	2	%

Table 3.1: Requirements

The physical principles used in the rheometers are determined and the theoretical working ranges set out. By linking a common characteristic length scale, a comparison can be made between the working principles. A measuring principle is selected by calculating the measuring ranges at various gap heights. Extra focus was put into the application of a magnetic field. For the measurement it is crucial that the magnetic field is homogeneous and constant. A concept is designed, a prototype built and tested. To determine the performance of the prototype, the viscosity was measured of 3 different fluids: deionized water, Shell Tellus S2 VX15 hydraulic oil and Ferrotec EFH1. For comparison, the same fluids were measured in a commercial rheometer, Anton Paar MCR 302.

3.3 Analysis

There are four principles for measuring high shear rates:

1 Parallel plate
2 Concentric cylinder
3 Round capillary
4 Slit capillary

The geometrical definition of these rheometer are given in figure 3.1. The cone plate has been left out as it has the same measuring range as the parallel plate, chapter 2. These principles can be linked through the common characteristic of the gap height. The gap height is a critical parameter for magnetorheometers due to the particle size and the chain formation caused by the magnetorheological effect. The round capillary rheometer can be linked to the slit capillary through the hydraulic diameter. The slit capillary can be linked to the parallel plate and concentric cylinder through the gap height.

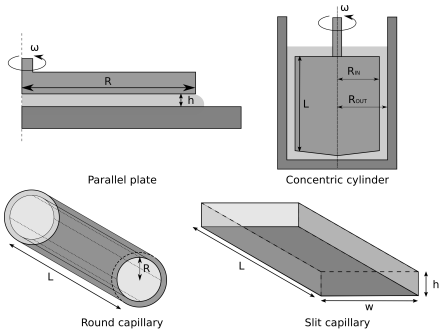

Figure 3.1: Geometrical definitions

3.3.1 Limitations

Each measuring principle is limited by a minimum gap height, turbulence and viscous heating.

Gap height The minimum gap height is a restriction due to the magnetorheological effect as the fluid creates chains which resist the flow, figure 3.2. The particles need sufficient space to form chains. The particle size is in the µm range. Therefore, a minimum gap height of 20 µm is set.

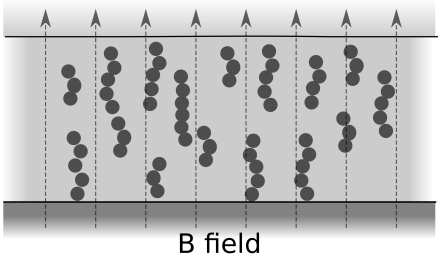

Figure 3.2: Chain formation in MR fluids which increases the viscosity.

Turbulence Turbulence limits the accuracy of the measurement. When the flow becomes turbulent, extra stress is induced in the fluid resulting in more resistance which is not the true viscosity. The limit of this is determined by the Reynolds number of the flow. For the rotational devices the Reynolds number for the radial direction is used. The equations for the Reynolds number can be found in table 3.2.

Temperature As viscosity is temperature dependent, isothermal flow conditions are required during the measurement. The Nahme-Griffith number describes the ratio between the viscous heating and the conductive dissipation. As long as the Nahme number is less than 1 the fluid will not be influenced by viscous heating. The equations for the Nahme number are in table 3.2.

Principle	Reynolds	Nahme
Parallel plate	$\frac{\rho\dot{\gamma}h^3}{R\eta}$	$\frac{\eta\beta h^2\dot{\gamma}^2}{k}$
Concentric C	$\frac{\rho\dot{\gamma}(R_{out}-R_{in})^3}{R_{in}\eta}$	$\frac{\eta\beta(R_{out}-R_{in})^2\dot{\gamma}^2}{k}$
Round capillary	$\frac{\rho\dot{\gamma}R^2}{2\eta}$	$\frac{\eta\beta R^2\dot{\gamma}^2}{4k}$
Slit capillary	$\frac{2\rho\dot{\gamma}wh^2}{6\eta(w+h)}$	$\frac{\eta\beta h^2\dot{\gamma}^2}{k}$

Table 3.2: Limitations, [27].

Taylor vortices The instability related to the centrifugal forces in concentric cylinders are called Taylor vortices. These vortices result in a limiting shear rate as in equation 3.1 for a critical Taylor number of 1700, [22].

$$\mathrm{Ta} = \rho^2\dot{\gamma}^2\frac{(R_{out}-R_{in})^5}{R_{in}\eta^2} \tag{3.1}$$

Shear fracture For the parallel plate an additional limitation occurs. Due to the high rotational speeds, centrifugal forces can pull the fluid from the gap and sling it away. This instability is characterised by equation 3.2, which is rewritten into a critical shear rate, equation 3.3, [20].

$$\frac{3}{20}\rho(\omega^2R^2) > \frac{\gamma}{h} \tag{3.2}$$

$$\dot{\gamma}_{\mathrm{app,c}} = \left(\frac{\omega R}{h}\right)_c = \sqrt{\frac{20\gamma}{3\rho h^3}} \tag{3.3}$$

3.3.2 Comparison

By taking a fixed fluid and a given common characteristic gap height, the working ranges can be calculated. An overlay of the theoretical ranges for a common gap height of 35 µm can be found in figure 3.3. The fluid used in the measuring range is kerosene with the following properties: ρ = 1.07 kg m^{-3}, k=0.15 W K^{-1} m^{-2}, β=0.01 $\Delta\eta$/K. Kerosene is a commonly used carrier for MR fluids.

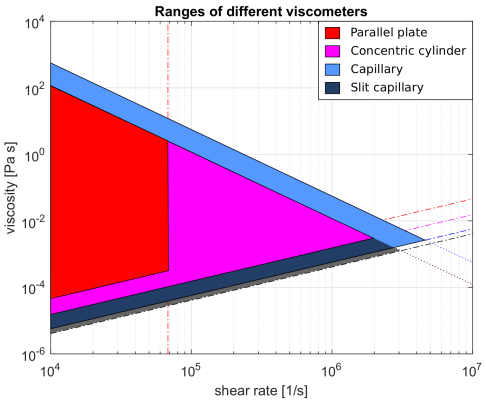

Figure 3.3: Theoretical ranges of the measurement principles for a gap of 35 µm.

From figure 3.3 we can see that the capillary devices have a slight advantage in measurement range. Moreover, in capillary devices are less influenced by viscous heating. The Nahme-Griffith number describes the viscous heating at a specific shear rate. Pressure driven flows have a varying shear rate over their gap, where the shear rate is highest at the edges. For rotational devices the shear rate is constant over the gap, meaning the entire fluid is heating. Additionally, the capillary devices continuously introduces new fluid to the system whereas the rotational devices reuse their

fluid. Lastly, capillary devices have an advantage in the application of a magnetic homogeneous magnetic field due to the linear shape.
The capillary concept, therefore, best fulfils the requirements. The slit capillary concept is chosen as producing rectangular microchannels is more cost effective and can be done more consistently.

3.4 Design

A slit capillary consists of three parts: the entrance length, the measuring length and the exit length.

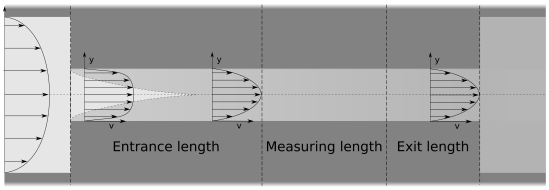

Figure 3.4: Channel design.

The entrance length is needed to create a fully developed flow and should be sufficient for the lowest viscosity fluid targeted. The transition to turbulent flow on macro scale is seen as a Reynolds number of 2300. In literature the transition phase for microfluidics is however still disputed. The consensus is that it does not start before a Reynolds number of a 1000,[24]. To accommodate the fluid entering and stabilising, an entrance length is determined by equation 3.4, [29].

$$\frac{L_e}{d_h} \approx \frac{0.63}{1+0.035\mathrm{Re}_{\max}} + 0.044\mathrm{Re}_{\max} \tag{3.4}$$

The measuring length is set at 1 mm as this creates a measurable pressure drop for low viscosity fluids while not requiring excessive feed pressure for higher viscosity fluids. The exit length is set to 0.2 mm. Increasing the exit length increases the required inlet pressure. However, by extending the exit length the MR fluid can be drained from the channel.

Lastly, the gap height needs to be determined. A lower gap height results in higher shear rates, lower viscous heating and an increase in the required inlet pressure. The goal to measure MR fluids determines the lower limit of the gap height, 20 µm. Through an iterative process of weighing the pressures required to drive the fluid and the heat generation, a gap height of 35 µm was chosen[1]. This results in the following measuring range for kerosene, figure 3.5.

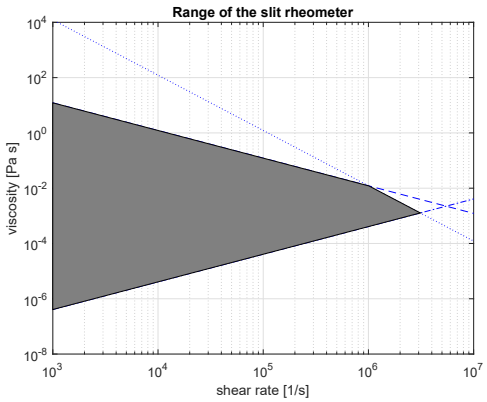

Figure 3.5: Working range of designed rheometer.

The maximum shear stress to be measured is tuned to have a Nahme-Griffith number of 1 at $10^6\ \mathrm{s}^{-1}$ which results in a pressure of 40 bar at the entrance of the channel, equation 3.5.

$$\frac{\Delta P}{\Delta L} = \tau \frac{2(w+h)}{wh} \tag{3.5}$$

The width of the channel has limited effect on the range but determines the flow rate. By tuning the width of the channel, the flow rate is adjusted to combine it with the flow rate of the pump, equation 3.6.

$$Q = \frac{wh^2\dot{\gamma}}{6} \tag{3.6}$$

The magnetic core was designed to apply a field over the microchannel[2]. The choice was made to use a symmetric design to create a homogeneous

[1] For more details see appendix D.1.7
[2] For more details on the magnetic core design see appendix D.2

field. The field has to be concentrated on the small area of the channel. The size was made four times as large as the channel dimensions. The final parameters used can be found in table 3.3.

Parameter	value
Channel height	35 µm
Channel width	500 µm
Entrance length	3.7 mm
Measurement length	1 mm
Exit length	0.2 mm
Inlet pressure	40 bar
Sensor pressure high	9.0 bar
Sensor pressure low	1.5 bar

Table 3.3: Final dimensions

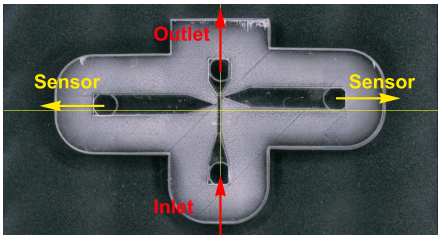

Figure 3.6: Design assembled chip.

The simplest design would be to have the sensors directly next to the channel, however, due to the magnetic core which surrounds the channel, there is limited space for the sensors. Therefore, sensor channels are created for the pressure sensors, figure 3.6. The sensor channels have to be much wider than the channel as not to create significant pressure drop to the sensors.

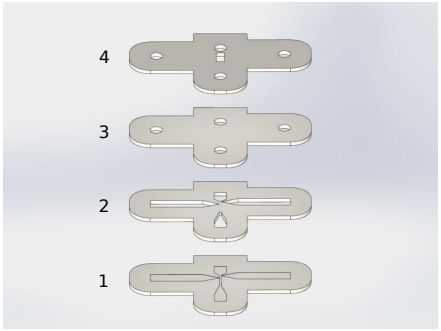

Figure 3.7: Exploded view of chip design in layers.

This results in a multi layered design where in the second layer the sensor channels are cut out. The third layer seals the sensor channels and allows for connectors to be mounted. A forth layer is added to create more connecting length for the connectors and make them more robust. The final design can be seen in figure 3.7 with the layers numbered.

3.5 Prototype

To show the functioning of the designed rheometer, a prototype is designed and manufactured. This prototype should measure a reduced range however still reach the ultra high shear rates. The designed range and the prototype range can be seen in figure 3.8.

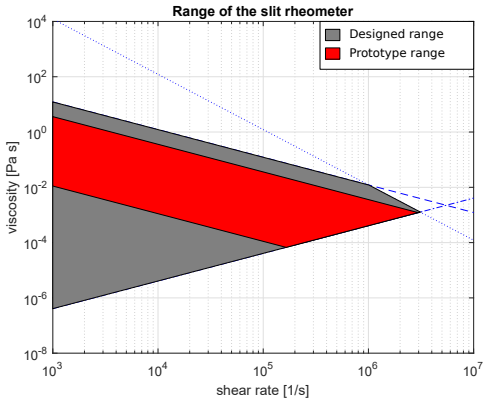

Figure 3.8: Prototype working range.

The range is reduced to ensure lower pressures over the channel. This put lower requirements on the pump and the sensors.

3.6 Fabrication

For the fabrication of the entire device 3 subsystems have to be built. Firstly, the microchannel itself. Secondly, the magnetic system and finally the external systems such as data acquisition and the pump.

3.6.1 Microchannel fabrication

The fabrication of the micro device is complicated. Most micro devices are made through a chemical etching process however this is expensive and time consuming. In microfluidics hot embossing techniques have been developed for quick prototyping. Hot embossing uses a master design to press features into a plastic substrate. This process has been chosen in order to make devices in a cost effective manner. The substrate material chosen is Poly(MethylMethAcrylate), (PMMA). The fabrication process for the chip consists of 5 steps.

1 Master production
2 Hot embossing
3 Flattening
4 Bonding
5 Final assembly

Master production

A laser etching machine is chosen to etch the master design in silicon. The laser is a Spectra Physics Q-switched Talon laser 355-15 with maximum output of 15 W at 50 kHz repetition frequency and with 13 W at 100 kHz. The maximum frequency is 500 kHz with a pulse width of 35 ns. Different laser patterns and rotations have been tested to optimize the height differences created by the laser path. The best result was obtained by laser etching the silicon with a 5 µm line spacing in a net pattern. The etch is repeated once with a 45° rotation of the net etching pattern. A firing rate of 20 kHz with a laser speed of 20 m s^{-1} was used, [30]. The produced master is cleaned in Isopropanol with an ultrasonic cleaner for half an hour, then spincoated with a anti stiction monolayer, EVGNIL ASL for releasing the PMMA after the embossing process, figure 3.9 .

Figure 3.9: Silicon master

Embossing

The master is placed in a mechanical press and covered with a piece of 1 mm thick PMMA cut into the shape of chip design. The PMMA is covered with a silicon wafer to improve the surface roughness of the counter surface.

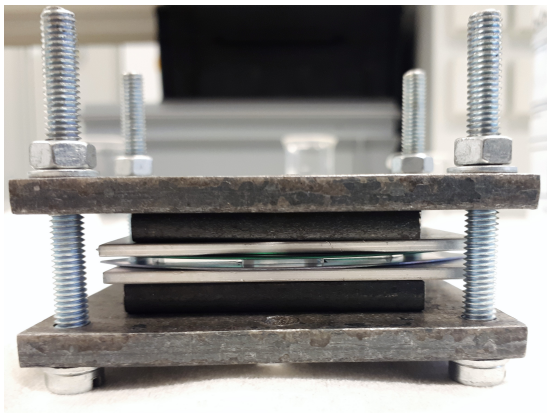

Figure 3.10: Assembled press.

The assembly is clamped between two sheets of aluminium and two cast steel plates and tightened by four bolts, figure 3.10. The bolts are hand tightened and the assembly placed in an oven preheated to 145 °C for 20 minutes. The bolts are then tightened with a torque wrench to an overall pressure of 0.9 MPa. The assembly is left in the oven for 20 minutes, then slowly cooled to 110 °C in about 20 minutes. The pressure is removed

and the press is disassembled. The master is separated from the PMMA and left to cool to room temperature. The temperature and pressure are sketched in figure 3.13 as the solid lines. The embossing procedure is taken from [31] and adapted through trial and error to get the best results for the used equipment. The embossed PMMA can be seen in figure 3.11.

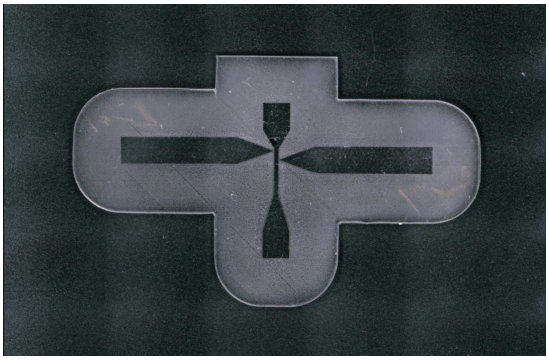

Figure 3.11: Embossed PMMA.

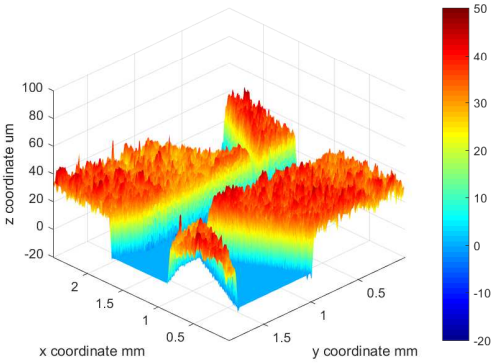

(a) before flattening.

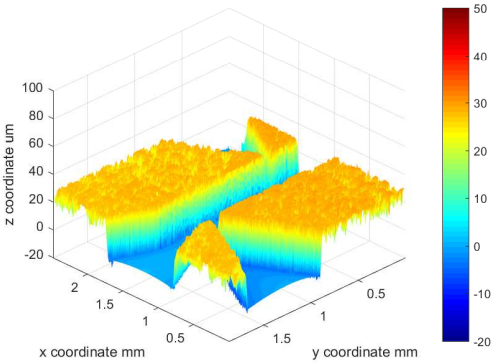

(b) After flattening.

Figure 3.11: White light interferometry images of PMMA surface before and after the flattening process.

Flattening

The uneven surface on the PMMA, due to the laser etched surface, is subjected to flattening stages. As a result of these steps, the bonding is improved and a sealed microchannel is obtained. The PMMA is put in between two layers of silicon and assembled in the press. A pressure of 0.57 MPa is applied. The assembly is put in a preheated oven of 110 °C for 55 minutes and then cooled under pressure to room temperature. The improvement of the bonding surface can be seen in figure 3.11. The flattening process does have an effect on the channel geometry. Due to the temperature and pressure the channel swells slightly.

Bonding

The bonding step is similar to the embossing step but requires a lower temperature to inhibit deformation of the geometry. Layers 2, 3 and 4, figure 3.7, are aligned and assembled in the press. For a smooth counter surface, silicon wafers are placed on either side. The press is tightened to 0.57 MPa and placed in an oven preheated to 110 °C. The assembly is left in the oven for 90 minutes and then slowly cooled to room temperature. The pressure is removed and the press is disassembled.

The bond of the embossed PMMA to the bonded layers 2, 3 and 4, figure 3.7, is done chemically [32]. A solution of 70% Isopropanol is distributed on top of the embossed PMMA. The remaining layers placed on top. The assembly is pressed together and the excess solution is removed. While under slight pressure the layers are aligned using alignment tools. The press is hand tightened and placed in a preheated oven of 68 °C. The press is left for 15 minutes. The press is removed and slowly cooled to room temperature. Once cooled the pressure is removed. The temperature and pressure are sketched in figure 3.13 as the striped lines and dotted lines as thermal bonding and chemical bonding respectively. The final assembled chip can be seen in figure 3.12.

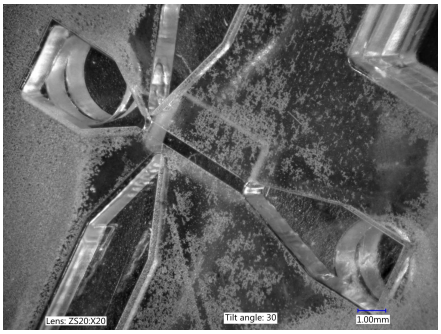

Figure 3.12: The assembled chip.

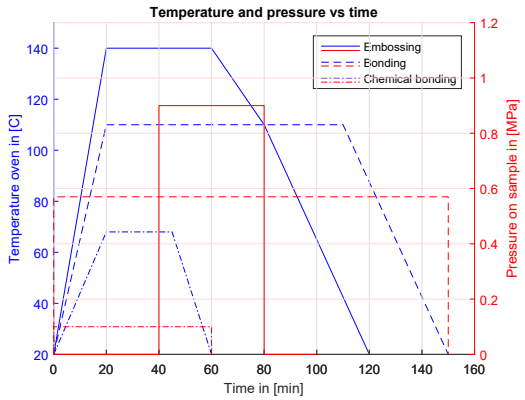

Figure 3.13: Temperature in the oven and pressure on PMMA against time.

3.6.2 Preliminary test

The seal of the microchannel is tested through two simple tests. Firstly the chip is submerged in water for a leak test. Air is pressed into the channel through a syringe. The air bubbles appearing show the flow of air and the leakages, figure 3.14.

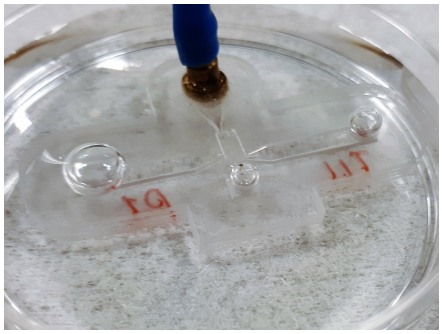

Figure 3.14: Airtest showing bubbles at the connection points and outlet.

In the second test water is pressed into the chip with a syringe. The meniscus moving through the chip can be perceived. Showing that the fluid does not flow in between the layers.

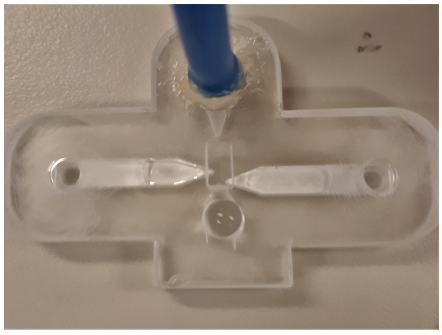

Figure 3.15: Water test.

3.6.3 Magnetic system

A magnetic core has been designed to apply the 1 T field on the microchannel. The core has been fabricated from St37 steel. The core has been designed as a layered design to be able to laser cut

and assemble the core. The coils have a diameter of 300 mm and are wrapped with 400 windings of 0.55 mm diameter magnetic copper wire. The gap is 3 mm to allow for the microchannel to be placed in between. The fabricated core can be seen in figure 3.16.

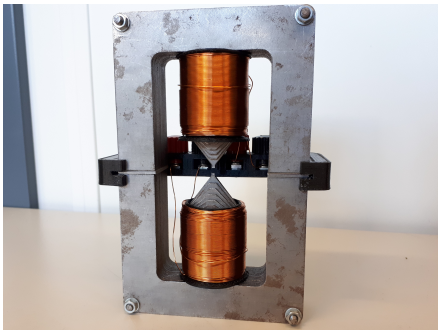

Figure 3.16: Fabricated core.

The magnetic behaviour has been characterised at the location of the microchannel using a Gauss meter. The current has been varied from −3 A to 3 A whilst measuring the magnetic field density.

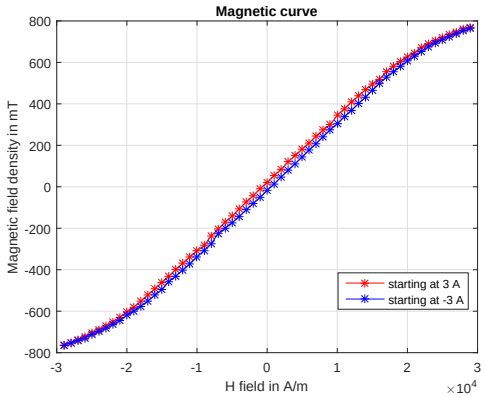

Figure 3.17: Magnetic field curve at microchannel in air.

3.6.4 Final assembly

The PMMA assembly needs to be connected to the hardware used. The connectors are adapted Festo connectors. These have been filed down to 3 mm diameter. The Festo piping connects the PMMA to the pressure sensors and the syringe pump. The connections are glued in place with Bison plastic epoxy

3.6.5 Sensors and data acquisition

The pump being used is a Kd Scientific Legato 111 double syringe programmable infusion and withdrawal pump. The syringe used is a 10 ml plastic Terumo syringe. The pump has a maximum flow rate with this syringe of 25.99 ml per minute which is sufficient to reach shear rates over 10^6 1/s. The sensors used are RS-Pro fluid pressure sensors.

Device	Serial number
RS-Pro 2 bar Gauge	8285760
RS-Pro 500 mbar Gauge	8285729
National Instruments	154424C-02L
Kd Scientific Legato 111	
Terumo 10 mL syringe	
Voltcraft power supply	PS-2403D

Table 3.4: Devices used

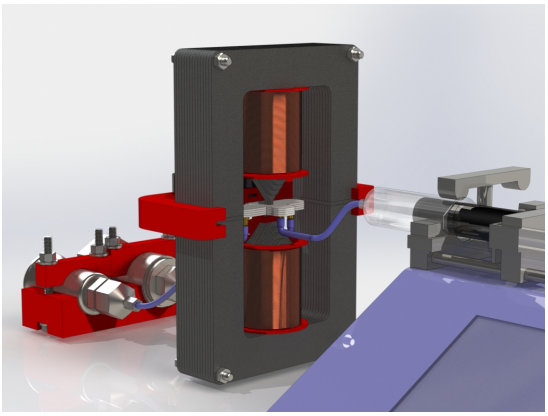

Figure 3.18: Test setup.

3.7 Measurement procedure

Figure 3.19 shows a typical measurement. The measurement is started in a steady state with zero flow. After 100 samples the measurement

is started. These sample points are used as zero measurement for the sensors. A flow rate is applied. Once the measured pressure has reached a steady state the flow rate is increased. This process is repeated until the syringe is empty. As the flow is stopped the pressures quickly return to their zero value.

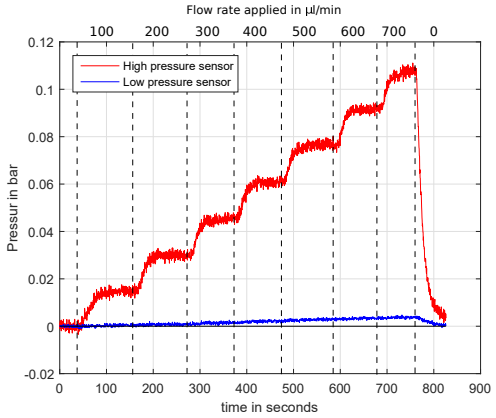

Figure 3.19: Typical measurement of pressure against time at different flow rates.

The measured pressures and flow rates are converted into shear stresses and shear rates through the geometrical model, equation [3.5,3.6], respectively.

3.8 Results

The resulting data is plotted for deionized water, Shell Tellus S2 VX15 and Ferrotec EFH1 in figures [3.20, 3.21, 3.22] respectively.

Deionized water The resulting viscosities at different shear rates are compared to the viscosity of deionized water at 21.8 °C, 0.96 mPa s, [33]. The maximum shear rate measured was 1.16×10^6 1/s. Higher shear rates were not measured as the pump engine stalled.

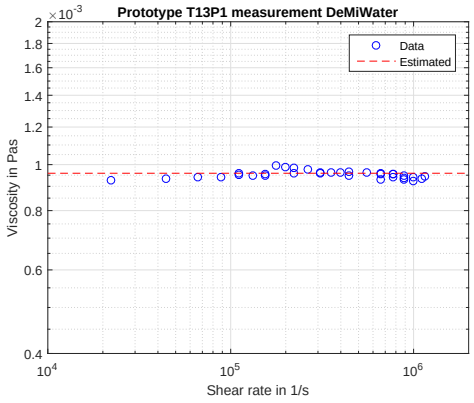

Figure 3.20: Viscosity of deionized water at high shear rates.

The chip was cleaned and filled with Shell Tellus S2 VX15. The resulting viscosities can be seen in figure 3.21. The expected viscosity is taken from the data sheet provided by Shell. The viscosity expected is 23 mPa s. The measurements from the Anton Paar rheometer have been added.

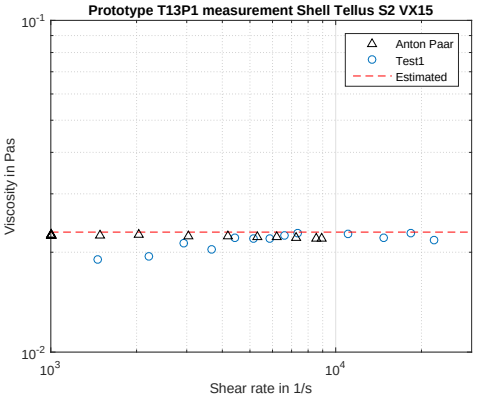

Figure 3.21: Viscosity of Shell Tellus S2 VX15 at high shear rates.

Lastly, Ferrotec EFH1 has been measured to show the magnetorheological effect. In figure 3.22 the flow rate was kept constant over the entire measurement. At the intervals shown the magnetic field was applied. The resulting pressure rise shows the magnetorheological effect. The resistance to flow has increased due to the magnetic field.

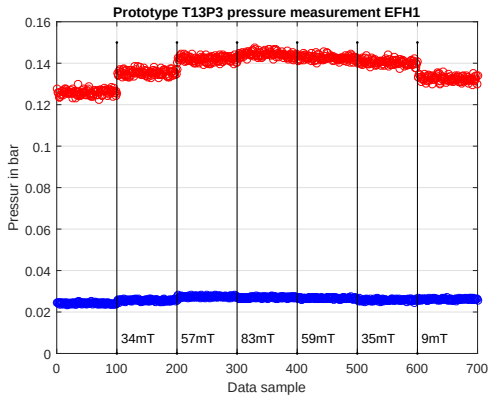

Figure 3.22: Viscosity of MR fluid with different magnetic fields.

3.9 Discussion

The goal of the research is to design a magnetorheometer capable of measuring at ultra high shear rates for MR fluids under the influence of a magnetic field. Firstly, a measuring principle was determined. A slit capillary rheometer was chosen as a concepts. It was chosen because of its high measuring range compared to other rheometer types, the simple application of the magnetic field and its low viscous heating effects. This concept was further developed into a detailed design for a prototype. Fabrication techniques were found and used to build the prototype. The resulting prototype succeeded in measuring deionized water, Shell Tellus S2 VX15 oil and Ferrotec EFH1 and showed the magnetorheological effect.

Measurement issues

Low pressure sensor During the measurement the measured pressure increases as the flow rate is increased. The resulting measurement is presented in figure 3.19. The low pressure sensor shows only small pressure steps. Expected pressures were calculate to estimate the performance of the system which showed larger pressure steps for the low pressure sensor. The cause was found upon inspection of the fabricated chip. During the chemical bonding of layers 1 and 2, figure 3.7, a misalignment is introduced. The misalignment is presented in figure 3.23. The exit length was dimensioned as 0.2 mm and is measured as 0.02 mm. This misalignment means that the exit length is reduced. The smaller exit length results in lower pressures measured at the sensors which is confirmed by the blue low pressure line in figure 3.19. This can be compensated for in the data processing and therefore has no effect on the measured viscosity. The misalignment could be prevented by introducing alignment features in the design.

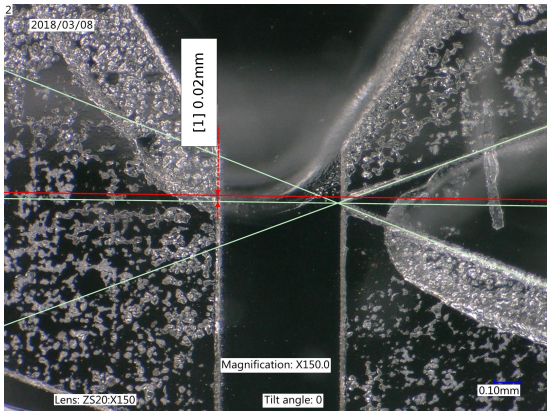

Figure 3.23: Misalignment influencing the measured low pressure.

Maximum shear rate The maximum shear rate measured is $1.16 \times 10^6\,\mathrm{s}^{-1}$. No higher shear rates were measured as the syringe pump motor stalled. This means the maximum pump pressure was applied to the chip. The expected pressure at the entrance for the maximum shear rate measured is 4.4 bar, whereas the maximum pressure produced by the pump is 6.7 bar, appendix E.3.1. This means this pressure is lost between the pump and the sensors. Further analysis revealed that this is caused by a restriction in the channel entrance. The restriction has two sources: the channel swelling in the flattening stage and the misalignment between layers 1 and 2, figure 3.7.

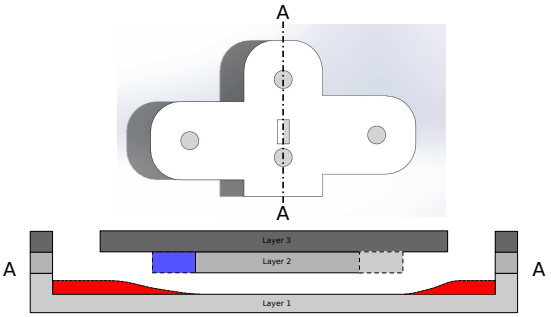

Figure 3.24: Entrance restriction, channel swelling in red, misalignment in blue

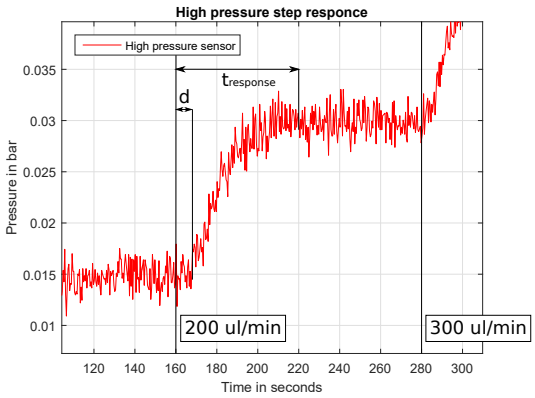

Figure 3.25: High pressure response to flow rate step increase.

As layer two is closer to the swelling of the channel (blue in figure 3.24), the entrance becomes much smaller than designed and causes an increased pressure drop. The swelling of the channel could be prevented by removing the flattening stage, section 3.6.1. This means improving the master such that the bonding surfaces are smooth.

Response time As a step in the applied flow rate is initiated, a delay(d) is noticed in the pressure response. After this delay the pressure rises steadily and stabilises to a pressure, figure 3.25. The delay is primarily caused by air bubbles in the syringe. The air in the syringe is compressed as the pressure increases, reducing the applied flow rate temporarily. After this initial delay the measured pressure increases, although not instantly as the incompressibility assumption would suggest. The slow response, (t_{response}), is caused by the type of pressure sensors used. The sensors have a membrane which deforms due to the applied pressure. The deformation is measured and converted into a pressure. Due to the incompressibility, the deformation of the membrane means an increase in the volume in the sensor channel. This volume has to be filled with fluid from the measuring channel to increase the measured pressure. The limited access to the measuring channel creates a flow restriction which causes the slow response of the measured pressure.

The delay can be prevented by draining the air bubbles from the system before measuring. The pressure response can be accelerated by having smaller measuring membranes in the sensors. This reduces the volume flow required for the pressure to increase. A further improvement would be to reduce the restriction to the measuring channel.

Blockages Some measurements failed due to blockages in the microchannel. It is critical to keep the system clean as the microchannel is a mere 30 µm in height. This issue was encountered with the first measurement using MR fluids. Due to the misalignment and swelling of the channels the effective gap was reduced significantly at the entrance. Due to the large particle size in the fluid, 1 µm to 2 µm, the entrance became blocked by the particles bridging across the channel,[34]. The blockage increased the pressure drastically at the entrance causing a leak of the chip. The entrance geometry can be improved to reduce the formation of particle bridges. The tapered entrance strengthens the bridges formed. Therefore a sharp entrance is preferred.

Syringe Due to the high flow rates required the maximum force is applied to the syringe. After the high shear measurements it was perceived that the syringe had deformed due to the applied

force. The fixation of the syringe pump is not able to hold the syringe in place, figure 3.26.

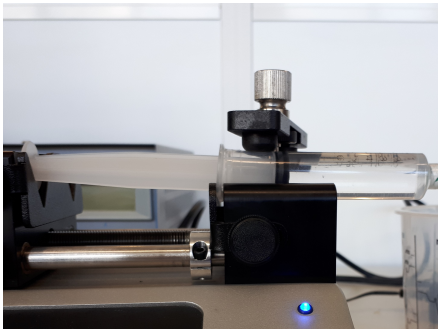

Figure 3.26: Deformation of the syringe due to high pressure in the system.

This results in the a slightly lower flow rate being applied to the chip which means lower pressures being measured. During the data processing this results in lower viscosity due to the flow rate used in calculation is higher than in reality. The deformation can be prevented by using stainless steel syringes or creating a custom fixation for the syringe pump.

Measurement results

The first step to derive these results is to process the measurement data. Three important topics in the processing of the data are discussed: the sensor zeroing, the used gap height and the exit length.

Sensor zeroing Before each measurement the pressures at zero flow rate were measured. The data is corrected during the data processing for the non-zero pressure at zero flow. The non-zero values are due to the gravitational force of the fluid in the connection tubes to the sensors and the offset of the sensors. However, due to the restriction in the sensor channels and surface tension of the measured fluid, the pressure did not always reach the true zero pressure value. The sensor channels were able to keep an over or under pressure. Once the flow was initiated the flow would correct itself.

Gap height The gap height is only known before the chemical bonding. As the channel swells about 2 µm, the exact gap height is slightly varying over the channel. The gap height is therefore slightly altered to fit the deionized water measurements. The alterations are less than 2 µm. Once the parameter is set it is not altered for any other measurement.

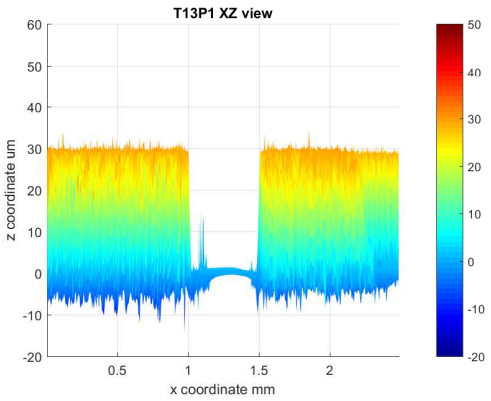

Figure 3.27: XZ view of T13P1 showing the channel swell.

Exit length Due to the misalignment of layer 1 and 2 in figure 3.7 the exit length is different than designed. The exit length is therefore slightly altered to fit the deionized water measurements. The value is checked by measuring using a Keyence optical microscope, figure 3.23. Once the parameter is set it is not altered for any other measurement.

3.9.1 Discussion measurements

The highest deviation for the water measurement is less than 8 % for deionized water and Shell Tellus VX15 oil. The maximum shear rate measured is 1.16×10^6 s^{-1}. The measurements with Ferrotec EFH1 show the device is able to measure the magnetorheological effect. This means that this prototype can be expanded into measuring MR fluids at high shear rates. To be able to perform these measurements some improvements will be necessary. Currently the system is not strong enough

to withstand the pressures involved with measuring MR fluids at high shear rates as the viscosity of MR fluids are higher.

3.10 Conclusions

From the physics based analysis of the measuring principles, it follows that capillary devices have an advantage in measuring MR fluids as they can reach higher shear rates while simplifying the application of a magnetic field. In figure 3.20 and 3.21 we see the measurement has a maximum deviation of 8 % compared to the true viscosity. The viscosity is measured to a range of 10^4 1/s to 1.16×10^6 1/s.
When measuring MR fluids we can clearly see the influence of the magnetic field on the viscosity.
Therefore, we have designed and built a prototype of an ultra high shear rheometer capable of measuring MR fluids and a range of 10^4 1/s to 10^6 1/s.

Chapter 4

Discussion

The goal of this research was to design a magnetorheometer for MR fluids under the influence of a magnetic field. The first step in this process was to determine a measuring principle. A tool was developed to estimate the measuring ranges of different measuring principles, chapter 2. The results indicated that a capillary design would have a larger range compared to the other types of rheometers. Together with the simplicity of the application of the magnetic field and the reduced viscous heating the slit capillary was chosen as a concept. This concept was further developed into a detailed design for a prototype, chapters 3 and appendix D. Fabrication techniques were found and used to build the prototype, appendix E. The resulting prototype succeeded in measuring deionized water, Shell Tellus S2 VX15 oil and Ferrotec EFH1 and to show the magnetorheological effect. Firstly, the tool for the theoretical measuring ranges is discussed. Secondly, the magnetorheometer is discussed focussing on the design, fabrication and the results.

4.1 Theoretical measuring range

The tool introduced uses limitations related to assumptions in the models for calculating the viscosity in the discussed rheometers. The limitations are taken from papers describing these effects on the rheometers. These descriptions have been adjusted to the other rheometers. The descriptions have been converted into the variables shear rate and viscosity to create the shear ranges.

4.1.1 Dimensionless numbers

The critical values for dimensionless parameters have been taken for the thin film situation. The $\widetilde{R}$ value has been taken from [19] which describes cone-plate systems. The assumption has been made that this value is equally valid for parallel plate rheometers. In literature different description were found for the Taylor number. The description of the Taylor number used is for larger gaps. The case study describes a small gap. Therefore, a description for thin gap Couette flow will describe the limit more accurately. The Reynolds numbers for the capillary rheometers has been given the maximum value of 1000. This number is taken from the consensus in literature that flow with Reynolds number below 1000 is laminar in a microchannel,[24]. The last dimensionless number is the Nahme number. The critical value of this parameter is not clearly defined. Depending on the conductivity of the

surrounding material and the heat transfer at the walls, the viscous heating could start sooner. However, the limit is equally limiting for each rheometer type and therefore does not have an influence on the comparison between the rheometers. It does have an influence on the range of the rheometers. Preferably the Nahme number should be kept below 1, although, Nahme numbers of $\mathcal{O}(1)$ are seen as adequate, [28].

4.1.2 Predicted ranges

The predicted ranges give an estimation of the limitations. These boundaries have not been tested as this was outside of the scope of the thesis. The measuring ranges provide insight in where lie the limitation of a measurement as to improve the system and avoid inaccurate measurements. The limitations calculated should therefore be seen as estimations of the boundary and as indication to the source of issues measuring near this boundary. Further research into the lower boundaries will give a full description of the measuring range.

4.1.3 Common gap height

The common gap height links the different rheometer types. This characteristic length has been chosen as it is a crucial parameter for the MR fluids. The common gap determines the space for the magnetic particles to form chains. Furthermore, the gap height is the main component in the definition of the shear rate and thus viscosity and is the main variable in all the dimensionless numbers.

4.1.4 Case study

The case study describes the design problem in section 2.6. Figure 2.14 gives as prediction of the measuring ranges of kerosene for the different rheometers with a common gap height of 50 µm. The graph shows that the capillary devices have a higher measuring range compared to the other rheometers. Therefore, the measuring principle for the magnetorheometer should be a capillary device.

4.1.5 Tool

This tool provides information on how to improve the measurement. Furthermore, the tool developed is useful for the untrained rheologist performing high shear measurements. When a rheologist uses a device with an unfamiliar fluid, he can use the tool to estimate the range, figure 2.8. With these limitations the rheologist can make sure he performs an accurate measurement.

4.2 Discussion magnetorheometer

In the processes of designing and manufacturing of the magnetorheometer many intermediate steps have been taken. The results are 4 functioning chips which have been tested. The results will be discussed in 3 parts. Firstly, the design of the chip and core is discussed. Secondly, the manufacturing process is discussed. Lastly, the resulting measurements are discussed.

4.2.1 Design

The main characteristics of the microchannel are the entrance, measuring and the exit length, appendix D. The entrance length has been designed after the equation from [29]. The maximum allowable Reynolds number is set to 1000. Resulting in a length of 2.9 mm. This length is fully under the magnetic core therefore the total length of the entrance length is 3.7 mm. The measuring length is set to 1 mm to create a measurable pressure drop for the entire measuring range. The exit length is set to 0.2 mm. The sensor channels are necessary to create space for connectors. The design for the sensor channels can be improved.

4.2.2 Manufacturing

The chip manufacturing process consists of 5 main steps: the master fabrication, hot embossing, bonding, flattening and the core manufacturing. The quality of the manufacturing process was improved throughout the thesis.

Master production The master fabrication is performed with a laser, appendix E.1.1. This process creates the negative of the microchannel. This creates a smooth surface which is imprinted in the PMMA. The laser introduced an issue. Due to the path planning calculated by the internal software some areas were etched less than others. This height step in the master created bonding issues for the PMMA layers. The solution used was to change the laser pattern in order to force the laser path to be more even. This reduced the step but did not eliminate it. The software of the laser should be inspected or externally controlled. Another solution would be to use a different fabrication technique.

Hot embossing The hot embossing step copies the pattern of the master, appendix E.1.2. In this step the geometry of the channel is defined. The tools used for this process are a simple bolt tightened press and an oven. Due to these simple tools there is some variation between the embossed PMMA substrates. To further standardize the fabrication of the chips, commercial equipment should be used. These will result in more consistent results. This will also enable the determination of the optimal process parameters.

Bonding The bonding was performed using thermal bonding and chemical bonding, appendix E.1.2. The thermal bonding created a full bond. The thermal bonding could not be applied to the bonding of the embossed PMMA to the other layers as it causes the channel to swell and close. The chemical bonding solved this issue as it caused no swelling of the channel. Due to the uneven pressure of the press used the chemical bond did not bond the entire surface. However, the bond did provide a seal of the microchannel. An improved press would provide a more complete bond.

Flattening The flattening stage is introduced to improve the bonding surface of the embossed PMMA, appendix E.1.2. Without this step the bond between the layers would fail resulting in leakages. The flattening stage results in a improved bonding surface at the cost of swelling of the embossed channel. The swelling is only 2 µm in the microchannel. The flattening stage can be omitted by improving the quality of the master.

Core manufacturing The core was designed to produce a homogeneous field, appendix D.2. The core should provide 1 T at 1 A. The core produced reached a field density of 0.8 T at 3 A, appendix E.2. The design overestimated the field created by the core, as the calculations assumed a simpler design. The introduction of the different layers created higher reluctance than calculated. Furthermore, the contact between the two core halves caused a small air gap which reduced the magnetic field density. Although the core did not reach the targeted values, it performed as satisfactory. Only a small field was necessary for the fluid tested. The core can be improved by using a monolithic design as well as optimizing the shape for magnetic field density.

4.2.3 Results

Four chips were produced. These have been tested with different fluids. With these chips measurements have been performed with deionized water, Shell Tellus S2 VX15 oil and Ferrotec EFH1. The first chip, (T9P5) was used to measure deionized water. The second chip,(T13P1), was used to measure deionized water and Shell Tellus VX15 oil. The last two chips,(T13P3 and T14P1), were used to measure deionized water and Ferrotec EFH1. The results from these measurements are presented in appendix F. The tests using T13P1 were used to assess the accuracy of the prototype. Tests usign T13P3 and T14P1 were used to determine the magnetorheological behaviour. During the measurements some issues were detected. The sources of these issues are discussed. Afterwards the measurement results are discussed.

Measurement issues

The following measurements issues were detected:

Low pressure sensor During a measurement the measured pressure increases as the flow rate is increased. The resulting measurement is presented in figure 3.19. The low pressure sensor shows only small pressure steps. Expected pressures were calculate to estimate the performance of the system. These showed larger expected pressure steps for the low pressure sensor. Upon inspection, the cause was found in the fabricated chip. During the chemical bonding of layers 1 and 2, figure 3.7, a misalignment is introduced. The misalignment is presented in figure 3.23. The exit length was dimensioned as 0.2 mm and is measured as 0.02 mm. This misalignment means that the exit length is reduced. The smaller exit length results in lower pressures measured at the sensors which is confirmed by the blue low pressure line in figure 3.19. This can be compensated for in the data processing and therefore has no effect on the measured viscosity. The misalignment could be prevented by introducing alignment features in the design.

Maximum shear rate The maximum shear rate measured is $1.16 \times 10^6\,\mathrm{s}^{-1}$. No higher shear rates were measured as the syringe pump motor stalled. This means the maximum pump pressure was applied to the chip. The expected pressure at the entrance for the maximum shear rate measured is 4.4 bar, whereas the maximum pressure produced by the pump is 6.7 bar, appendix E.3.1. This means this pressure is lost between the pump and the sensors. Further analysis revealed that this is caused by a restriction in the channel entrance. The restriction has two sources: the channel swelling in the flattening stage and the misalignment between layers 1 and 2, figure 3.7. As layer two is closer to the swelling of the channel (blue in figure 3.24), the entrance becomes much smaller than designed and

causes an increased pressure drop. The swelling of the channel could be prevented by removing the flattening stage, 3.6.1. This means improving the master such that the bonding surfaces are smooth.

Response time As a step in the applied flow rate is initiated, a delay(d) is noticed in the pressure response. After this delay the pressure rises steadily and stabilises to a pressure, figure 3.25. The delay is primarily caused by air bubbles in the syringe. The air in the syringe is compressed as the pressure increases, reducing the applied flow rate temporarily. After this initial delay the measured pressure increases, although not instantly as the incompressibility assumption would suggest. The slow response, (t_{response}), is caused by the type of pressure sensors used. The sensors have a membrane which deforms due to the applied pressure. The deformation is measured and converted into a pressure. Due to the incompressibility, the deformation of the membrane means an increase in the volume in the sensor channel. This volume has to be filled with fluid from the measuring channel to increase the measured pressure. The small access to the measuring channel creates a flow restriction which causes the slow response of the measured pressure. The delay can be prevented by draining the air bubbles from the system before measuring. The pressure response can be accelerated by having smaller measuring membranes in the sensors. This reduces the volume flow required for the pressure to increase. A further improvement would be to reduce the restriction to the measuring channel.

Blockages Some measurements failed due to blockages in the microchannel. It is critical to keep the system clean as the microchannel is a mere 30 µm in height. This issue was encountered with the first measurement using MR fluids. Due to the misalignment and swelling of the channels the effective gap was reduced significantly at the entrance. Due to the large particle size in the fluid, 1 µm to 2 µm, the entrance became blocked by the particles bridging across the channel,[34]. The blockage increased the pressure drastically at the entrance causing a leak of the chip. The entrance geometry can be improved to reduce the formation of particle bridges. The tapered entrance strengthens the bridges formed. Therefore a sharp entrance is preferred.

Syringe Due to the high flow rates required the maximum force is applied to the syringe. After the high shear measurements it was perceived that the syringe had deformed due to the applied force. The fixation of the syringe pump is not able to hold the syringe in place, figure 3.26. This results in a lower flow rate being applied to the chip which means lower pressures being measured. During the data processing this results in lower viscosity due to the flow rate used in calculation is higher than in reality. The deformation can be prevented by using stainless steel syringes or creating a custom fixation for the syringe.

Measurement results

The measurements were performed on the 4 chips. The result of each chip is presented in appendix F. There is some difference between the performance of each chip. The first step to derive these results is to process the measurement data. Three important topics in the processing of the data are discussed: the sensor zeroing, the used gap height and the exit length.

Sensor zeroing Before each measurement the pressures at zero flow rate were measured. The data is corrected during the data processing for the non-zero pressure at zero flow. The non-zero values are due to the gravitational force of the fluid in the connection tubes to the sensors and the offset of the sensors. However, due to the restriction in the sensor channels and surface tension of the measured

fluid, the pressure did not always reach the true zero pressure value. The sensor channels were able to keep an over or under pressure. Once the flow was initiated the flow would correct itself.

Gap height The gap height is only known before the chemical bonding. As the channel swells about 2 µm, the exact gap height is slightly varying over the channel width, figure 3.27. The gap height is therefore slightly altered to fit the deionized water measurements. The alterations are less than 2 µm. Once the parameter is set it is not altered for any other measurement with the chip.

Exit length Due to the misalignment of layer 1 and 2 in figure 3.7 the exit length is different than designed. The exit length is therefore slightly altered to fit the deionized water measurements. The value is checked by measuring using a Keyence optical microscope, figure 3.23. Once the parameter is set it is not altered for any other measurement.

Chip T9P5 Chip T9P5 was used for the first measurement with deionize water. This chip was made with the first master type [1]. The gap height of this chip is only 25.8 µm. This prototype was bonded only using thermal bonding. Therefore the channel geometry is not well defined due to the channel swelling. This caused the pressures measured to rise slowly. The viscosity measurements in figure F.3a show quite a spread in viscosity measured, the largest deviation is 26%. The lower shear rate measurements are more reliable as the high shear rates stabilized slowly and showed unstable behaviour due to deformation of the syringe and dirt in the channel.

Chip T13P1 Chip T13P1 is the first chip chemically bonded with success. This chip was made using the adjusted master. This chip was used for the measurement of deionized water and Shell Tellus S2 VX 15 oil. The measurement for water resulted in a maximum deviation of 8% to the estimated deionized water viscosity. The same accuracy was found for the Shell Tellus S2 VX 15 oil. The misalignment together with the channel swelling present in the chip limited the maximum shear rate to 1.16 s^{-1}. An attempt to measure Ferrotec EFH1 failed as blockages occurred due to the reduced entrance.

Chip T13P3 Chip T13P3 was used for the measurement of deionized water and Ferrotec EFH1. During the manufacturing of the chip, the silicon master fractured. Resulting in a damaged channel. The chip was chemically bonded multiple times due to blockages during manufacturing. The chip channel quality is therefore low. In the initial deionized water measurement it showed that the access to the low pressure sensor channel was not fully bonded resulting in much higher pressures than expected. Measurements with chip T13P3 can, therefore, not be used for quantitative measurement, however, it can be used for qualitative measurements of the magnetorheological effect. Figure F.5a shows the resulting measurement points indicating a step response in the pressure due to the application of the magnetic field, figure F.6a.

Chip T14P1 Chip T14P1 was used for the measurement of deionized water and Ferrotec EFH1. The water measurements show a maximum deviation of 11%. The low pressure sensor channel shows a slow response to the pressure input due to the misalignment. Figure F.5b shows the resulting measurement points indicating a step response in the pressure due to the application of the magnetic field. The Anton Paar rheometer measured the viscosity of Ferrotec EFH1 as 8.5 mPa s. The measurement of chip T14P1 showed the viscosity without magnetic field to be 11 mPa s, figure F.6b. The low

[1] See appendix E.1.1 for more information.

pressure sensor channel showed no pressure increase during the Ferrotec EFH1 measurement. This is due to the surface tension limiting the influx. By priming the channel with the to be measured fluid a more accurate measurement is expected. The increase in viscosity due to the applied field is around 10% which is expected for Ferrotec EFH1.

4.2.4 Measuring MR fluids using capillary rheometer

The measurements with Ferrotec EFH1 show that the prototype is able to measure magnetic fluids. Ferrotec EFH1 has small particles ($\pm 20\,nm$) compared to common MR fluids($\pm 1\,\mu m$). The larger particles might become an issue. The entrance must be at least 10 times larger than the particle size to prevent blockages. Another issue is sedimentation of the MR fluid in the syringe. If the fluid remains too long in the syringe sedimentation can occur. The sedimentation changes the particle concentration in the microchannel. By using ultrasonic vibrations the particles can be agitated to prevent the sedimentation in the syringe.
For the prototype to measure MR fluids at high shear rates some improvements are needed. Currently the system is not strong enough to withstand the pressures involved with measuring MR fluids at high shear rates as the viscosity of MR fluids are higher.

Chapter 5

Conclusions and recommendations

5.1 Theoretical measuring range

5.1.1 Conclusions

The tool designed gives an estimation of the measuring range of different types of rheometers. It compares the measuring ranges of the rheometers through a characteristic length. It provides insight into what is limiting a measurement. This information can be used to improve the measurement. The tool developed is useful for the untrained rheologist performing high shear measurements. When a rheologist uses a device with an unfamiliar fluid, he can use the tool to estimate the range and make sure he performs an accurate measurement.

5.1.2 Recommendations

The use of the tool can still be improved. Firstly, by testing the accuracy of the predicted ranges. This will make the tool more reliable. Secondly, the tool can be extended with the lower boundaries of the devices.

5.2 Magnetorheometer

5.2.1 Conclusions

From the theoretical analysis of the measuring principles, it follows that capillary devices have an advantage in measuring MR fluids as they can reach higher shear rates while simplifying the application of a magnetic field.

In figure 3.20 and 3.21 we see the measurement has a maximum deviation of 8 % compared to the true viscosity. The viscosity is measured to a range of $10^4\ s^{-1}$ to $1.16 \times 10^6\ s^{-1}$.
When measuring Ferrotec EFH1, we can clearly see the influence of the magnetic field on the viscosity. Therefore, we have designed and built a prototype of an ultra high shear rheometer capable of measuring MR fluids and a range of $10^4\ s^{-1}$ to $10^6\ s^{-1}$.

5.2.2 Recommendations

The recommendations are split in three parts. Firstly, the recommendations on the current prototype are discussed. Secondly, the recommendations to extend the current system are discussed. Thirdly, the recommendations for future setups are discussed.

Improvements to current system A first recommendation is to improve the alignment of the PMMA layers. Due to the misalignment the entrance and exit lengths are influenced. This changes the measured pressures. This does not alter the quality of the measurement as long as these lengths are adjusted in the data processing. The misalignment of a produced chip is shown in figure 3.23. The exit length designed is 0.2 mm. The measured exit length is 0.02 mm. The measurements presented in figures [F.3,F.4,F.6] have been adjusted for the misalignment. The alignment can be improved by designing alignment features on the chip.

A second recommendation would be to improve the master fabrication. The use of the laser created unwanted uneven surfaces which disrupted the bonding of the PMMA layers. This was partially solved by using a flattening process however could be avoided completely. The main problem was the laser path. The direction of the laser had an effect on the etching rate creating the unevenness. The path planning is done by the laser software and could not be edited. Another master fabrication could be used, for example, using a chemically etched master. This would improve the surface roughness of the bonding surfaces and therefore increase the bonding strength. Another solution would be to use a soft master. A glass plate with SU-8 spincoated on it. By using lithography the design can be etched and used as a master for the embossing process, however, these are more time consuming to produce,[31] and damage by use.

A third recommendation would be to use a better press. The press used functioned, however, the parameters could not be tuned finely. This could be achieved by creating a press with a better defined force application, force measurement and better defined parallel plates. A commercial hot embossing press would improve the quality of the chip.

A fourth recommendation would be to improve the draining system. Currently, the MR fluid flows into a container and is waisted. A recuperating system can be designed. The MR fluid is attracted to the core and spills over it. By creating a barrier for the fluid, the fluid can be contained are prevent contamination of the setup.

Extension of the current system The current system can be improved to extend the measurement capabilities. Firstly, using a stronger pump to reach the high pressures designed for. The chip will need to be supported in order to withstand the pressures. By doing this the range of the rheometer is expanded to higher viscosity fluids.

Secondly, by adding temperature control the ability to measure at a certain temperature. This information is important as the MR fluids are used in environments reaching high temperatures.

Thirdly, the magnetic core design can be optimized. The current shape is simple and leaves space for accessibility however it limits the maximum magnetic field density and could be increased.

Improvements for future setup Using integrated pressure sensors. This would result in more local pressure sensing and would eliminate the effects of an interrupted wall for pressure taps. Furthermore, the pressure changes would be measured instantly. Integrated pressure sensors are much harder to manufacture.

Thirdly, the system can be extended to electrorheological fluids. These fluids alter their rheological properties under the influence of an electric field. By simply separating the core pieces and insulating them, an electric field can be applied. Care should be taken in the safety of the device as electrorheometers use voltages in the kilovolt range.

Appendix A

Introduction to rheology

The measurement of viscosity is done using a viscometer. A viscometer is defined as 'an instrument for the measurement of viscosity', however the viscosity of non-Newtonian fluids depends on much more. The viscometer is therefore inadequate to characterise the behaviour of these fluid and has to be replaced by a rheometer, defined as 'an instrument for measuring rheological properties'. Where rheology is the study of flow. The first step to understand what we are measuring is to define some fluid characteristics. Viscosity is defined as the resistance to shearing flow.

The definition of viscosity is the 2D case where a fluid is sheared between two parallel plates, figure A.1. The bottom plate is stationary while the upper plate is moved with a constant velocity. Assuming zero slip at the wall the velocity profile of the fluid can be seen in figure A.1. The shear stress is constant through the fluid. The viscosity is the ratio between the shear stress exerted on the plate and the shear rate of the fluid and can be expressed as in equation A.1. A fluid with a high viscosity requires more force to move than a fluid with low viscosity, which will move with ease. An example of a low viscosity fluid is water. A high viscosity fluid would be tar.

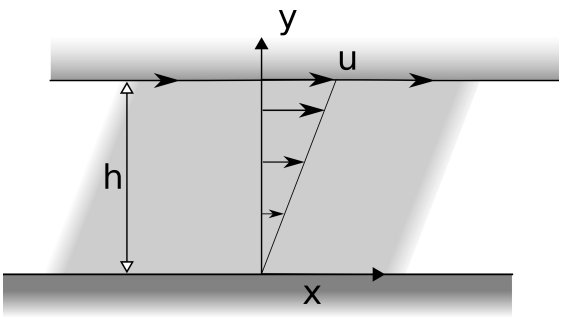

$$\eta = \frac{\tau}{\dot{\gamma}} \tag{A.1}$$

$$\dot{\gamma} = \frac{\partial u}{\partial h} \tag{A.2}$$

Figure A.1: Definition of viscosity

For the simplest fluids this viscosity is a constant however this is not valid for all fluids. The viscosity can be dependent on the shear applied. This means fluids can have a higher or lower viscosity depending on which shear rate they experience. Viscosity is dependent on many parameters such as temperature, pressure, time and many more. Therefore, to measure the shear dependence of a fluid

the other parameters have to be controlled or of negligible influence. The goal of rheology is to describe fluid behaviour in models such that they can be used to predict behaviour in applications. Large part of the rheology research has been conducted for the food process industry. The behaviour of fluids has been described through various models. These models differ in complexity and applicability. The most basic fluid is the Newtonian fluid. A list of models can be found below these models have been, table A.1. Another dependency of viscosity is time. There are fluids models describing the behaviour change over time. The general categories are Thixotopic and Rheopecitic. Meaning increasing viscosity and decreasing viscosity over time respectively.

Model name	Model		Comment
Newtonian model	$\tau = \eta\dot{\gamma}$	(A.3)	Constant viscosity, fluids such as water, air.
Power law model	$\tau = \eta\dot{\gamma}^n$	(A.4)	Viscosity is shear dependent, for n<1 shear thinning, for n>1 shear thickening, fluids such as ketchup, cornstarch mixed with water.
Bingham model	$\tau = \tau_y + \eta\dot{\gamma}$	(A.5)	Constant viscosity with a yield stress, fluids such as toothpaste or mayonnaise
Herschel Bulkley model	$\tau = \tau_y + \eta\dot{\gamma}^n$	(A.6)	Viscosity is shear dependent with a yield stress, for n>1 shear thickening.
Ellis model	$\tau = \frac{\dot{\gamma}}{\frac{1}{\eta_0} + K_E(\tau)^{(\frac{1}{n_E})-1}}$	(A.7)	Low shear rate data with a η_0
Sisko model	$\tau = \eta_\infty\dot{\gamma} + K_S\dot{\gamma}^{n_S}$	(A.8)	High shear rate data with a η_∞.
Cross model	$\tau = \eta_\infty + \frac{\eta_0 - \eta_\infty}{1 + (\alpha_c\dot{\gamma})^m}$	(A.9)	To describe a wide range of data.
Carreau model	$\tau = \eta_\infty + \frac{\eta_0 - \eta_\infty}{[1 + (\lambda_c\dot{\gamma})^2]^N}$	(A.10)	To describe a wide range of data.
Casson model	$\tau^{0.5} = K_{0c} + K_c(\dot{\gamma})^{0.5}$	(A.11)	Specifically for chocolate and printing ink
Mizrahi berk model	$\tau^{0.5} - \tau_{0M} = K_M(\dot{\gamma})^n_M$	(A.12)	modification of the Carreau model
Ofoli et al. model	$\tau^{n_1} = \tau_0^{n_1} + \eta_\infty(\dot{\gamma})^{n_2}$	(A.13)	Four parameter model for inelastic food fluids.
Vocadlo model	$\tau = [(\tau_{oV}^{\frac{1}{n_V}}) + K_V\dot{\gamma}]^{n_V}$	(A.14)	

Table A.1: Table of fluid models [35]

Appendix B

Rheometers

Rheology is the study of flow of matter. To be able to measure these properties devices are needed. These devices can take many forms and shapes. In this chapter the different type of rheometers are presented. The rheometers have been categorised in 4 sections by their working principles.

- Pressure driven flows.
- Shear driven flows.
- Shape flows.
- Velocimetry

Each section describes the working principle of the rheometer and the different types available. The working formulas of each rheometer are stated. Finally a comparison between the rheometers is made.

B.1 Pressure driven flows

This section describes the rheometers based on the oldest principle of rheometry. These rheometers where first used to measure viscosity. They are based on a pressure differential forcing the fluid through a tube. The fluid will viscously dissipate energy along the wall of the tube. The first kinds of rheometers where not able to use sensors as they were not available yet and were, therefore, based on visual reference. Later on, more complicated pressure driven rheometers were developed.

The flow in these rheometers is Poiseuille flow as can be seen in figure B.1. The flow profile can be calculated from the Navier-Stokes equation G.1 for incompressible flow.

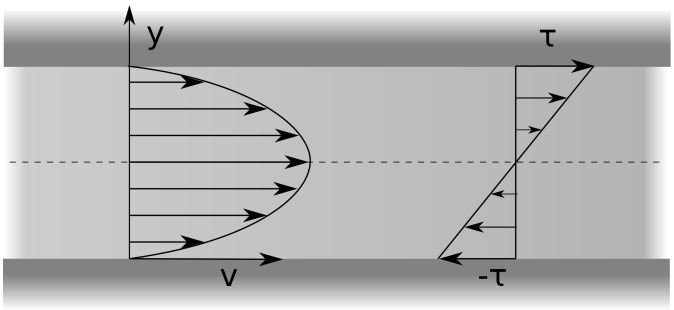

Figure B.1: Pouseille flow for Newtonian fluid, the left drawing shows the velocity profile. The right shows the shear stress profile.

Key assumptions in this measuring technique are:

- Laminar isothermal flow.
- Stationary flow conditions.
- Pressure independence of the liquid.
- Incompressibility of the liquid.
- Wall adherence of the liquid.
- Neglect the flow influences at entry and exit of the capillary of sufficient length.

A capillary viscometer works according to the Hagen-Poiseuille law. The viscometer consists, in its simplest form, of a capillary tube. The fluid is put in a capillary and slowly flows down due to a differential pressure. The flow is slowed down by the viscous forces acting inside the fluid and on the capillary wall. The liquid flows in a parabolic velocity profile through the capillary. The Hagen-Poiseuille law can be derived from the momentum equation of the Navier-Stokes equation. The resulting volumetric flow rate can be found in equation B.1.

$$Q = \frac{\pi R^4 \Delta P}{8 L \eta} \tag{B.1}$$

The viscosity can thus be measured in two different ways:

- Measure the pressure differential at a constant volume flow through the capillary
- Measure the volume flow at a fixed differential pressure.

The first type of measurement can be used for continues measuring of fluid properties. The accuracy is dependent on the accuracy of the differential pressure and the stability of the volume flow. This type of rheometer is usually a slit rheometer or a capillary rheometer.

The second type of measurement is used purely for the measurement of viscosity. This type of measurement has been the first to be applied. These capillaries are time based and thus timed capillary viscometers.

B.1.1 Timed capillary viscometer

The measurement is done by measuring the time it takes for a certain volume to flow through the capillary. This is measured either with sensors or visually. The time and the volume complete the Hagen-Poiseuille law and can be used to calculate the viscosity.

a. Ostwald

b. Ubbelohde

c. Cannon-Fenske

d. Houillon.

The capillaries can be seen in figure B.2.

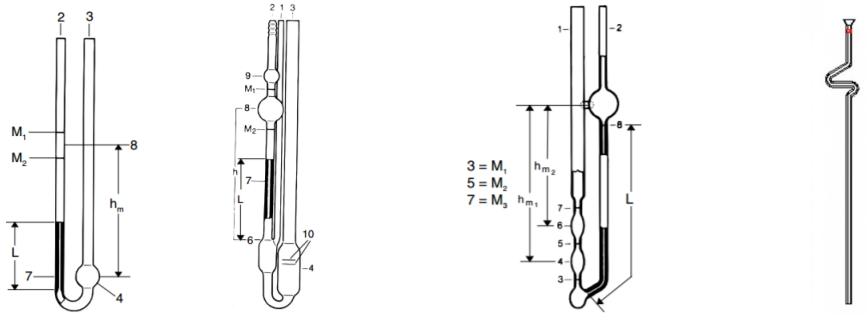

(a) Ostwald (b) Ubbelohde (c) Cannon (d) Houillon

Figure B.2: Capillarie viscometers, 1 Ostwald, 2 Ubbelohde, 3 Cannon-Fenske, 4 Houillon.[36]

.

Ostwald

The Ostwald in filled through tube 3, figure B.2a. The heigh of filling determines the mean pressure. For the measurement the fluid is sucked up through the tube 2 up to a the first mark, M1. The time is measured until, when the pressure is released, the level descends to the second mark, M2. See figure B.2a.

Ubbelohde

The Ubbelohde is an improved version of the Ostwald. It works in the same way. The viscometer is filled through tube 3 until it is within the maximum and minimum indicated at mark 10. On can either suck the fluid up into tube 2 or use overpressure in tube 3 to fill tube 2. The fluid has to reach at least up until midway the pre-run sphere 9. Once this is done tube one is cleared. This causes column of fluid to break off at bulb 6. This means the hydrostatic column is no longer dependent on the amount of filled fluid which increases the accuracy of the pressure differential. Furthermore the fluid flowing down into bulb 6 will flow along the wall as a film which reduce the interference of the surface tension. The time is measured for the fluid to flow down from mark M1 to mark M2. See figure B.2b.

Cannon-Fenske

To determine whether the specific volume has flowed through the capillary, a sensor or a visual reference is used in the Ostwald and Ubbelohde, however this is only possible when the fluid used is reasonably clear. When this is not the case the Cannon-Fenske viscometer can be used. The viscometer held upside down and is filled through tube 2 until the mark 8. A plug is inserted in tube 1 to stop any flow. The viscometer is turned right side up and the plug in tube 1 removed to let the fluid flow into the bottom bulb. The bulb is half filled and stopped with a plug in tube 2. The measurement is performed by removing the plug and time the rising of the fluid from mark M1 to mark M2 and from mark M2 to mark M3. Due to the fact the fluid is flowing upward the surpassing of the marks can clearly be seen as the fluid has not passed there yet. See figure B.2c.

Houillon

The Houillon viscometer is mainly used in automatic viscometers. The glass is specially shaped for low sample volumes and for fast analysis. The viscometers are not as accurate as the ones named before, however, can easily be cleaned and reused. The amount of samples that can be analysed per time unit is higher than in the others. As in the other capillaries the time is measured for the sample to flow through the capillary. The Houillon tube is a reverse flow viscometer which means opaque samples can be measured. See figure B.2d.

Rheometer	**Benefits**	**Drawbacks**
Ostwald	Simple	Only clear fluids Newtonian liquids Forcing pressure inaccurate Slow Fixed shear rate
Ubbelohde	Independent on fluid column No influence of fluid tension	Only clear fluids Newtonian liquids Slow Fixed shear rate
Canno-Fenske	Opaque fluids independent of fluid column	Slow Newtonian liquids Fixed shear rate
Houillon	Opaque fluids Fast Small samples	Newtonian liquids Fixed shear rate

B.1.2 Capillary rheometer

The capillary rheometers apply a constant volume flow through a tube or slit and measure the pressure drop over the length of the capillary. The pressure drops due to viscous friction. These rheometers are mostly used to analyse polymers. In these rheometers the range of the measurement is determined by the geometry of the capillary. Furthermore the range of the sensors is a limitation to these devices. There are multiple geometries possible. Simple ones such as circular capillaries but also more complex shapes such as square, rectangular, trapezoid. These stress the fluid in a different way. Depending on the fluid a certain geometry is preferred. The final application of the fluid sometimes determines

the geometry as this simulates the future application. This is done with polymer solutions which are used in the plastic industry. The polymer melt is forced through a small shape. A consideration in the geometry is the development of the flow. For viscosity measurement a easily determined flow profile is required.

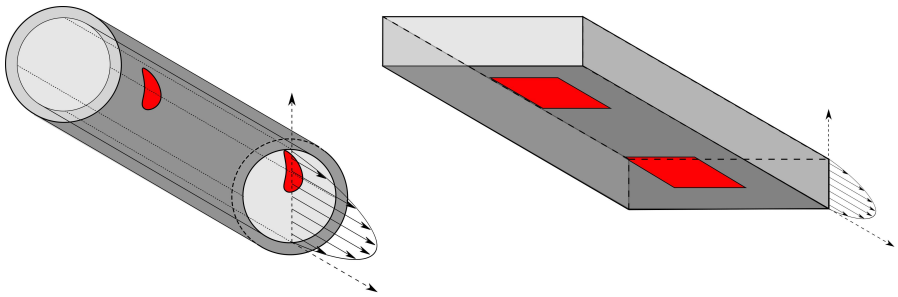

Figure B.3: Round capillary and a slit capillary, pressure sensors drawn in red.

Rheometer	Benefits	Drawbacks
Round capillary	Simple High shear rates Analytical solution	Inlet and outlet pressure losses Pressure sensors disturb flow
Slit capillary	Simple High shear rates	Inlet and outlet pressure losses Edge effect Cleaning slit corners

B.2 Shear driven flows

The second category contains the shear driven flows. These are flows where mechanically the fluid is sheared. This type of rheometer have a moving part which drives the fluid. The fluid resists this movement due to viscous forces. From this resistance the viscosity can be derived. These rheometers work with a shear profile that can be seen in figure B.4. This flow profile is also known as Couette flow.

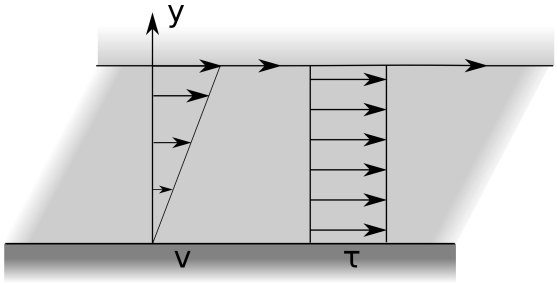

Figure B.4: Couette flow for Newtonian fluid, the left drawing shows the velocity profile. The right shows the shear stress profile.

key assumptions in this measuring technique are:

- Laminar isothermal flow.
- Stationary flow conditions.
- Incompressibility of the liquid.
- Wall adherence of the liquid.

The shear driven flow rheometers work close to the definition of viscosity. They apply either a constant shear force and measure the velocity of the moving wall or vice versa. Depending on the geometry of the rheometer the basic formula has to be adjusted. In the flow, the shear force is constant over the gap. This means the shear rate is constant over the gap. These rheometers can not be used for continuous on-line measurements.

B.2.1 Rotational viscometers

Rotational viscometers are viscometers creating a shear flow to measure the viscosity. The flow can be created in multiple manners, however, the main principle is to create a shear strain and measure the torque required for this. From these the viscosity can be determined. The rotational viscometers are the following:

a. Concentric cylinder
    - Couette flow
    - Searle flow
b. Cone plate
c. Parallel plate
d. Sliding plate
e. EMS

Concentric cylinders

The concentric cylinders consist of a cup and a spindle. The cup is filled with the to be tested fluid and the spindle immersed. In the Couette type the cup is rotated to minimize centrifugal forces. The Searle type rotates the spindle.

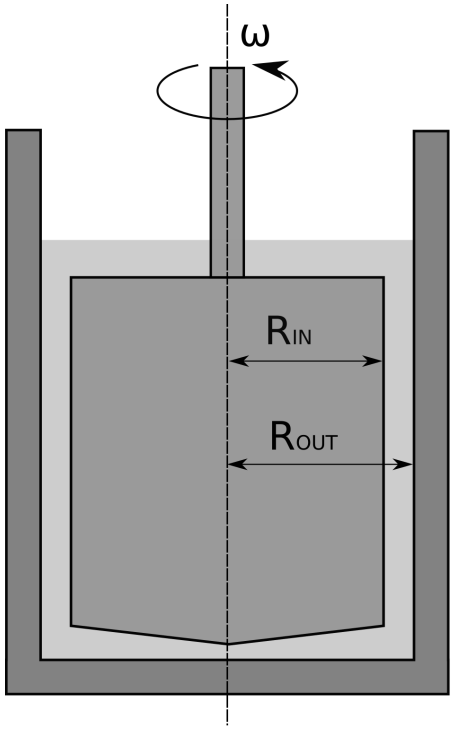

Figure B.5: concentric cylinder viscometer

Due to the similarity between these principles the formulas provided will be considering the Searle type rheometer. The torque is measured at the stationary cylinder. With these values the viscosity of the fluid can be calculated. Due to the shape of the cylinders the shear profile around the inner cylinder is constant, however not constant in the radial direction. In case of a small gap the working formulas can be found in equationB.2.

$$\dot{\gamma} = \frac{\omega R_{\text{in}}}{(R_{\text{out}} - R_{\text{in}})} \tag{B.2}$$

$$\tau = \frac{M}{2\pi R_{\text{out}}^2 L} \tag{B.3}$$

$$\eta = \frac{\tau}{\dot{\gamma}} = \frac{M(R_{\text{out}} - R_{\text{in}})}{2\pi R_{\text{out}}^2 R_{\text{in}} \omega L} \tag{B.4}$$

The concentric cylinders is influenced by the end effects. Different solutions have been found to solve this issue. The ends have been made into cones as to have a constant shear and to include these in the viscosity calculation. Another solution is to use a different medium that relative to the measured fluid does not transfer torque to the spindle. This is done by creating an air bubble under the spindle to reduce the torque disturbance. Lastly to increase the range to the low viscosity fluids hollow spindles are used to have more shear area, figure B.6.

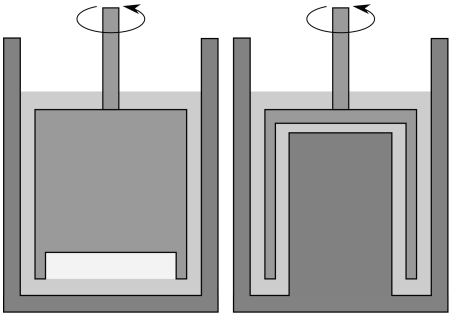

Figure B.6: Reduction of end effects by using adjusted geometry.

An issue with the concentric cylinder approach is the rotational motion. This motion creates a centrifugal force on the fluid which develops into an instability. The flow develops Taylor vortices which influence the measurement.

Another issue with the concentric cylinder approach is the friction in the actuation system. This friction influences the measurement by increasing the torque required to drive the system. A magnetic drive train was developed for the Stabinger™ rheometer, figure B.7,[37]. It uses a immersed core with a temperature controlled outer cylinder. The core is lighter than the fluid and thus moves freely in the sample and is centred by centrifugal forces. The outside cylinder is spun and due to the viscous forces the core starts to rotate as well. The core has on the inside a permanent magnet. This magnet causes an eddy current in the soft iron ring around the outer cylinder. This functions as an eddy current brake. An equilibrium is found between the moment forced by the viscous forces and the eddy current brake. The viscosity can be calculated. The core speed and braking is measured from the current through the soft iron ring and a hall sensor.

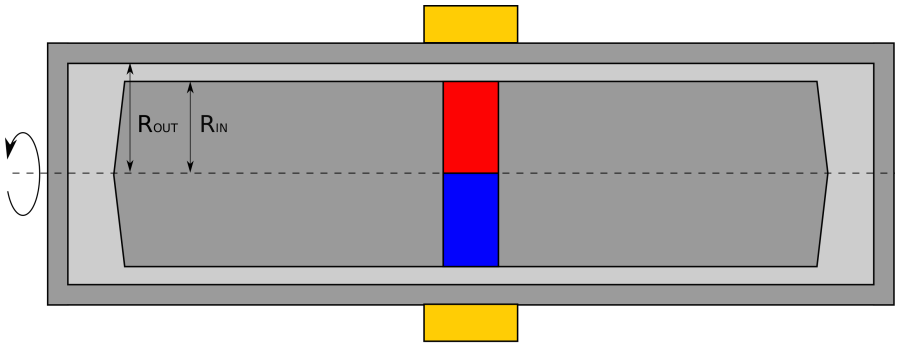

Figure B.7: Stabinger™ rheometer sketch, orange = soft iron ring.[37]

$$\dot{\gamma} = \frac{R_{\text{out}}\omega_{\text{out}} - R_{\text{in}}\omega_{\text{in}}}{R_{\text{out}} - R_{\text{in}}} \tag{B.5}$$

$$\tau = \frac{M_{\text{eddy}}R_{\text{in}}}{A} \tag{B.6}$$

$$\eta = \frac{\tau}{\dot{\gamma}} = \frac{M_{\text{eddy}}R_{\text{in}}R_{\text{out}} - R_{\text{in}}^2}{\omega_{\text{out}} - R_{\text{in}}\omega_{\text{in}}} \tag{B.7}$$

Another adaptation to the concentric cylinder is the so called tapered bearing simulation (TBS), figure B.8. The TBS uses a tapered inner cylinder with a matching outer cylinder. With this adaptation the error in the alignment and the gap error is reduced. Using the TBS gaps are reduced to several microns. With this device ultra high shear rheometry is performed.

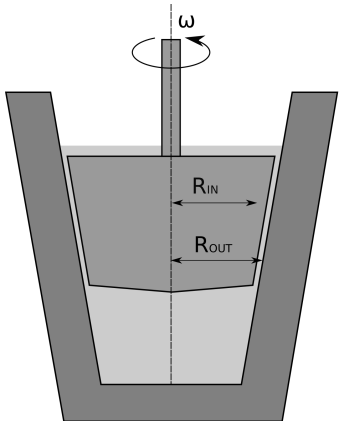

Figure B.8: Tapered bearing simulator

Cone plate viscometer

The cone plate viscometer uses a spinning cone and a stationary plate which are aligned axially. The sample is placed under the cone. The cone is lowered onto it. Different measuring setups are available. Either the torque or the rotational speed can be controlled and the counterpart measured. Furthermore the measuring place can be changed. The torque can be measured at the stationary plate or in the cone. The speed is measured at the rotating shaft.

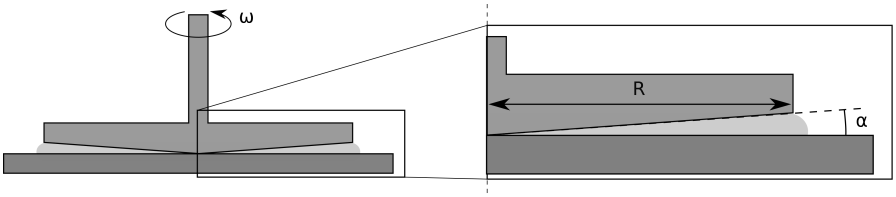

Figure B.9: Sketch of a cone plate viscometer with a zoomed in sketch including parameters, α for cone angle and R for cone radius.

Due to the shape of the cone the shear rate is constant over the entire surface of the cone. This is due to the angle of the cone. The increase in rotational speed by being further from the axis is compensated by having a larger gap, figure B.9 and equation B.8

$$\dot{\gamma} = \frac{\omega r}{r \tan \alpha} = \frac{\omega}{\tan \alpha} \tag{B.8}$$

$$\tau = \frac{3M}{2\pi R^3} \tag{B.9}$$

$$\eta = \frac{3T \tan \alpha}{2\pi R^3 \omega} \tag{B.10}$$

In practice the cones are truncated. The truncation prevents direct contact between cone and plate. The contact would create friction which is not due to the viscous forces. Therefore the virtual tip make contact with the plate. One disadvantage of the cone plate rheometer is the open edge. This open edge creates end effects. You should also avoid using a cone if the sample you are testing contains particulate material. If the mean particle diameter is not some five to ten times smaller than the gap, the particles can 'jam' at the cone apex resulting in noisy data. Gap setting is crucial for a cone plate rheometer as well as the alignment. Small error in these parameters have large impact on the measurement. Cone plate rheometers are therefore not recommended for temperature sweeps. There are cone plate rheometers that compensate for the thermal expansion.

Parallel plate viscometer

The parallel plate rheometer is similar to the cone plate viscometer. Instead of having a cone and a plate this viscometer uses two plates. One plate is rotated while the other remains stationary. Different measuring setups are available. Either the torque or the rotational speed can be controlled and the counterpart measured. Furthermore, the measuring place can be changed. The torque can be measured at the stationary plate or in the rotating plate. The speed is measured at the rotating shaft.

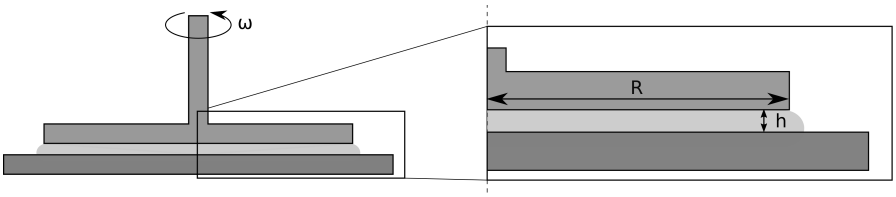

Figure B.10: Sketch of a parallel plate viscometer

In the parallel plate setup the gap height is constant over the plate. The shear rate is, therefore, increasing towards the edge of the plate. The values calculated by the rheometer are apparent shear rates and shear stresses at the edge of the plate.

$$\dot{\gamma} = \frac{\Omega r}{H} \tag{B.11}$$

$$\tau = \eta \dot{\gamma} \tag{B.12}$$

$$\eta = \frac{2Mh}{\pi R^4 \Omega} \tag{B.13}$$

The advantages of using a parallel plate rheometer are that it is easy to clean. Large range of shear rates and viscosities can be measured as the gap height and the plate radius can be varied. One disadvantage of the parallel plate rheometer is the open edge. This open edge creates end effects. Gap setting is crucial for a parallel plate rheometer as well as the alignment. Small error in these parameters have large impact on the measurement. Parallel plate rheometers are therefore not recommended for temperature sweeps. There are parallel plate rheometers that compensate for the thermal expansion.

Sliding plate viscometer

The sliding plate viscometer is the closest to the direct definition of viscosity. The sample is loaded between two parallel plates which are fixated at the required gap height. One plate is moved by an actuator or by an attached weight. The shear rate is measured through the displacement of the plate and the shear stress through sensors or the applied force. This is then used to derive the viscosity.

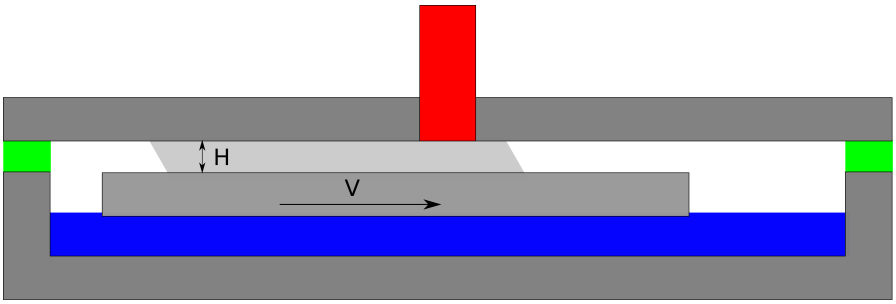

Figure B.11: Sketch of a sliding plate viscometer

$$\dot{\gamma} = \frac{V}{h} \tag{B.14}$$

$$\tau = \frac{F}{A} \tag{B.15}$$

The benefit of a sliding plate viscometer is that has a uniform flow field and non irregularities associated with rotational rheometers. This is especially useful for assessing polymer melt flows. [38] [39]. The sliding plate rheometer does have some downsides. Acceleration is part of the measurement. Furthermore, it is uncertain how well area is wetted.

Electro Magnetically Spinning Sphere viscometer

The Electromagnetically Spinning sphere viscometer uses a small aluminium sphere which is immersed in the sample. A rotating magnetic field is applied which induces eddy currents in the sphere. A Lorentz force is induced which causes the sphere to spin. The sample is in a tube with a concave ending. The tube is temperature controlled. The speed of the sphere is measured with a camera under the tube. The torque on the sphere is related to the angular velocity of the magnetic field and the angular velocity of the sphere.[40]

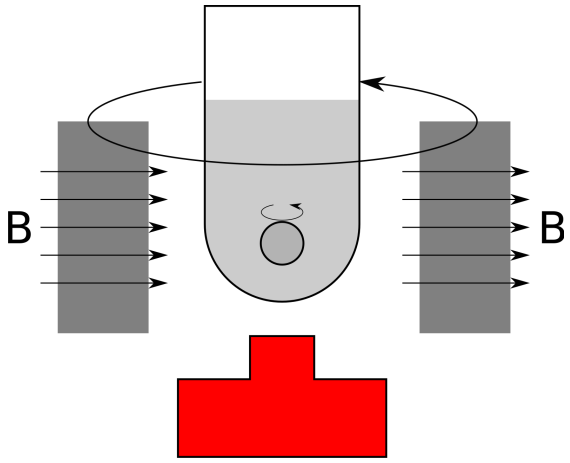

Figure B.12: Sketch of electromagnetically spinning sphere viscometer.

$$\eta = \frac{K(I - I_0)}{v} \tag{B.16}$$

The benefit of electromagnetically spinning sphere is the non contact actuation. This allows for high pressure measurement without information being lost due to friction on actuation due to seals. It needs to be calibrated against a known fluid due to the inhomogeneous flow.

Rheometer	**Benefits**	**Drawbacks**
Concentric cylinders	Accurate	Difficult to clean Taylor vortices
Cone plate	Constant shear rate Easy to clean	Edge effects Not suitable for fluids with large particles Secondary flows
Parallel plate	Simple Easy to clean Variable gap height	Varying shear rate over the plate Secondary flows
Sliding plate viscometer	Simple Close to definition of viscosity	Open edges
EMS	No friction in actuation system No contamination	Needs to be calibrated

B.2.2 Falling ball viscometer

A falling ball viscometer works by letting a sphere fall through a tube. The viscous forces together with the gravitational force and the buoyancy forces become balanced. The ball reaches a terminal velocity. The buoyancy force and gravitational force can be calculated. The viscous force can be determined by measuring the terminal velocity which can be converted into viscosity.

$$\eta = \frac{2}{9}\frac{(\rho_s - \rho_f)}{\nu} g R^2 \tag{B.17}$$

Adaptation of the falling ball viscometer are falling cylinder and rolling ball viscometers. The falling cylinder uses a cylinder instead of a ball. The falling ball viscometer does experience wall effects and end effects.

B.2.3 Rising bubble

A different viscometer is the rising bubble viscometer. This viscometer uses the buoyancy to let bubbles rise through the fluid. The measurement can be performed in two ways, a comparison method or the time method. The time method measures the time required for the bubble to rise a specific distance. This time and distance is converted together with the dimensions of the tube into the viscosity. The comparison method determines the viscosity by comparing the rising of the bubbles to precisely calibrated standards. The one that matches best resembles the viscosity of the fluid.
The tubes are filled with fluid to the 100 mm mark. A cork is inserted up to the 108 mm mark. The tube is placed on a suitable rack and flipped vertically. The time is measured for the bubble to rise from the 27 mm mark to the 100 mm mark.

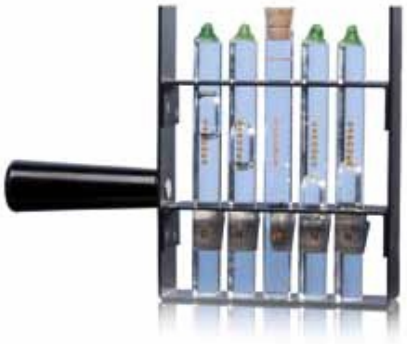

Figure B.13: Rising bubble viscometer

The equation for this viscometer is similar to the equation for falling ball viscometry. The extra influence is the viscosity of the bubble itself. This effect is added as a factor, equation B.18.

$$\eta = \left(\frac{1}{\epsilon}\right)\frac{2}{9}\frac{(\rho_s - \rho_f)}{\nu} g r^2 \tag{B.18}$$

$$\epsilon = \frac{2\eta + 3\eta'}{3(\eta + \eta')} \tag{B.19}$$

With η' being the viscosity of the bubble. The shape of the bubble remains mostly spherical as the tube diameter is 5 times larger than the bubble diameter and has little effect on the accuracy of the measurement. The wall effects are much larger therefore the ratio of container length to bubble diameter must be in the range 10-100.

B.3 Vibrational viscometers

Next to the constant movement viscometers there is a oscillating viscometer. The viscometer works by measuring the damping caused by the viscous forces of the moving body. This damping is representative for the viscosity. This type of rheometry can be done on the rotational viscometers and specialised vibrational viscometers. In the case of using a rotational viscometer the damping is measured by oscillating the spindle around its axis. This causes the liquid to resist and this can be measured in the change in damping and frequency. The specialised oscillatory viscometers have two tuning forks vibrating.

Rotational oscillatory rheometers

Rotational oscillatory viscometers can be applied to the rotational rheometers discussed in section B.2.1, however, apply a different principle. Instead of applying a constant shear stress or shear rate, the oscillatory rheometers apply shear waves. These waves cause a shear stress response which can be measured. The difference between the strain applied and the measured shear stress gives information about the fluid behaviour. Especially about the viscoelastic behaviour.

$$y(\omega) = y_0 \sin(\omega t) \tag{B.20}$$

$$\tau(\omega) = \tau_0 \sin(\omega t + \delta) \tag{B.21}$$

Tuning fork viscometers

The tuning fork viscometer vibrates two beams by use of electromagnetic forcing. The beams are in counter phase to have no resulting force on the device. The displacement of the forks is measured. The forcing of the forks is controlled. The energy consumed by the system will be caused by the viscous forces as well as the losses in the system. The amplitude is kept constant and the change in the required forcing needed to keep the system in its natural frequency. This forcing is then converted into the viscosity. Figure B.14.

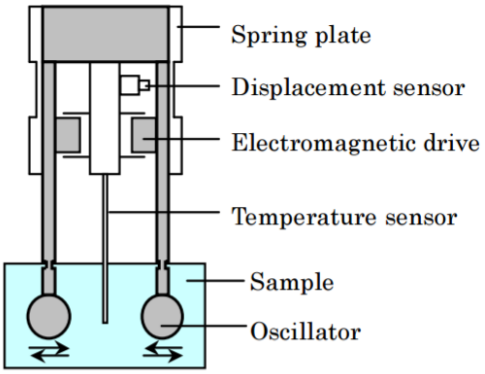

Figure B.14: Tuning fork type viscometer. [41], Physical Quantity Measured by a Vibration Viscometer

B.4 Velocimetry

Velocimetry is an adaptation to conventional measurement techniques. The main component is to measure the flow profile. From the flow profile the viscosity and shear behaviour can be determined. The velocimetry uses the velocity profile to determine the shear behaviour. By measuring the velocity profile the shear rate through the fluid can be determined. Together with the forcing the viscosity can be calculated. There are two types of velocimetric viscometers: nuclear magnetic resonance imaging rheometer and the ultrasound pulse Doppler mapping.

Nuclear Magnetic Resonance

The nuclear magnetic resonance(NMR) uses the same principle as is used in an MRI machine on the flow in a capillary. There are different NMR techniques. Time of flight techniques and the phase-based technique. The time of flight technique uses two pulse tag detect sequence. A plane of spins is tagged. At different distances a detection pulse is sent. In this way the displacement of the tagged particles can be followed and thus the velocity profile determined. The position of the tagged spins is determined by setting gradient magnetic field over the plane. The magnetic field determines the frequency of the rf signal sent out by the particles given by the Larmor relation, equation B.22. A sketch of an NMR seen in figure B.15. In black are the constant field coils. In blue are the gradient coils. In red are the sensors and in green are the rf signal generators. Together with the shear stress distribution the shear dependent viscosity can be determined of the [42] The phase-based technique is similar to the time of flight technique. It uses a pulse field gradient signal such that the phase of the detected signal is dependent on the displacement of the fluid.

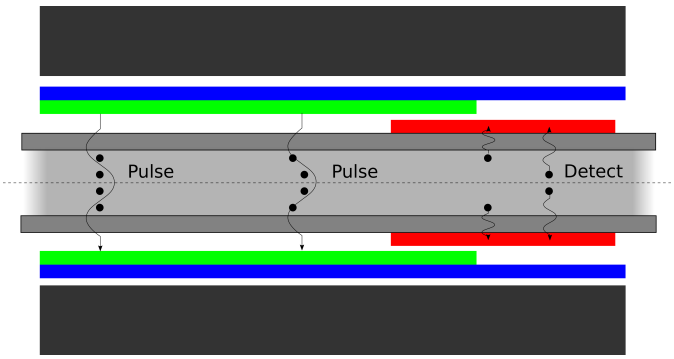

Figure B.15: Sketch of NMR rheometer

$$\omega = 2\pi f = -\gamma_{\text{gyr}}|B| \tag{B.22}$$

The benefit of this technique is that it is non-invasive. Furthermore only one measurement is needed to determine the viscosity for a range of shear rates. The down side is the large magnetic fields required.

Ultrasound Pulse Doppler mapping

Ultrasound pulse Doppler mapping(UPD) uses the Doppler effect to determine the viscosity. An ultrasonic pulse is sent into the fluid. The moving particles will reflect the incoming pulse with a frequency shift. After sending the pulse the measurement device measures the reflected wave. The different frequencies measured can be converted into the velocity of the particle, equation B.23. The device measures at different time intervals to determine the distance to the reflecting particles. The position of the particle together with the velocity of the particle gives the velocity profile. The velocity profile together with the shear stress is converted into viscosity.

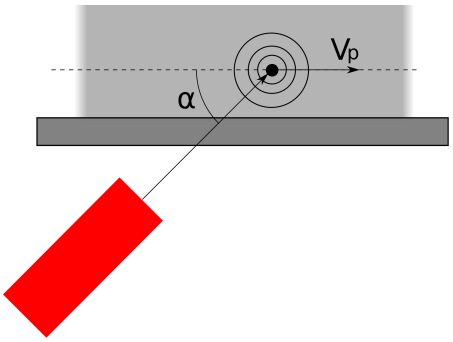

Figure B.16: Sketch of Ultrasound pulse Doppler mapping rheometer

$$v_{\text{meas}} = v_{\text{p}} \cos\alpha = \frac{f_{\text{meas}} c_{\text{s}}}{2f} \tag{B.23}$$

The benefit of UPD is that it is non-intrusive. It can determine the behaviour of the fluid near the boundary, such as wall slip and yield stress. The downside of UPD is that the speed of sound in the material needs to be known and that measurements are time consuming as multiple measurements are needed to determine the velocity profile.

Appendix C

Magnetorheological fluids

C.1 History

Before the 1930's all magnetic material known to man was in the form of a solid material. This was either a permanent magnet or soft magnetic material. The first use of magnetic particles in a suspension was used to detect imperfections in the surface of paramagnetic material. The first scaled use of it was with NASA to control the liquid rocket fuel as in space the absence of gravity would make the fluid float in the holding tanks and no longer power the rocket. It was a challenging task to design a pump deliver fuel to the combustion chamber. Steven Papell envisioned to give the rocket fuel magnetic properties to control it under zero gravity conditions and pull it towards the magnets near the combustion chamber. Papell is credited in literature with the preparation of the first magnetic fluid based on kerosene. This was the first case of the use of a ferrofluid. The first magnetorheological fluid(MR fluid) has been developed by Jacob Rabinow. The MR fluid contrasts with ferrofluid by having larger particles and having a yield stress under the influence of magnetic fields. In 1948 J. Rabinow patented the first application of a MR fluid, the MR clutch,[3]. Soon after he patented the MR force transmitter, [4]. The interest in MR fluids died out due to the simultaneous development of the electrorheological fluids, (ER fluid), which were thought to have more potential in industry, however, their breakthrough still remains illusive. The interest in MR fluids returned in the early 1990's. The main benefits of MR fluids compared to ER fluids are the higher yield stress that can be obtained with MR fluids. MR fluids generally have a larger temperature working range and the excitation for ER fluids is in the kiloVolt range while for the MR fluids the excitation is much lower, [5]. From then on the fluid quickly found new applications. Applications such as MR damper [6]. The MR damper was first developed by the Lord Corporation for truck seats and is still being used. The technology was further developed by General Motors in partnership with Delphi corporation to produce dampers for the automotive industry and made its début in production cars from Cadillac as MagneRide in 2002. MR dampers can now be found in high end cars such as Audi and Ferrari,[7]. Further applications such as the MR brake[8] as well as in bearing applications,[[9], [10]] and more,[[2], [5]].

C.2 Properties

In the most basic terms a magnetic fluids fluid consist of three components: magnetic particles, a carrier liquid and a stabiliser. The magnetic particles are usually magnetite (Fe_3O_4) or carbonyl iron powders. These particles are spherical in shape and can be treated as a single domain particle. These particles are suspended in a carrier. The carriers are generally oil, however, different carriers can be used. To make sure the particles remain suspended the particles are coated with a surfactant. This surfactant keeps the particles from sticking together and creating a solid sediment when the fluid is stationary. There are two types of magnetic fluids: Ferrofluids and MR fluids. The difference between these fluids is not binary. MR fluids show a significant change in rheological properties when under the influence of a magnetic field. The particles create chains and structures thus resisting flow. The MR fluids show a yield stress. When ferrofluids are subjected to a magnetic field the particles do create chains however remain colloidal and thus in a fluid state. The ferrofluid experience a force and are pulled towards the highest density of magnetic field, however, show no to less change in rheological properties compared to MR fluids. This effect is caused by the size of the particles. The MR fluid particles are larger and thus have a stronger magnetisation. Furthermore, the MR fluids are generally not colloidal stable.

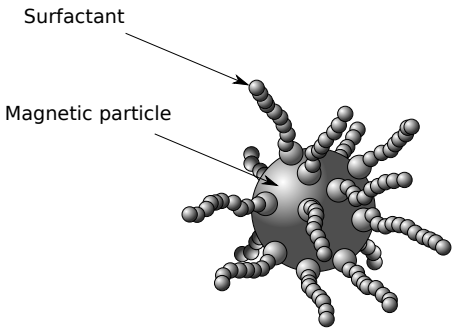

Figure C.1: Schematic sketch of a magnetic particle of a magnetic fluid.

Magnetic fluids have two mechanisms with which they resist flow. The first mechanism can be seen in figure C.2. When a particle is in a laminar fluid flow it will rotate around its axis as to move over the slower layer next to it, figure C.2(a). As the field is applied the particles are magnetised and have their own magnetisation direction, figure C.2(b). Due to flow of the fluid the particles are rotated. As the particle is rotating in the magnetic field, the magnetic moment is rotated as well. This creates a misalignment between the magnetic field and the magnetic moment. Due to the angle between the magnetic moment and the field a magnetic torque is introduced to realign the particle with the field. This magnetic torque resists the rotation due to the flow thus resisting the flow itself and increasing the viscosity, figure C.2(c).

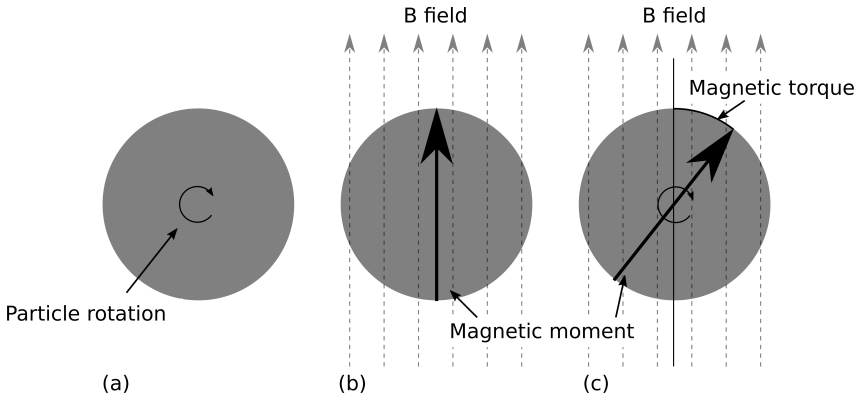

Figure C.2: Magnetorheological effect, (a) single particle in a fluid flow, Particle rotates due to the flow. (b) Particle in a stationary fluid under the influence of a magnetic field. (c) Particle in a fluid flow under the influence of a magnetic field.

The second mechanism resisting the flow is caused by the forming of chains by the particles. Due to the magnetic moment in the particles the dipole moment forces them together forming chains. Similar to the first mechanism the chains are harder to rotate and thus increase the viscosity.

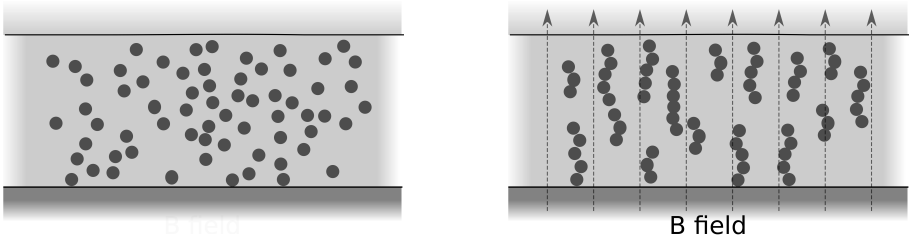

(a) Particles without influence of magnetic field (b) Particles with influence of magnetic field

Figure C.3: Magnetorheological effect

C.3 State of the art magnetorheometers

For the research into the flow properties of magnetic fluids magnetorheometers are needed. Currently only a few magnetorheometers are on the market. These are insets for parallel plate and cone plate devices. Figure C.4 presents the magnetic insets on the marker. These devices are limited in range by their measuring principle, chapter 2. These inserts use a coil under the stationary plate to create a magnetic field which is guided by a magnetic yoke. The rotating plate is of non-magnetic material to create a homogeneous field.

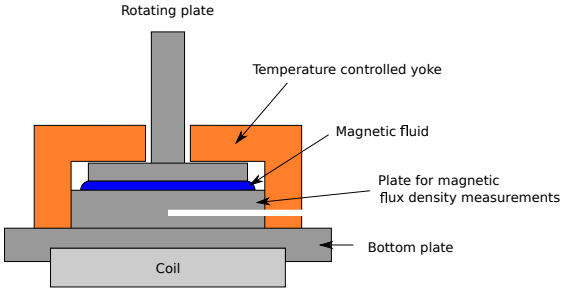

(a) Sketch of the magnetorheological insert components. [11]

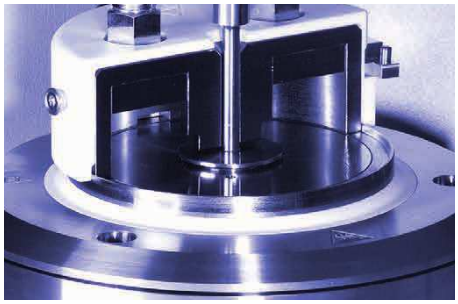

(b) Anton Paar rheological insert. [11]

(c) TA Magnetorheological insert. [12]

Figure C.4: Magnetic inserts for Anton Paar rheometer and TA rheometer.

Appendix D

Detailed design

D.1 Measurement system design

As was seen in chapter 2.6 the measuring principle to be designed is a pressure driven flow through a microchannel. Firstly, the working equations are derived and the critical dimensions determined. Secondly, the design is specified and the measuring range determined. The design is reiterated over the resulting pressures required and flow speeds. The result is a fully dimensioned microchannel with pressure sensors.

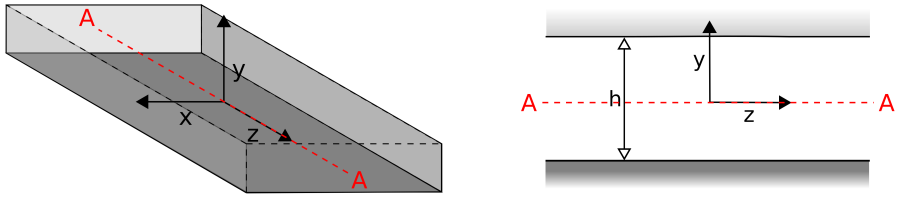

Figure D.1: Sketch of slit capillary.

Measuring viscosity using a slit capillary

The slit rheometer measures a pressure drop over a measuring length. The pressure together with the flow rate is converted into viscosity. Firstly, the pressure is related to the shear stress. The resistance to the flow which causes the pressure drop is connected to the fixed world through the walls of the channel. The shear stress applied to the surface of the wall summed up over a length is thus equal to the pressure drop, equation D.1. Figure D.1 presents the geometrical definitions for the slit rheometer.

$$\tau_{\text{wall}} = \frac{wh}{2(w+h)} \frac{\Delta P}{L} \tag{D.1}$$

Now the pressure stress relation is known, the flow in the channel can be analysed to determine the shear rate relation to the volume flow. To be able to do this the flow in the capillary has to be determined. The flow in a channel is described by the Navier-Stokes equation for incompressible fluids,

equation G.1. By assuming only flow in the length direction and assuming steady state the Navier-Stoke simplifies to equation D.2. Due to the rectangular shape the Navier-Stokes equation cannot be analytically solved. There are approximations of the exact solution using Fourier series, [43]. However, when using aspect ratios larger than 10 the approximation of infinite parallel plates is sufficiently accurate to neglect the side wall effects, [[44], [45]]. This simplifies the equation and allows it to be solved analytically.

$$-\begin{bmatrix} \frac{\partial p}{\partial x} \\ \frac{\partial p}{\partial y} \\ \frac{\partial p}{\partial z} \end{bmatrix} = \eta \begin{bmatrix} \frac{\partial^2 u_x}{\partial x^2} + \frac{\partial^2 u_x}{\partial y^2} + \frac{\partial^2 u_x}{\partial z^2} \\ \frac{\partial^2 u_y}{\partial x^2} + \frac{\partial^2 u_y}{\partial y^2} + \frac{\partial^2 u_y}{\partial z^2} \\ \frac{\partial^2 u_z}{\partial x^2} + \frac{\partial^2 u_z}{\partial y^2} + \frac{\partial^2 u_z}{\partial z^2} \end{bmatrix} \tag{D.2}$$

$$\frac{\partial u_x}{\partial x} + \frac{\partial u_y}{\partial y} + \frac{\partial u_z}{\partial z} = 0 \tag{D.3}$$

In steady state laminar flow, the fluid will only flow in z direction. This means the fluid speed is zero in the other directions. From the continuum equation, equation D.3, it follows the gradients in all directions are zero. Implementing the parallel plate approximation results in equation D.5.

$$-\left[\frac{\partial p}{\partial z}\right] = \eta \left[\frac{\partial^2 u_z}{\partial x^2} + \frac{\partial^2 u_z}{\partial y^2} + \frac{\partial^2 u_z}{\partial z^2}\right] \begin{cases} u_x = 0 \\ u_y = 0 \\ \frac{\partial p}{\partial x} = 0 \\ \frac{\partial p}{\partial y} = 0 \\ \frac{\partial u_z}{\partial z} = 0 \end{cases} \tag{D.4}$$

$$\left(\frac{\partial p}{\partial z}\right) = \eta \left(\frac{\partial^2 u_z}{\partial y^2}\right) \tag{D.5}$$

From this equation the flow profile can be derived for Newtonian fluids. Firstly, equation D.5 is integrated twice with respect to y.

$$\frac{1}{\eta}\left(\frac{\partial p}{\partial z}\right) y + C_1 = \left(\frac{\partial u_z}{\partial y}\right) \tag{D.6}$$

$$\frac{1}{2\eta}\left(\frac{\partial p}{\partial z}\right) y^2 + C_1 y + C_2 = u_z \tag{D.7}$$

Solve C_1, C_2 using boundary conditions.

$$y = \begin{cases} 0, & u_z = \text{finite} \\ \frac{h}{2}, & u_z = 0 \\ -\frac{h}{2}, & u_z = 0 \end{cases} \tag{D.8}$$

$$\frac{1}{8\eta}\left(\frac{\partial p}{\partial z}\right)h^2 + \frac{C_1 h}{2} + C_2 = 0 \tag{D.9}$$

$$\frac{1}{8\eta}\left(\frac{\partial p}{\partial z}\right)h^2 - \frac{C_1 h}{2} + C_2 = 0 \tag{D.10}$$

$$C_1 h = 0 \tag{D.11}$$

$$C_1 = 0 \tag{D.12}$$

$$C_2 = -\frac{1}{8\eta}\left(\frac{\partial p}{\partial z}\right)h^2 \tag{D.13}$$

This gives the velocity profile for steady state laminar flow in a rectangular channel as equation D.14.

$$u_z = \frac{1}{2\eta}\left(\frac{\partial p}{\partial z}\right)\left(\frac{h}{4}^2 - y^2\right) \tag{D.14}$$

The volume flow is calculated as the integral of the velocity profile times the width of the channel, equation D.15.

$$\left.\begin{aligned} Q = w\int_{-\frac{h}{2}}^{\frac{h}{2}} u_z \,\mathrm{d}y = w\frac{h^3}{24\eta}\frac{\partial p}{\partial z} \\ \frac{\partial p}{\partial z} = \frac{4\tau_{\text{wall}}}{h} \end{aligned}\right\} Q = \frac{wh^2\dot{\gamma}}{6} \tag{D.15}$$

Equation D.15 gives the relation for the Newtonian case. However, most fluids are non-Newtonian. To accommodate for this an analytical correction has been developed by Rabinowitsch,[27]. The correction starts with the integral of the flow velocity over the gap however does not assume a flow profile and leaves this as a variable.

$$Q = w\int_{\frac{-h}{2}}^{\frac{h}{2}} u_z(y)\, y \,\mathrm{d}y \tag{D.16}$$

Integration by parts

$$Q = w\left[\left[u_z(y)\right]_{\frac{-h}{2}}^{\frac{h}{2}} - \int_{\frac{-h}{2}}^{\frac{h}{2}} y\frac{\partial u_z}{\partial y}\,\mathrm{d}y\right] \tag{D.17}$$

$$Q = w\left[-\int_{\frac{-h}{2}}^{\frac{h}{2}} y\dot{\gamma}\,\mathrm{d}y\right] \tag{D.18}$$

Change of integration variables

$$Q = -\frac{wh^2}{4\tau_w^2}\int_{-\tau_w}^{\tau_w} \tau\dot{\gamma}\,\mathrm{d}\tau = -\frac{wh^2}{2\tau_w^2}\int_0^{\tau_w} \tau\dot{\gamma}\,\mathrm{d}\tau \tag{D.19}$$

Using Leibniz integration rule the integral can be solved. This is done by differentiating with respect to τ_w.

$$\frac{4\tau_w Q}{wh^2} + \frac{2\tau_w^2}{wh^2}\frac{\partial Q}{\partial \tau_w} = \int_0^{\tau_w} \frac{\partial}{\partial \tau_w} \tau\dot{\gamma}\,\mathrm{d}\tau + \tau_w\dot{\gamma}(\tau_w) \tag{D.20}$$

The integral is zero and the resulting can be reorganized into the Weissenberg-Rabinowitsch correction.

$$\left.\begin{aligned} \frac{4\tau_w Q}{wh^2} + \frac{2\tau_w^2}{wh^2}\frac{\partial Q}{\partial \tau_w} &= \tau_w\dot{\gamma}(\tau_w) \\ \dot{\gamma}_{\mathrm{app}} &= \frac{6Q}{wh^2} \end{aligned}\right\} \frac{\dot{\gamma}_{\mathrm{app}}}{3}\left[2 + \frac{d\ln(Q)}{d\ln(\tau_w)}\right] = \dot{\gamma}(\tau_w) \tag{D.21}$$

When performing a measurement the pressure drop at different volumetric flow rates is measured. The pressures are converted into shear stresses and the flow rates into shear rates for the Newtonian case. The natural logarithm of these curve is taken and fitted using a higher order polynomial. The differential of the measurements is taken and equation D.21 is applied correcting the shear rates at which the stresses occur. For the curve found the y axis crossing can be extrapolated, resulting in the yield stress.

D.1.1 Microchannel design

In the section above, the pressure and flow rate have be related to shear stress and shear rate respectively. This relation does depend on the following assumptions.

1 Laminar flow

2 Isothermal flow

3 Fully developed flow

These assumptions determine some of the dimensions of the microchannel. The other dimensions are chosen to fulfil the requirements.

D.1.2 Laminar flow

During the measurement laminar flow is crucial. In laminar flow, the flow conditions are known and thus predictable. When the flow becomes turbulent, extra stress is induced in the flow which disturbs the measurement. The Reynolds number is commonly used as an indication of laminar flow. The Reynolds number of the system at a given shear rate can be calculated. The Reynolds number can be rewritten into a critical parameter.

$$\mathrm{Re} = \frac{\rho v_{\mathrm{mean}} d_h}{\eta} \tag{D.22}$$

$$v_{\mathrm{mean}} = \frac{h\dot{\gamma}_{\mathrm{app}}}{6} \tag{D.23}$$

$$\mathrm{Re} = \frac{\rho}{\eta}\frac{2wh}{w+h}\frac{h\dot{\gamma}_{\mathrm{app}}}{6} = \frac{\rho w h^2 \dot{\gamma}_{\mathrm{app}}}{3\eta(w+h)} \leq 1000 \tag{D.24}$$

The limit of fully developed laminar flow in macro systems is at a Reynolds number of 2300. In literature the true microscale transition to turbulence Reynolds numbers is still discussed. Some studies have found it to occur at Reynolds numbers of 200-500,[23].The general assumption, concluded from different researches,[24], shows laminar flow below a Reynolds number of 1000 for microchannels.

D.1.3 Isothermal flow

The temperature has significant effect on the viscosity of a fluid. The fluid temperature should, therefore, remain constant during its passage through the measurement system. Due to the particles flowing past each other, friction is created which is turned into the heat. This principle is known as viscous heating. Most of the generated heat is conducted through the fluid and taken out of the system. When the flow reaches high shear rates, a lot of heat is generated. This heat ultimately reduces the viscosity of the fluid. To quantify the effect of the heating on the viscosity the dimensionless Nahme-Griffith is used, equation D.25. The Nahme number is the ratio of the viscous heating generated and the conduction of the heat out of the system and is closely related to the Brinkman number, [27]. As long as the Nahme number is below 1 the heat generated is less than the heat conducted out of the system.

$$\mathrm{Na} = \frac{\beta h^2 \dot{\gamma}^2}{k} \leq 1 \tag{D.25}$$

D.1.4 Fully developed flow

When a larger stream enters a smaller channel the flow profile is drastically changed. Due to this agitation the flow needs to stabilize into its new flow profile, figure D.2.

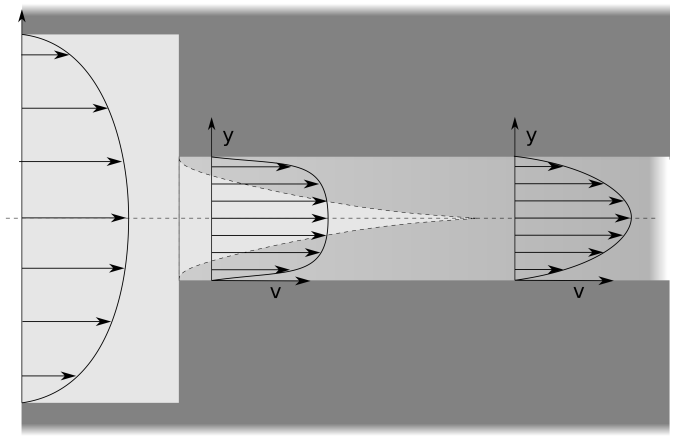

Figure D.2: Entrance length needed to stabilize flow profile.

Stabilisation of the laminar flow have been researched and result in equations for the required entrance length to reach fully developed flow. The length is related to the Reynolds number and has been described for macro applications as:

$$\frac{L_e}{d_h} \approx 0.06\mathrm{Re} \tag{D.26}$$

For micro applications the equation for the length is more complex as particle interactions become more dominant. There are many descriptions of the correct length for different Reynolds numbers. They are described in [46] for aspect ratios of 1. The non linearity starts at very low Reynolds numbers and is empirically fitted. For low aspect ratios the parallel plate approximation by Chen is used, [29]. With very low aspect ratios the entrance length is even more reduced, [47]. Therefore the Chen parallel plate approximation is used for maximum Reynolds numbers.

$$\frac{L_e}{d_h} \approx \frac{0.63}{1+0.035\mathrm{Re}_{\max}} + 0.044\mathrm{Re}_{\max} \tag{D.27}$$

$$d_h = \frac{4 \times \text{cross section area}}{\text{wetted perimeter}} = \frac{2wh}{w+h} \tag{D.28}$$

D.1.5 Measuring length

After the entrance length, the flow is fully developed and laminar. From this point we move into the measuring length and finally the exit length. These lengths define the measured pressure drop.

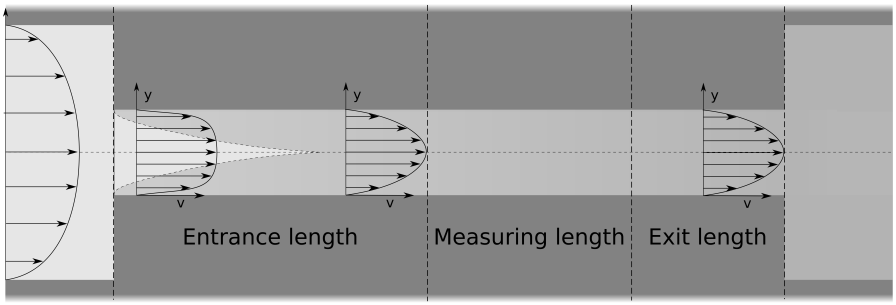

Figure D.3: Channel design.

Measurement length

The length between the sensors determines what the measured pressure drop is. This length has to be designed such that the highest viscosity targeted, creates a pressure drop which does not exceed the maximum pressure limit of the sensors.

$$\tau_{\max} = \eta_{\text{target}} \dot{\gamma}_{\text{target}} \tag{D.29}$$

$$\tau_{\max} = \frac{wh}{2(w+h)} \frac{\Delta p_{\max}}{L_{\text{meas}}} \tag{D.30}$$

$$\Delta P_{\max} = \tau_{\max} L_{\text{meas}} \frac{2(w+h)}{wh} \tag{D.31}$$

Exit length

The exit length has little effect on the flow in the channel. Special exit geometry is only required for polymer fluids to compensate for die swell. Increasing the exit length increased the required inlet pressure. However, by extending the exit length the MR fluid can be drained from the channel and is more easily accessed.

D.1.6 Pressure development

With the lengths of the channel as variables, the pressure drop through the system can be calculated. The velocity of the fluid is constant through the microchannel. The pressure required at the beginning of the microchannel can be estimated. An important factor is the undeveloped flow at the entrance of the slit. The flow is developing and has a larger pressure drop than the fully developed flow. A factor for the extra pressure drop is added, equation D.32, [22].

$$K \approx 0.42 \left(1 - \frac{d^2}{D^2}\right) \tag{D.32}$$

The rest of the developed flow follows the pressure shear relation in equation D.1.

$$P_{\text{ex}} = 0 \tag{D.33}$$

$$P_{\text{meas,out}} = P_{\text{ex}} + \frac{\tau_{\max} 2(w+h) L_{\text{ex}}}{wh} \tag{D.34}$$

$$P_{\text{meas,in}} = P_{\text{measure,out}} + \frac{\tau_{\max} 2(w+h) L_{\text{measure}}}{wh} \tag{D.35}$$

$$P_{\text{e}} = P_{\text{meas,in}} + \frac{\tau_{\max} 2(w+h) L_e}{wh} + \frac{\rho K v_{\text{mean}}^2}{2} \tag{D.36}$$

$$P_{\text{e}} = \text{Total pressure drop} \tag{D.37}$$

The problem to be solved is to choose the variables in such a way that the total pressure is realistic and does not exceed the pressure supplied by the actuation system. By evaluating the effect of the height of the microchannel, the width of the microchannel, and the measuring length the range of the slit rheometer can further be determined. One crucial aspect is the sensing. The sensors must be able to sense a differential pressure.

Sensitivities

The sensitivity of the Nahme number, Reynolds and the total pressure:

$$d_h = \frac{2wh}{(w+h)} \Rightarrow h \propto d_h \tag{D.38}$$

$$\text{Re} = \frac{\rho w h^2 \dot{\gamma}_{\text{app}}}{3\eta(w+h)} \Rightarrow h \propto \text{Re} \tag{D.39}$$

$$\text{Na} = \frac{\beta h^2 \dot{\gamma}^2}{k} \Rightarrow h^2 \propto \text{Na} \tag{D.40}$$

$$L_e = d_h \left(\frac{0.6}{1 + 0.035\text{Re}_{\max}} + .056\text{Re}_{\max} \right) \Rightarrow h \propto L \tag{D.41}$$

$$P_{\text{total}} = P_{\text{ex}} + \frac{\tau_{\max} 2(w+h)}{wh} (L_{\text{e}} + L_{\text{measure}} + L_{\text{ex}}) + \frac{\rho K V^2}{2} \Rightarrow \frac{1}{h} \propto P \tag{D.42}$$

$$P_{\text{total}} = \frac{\tau_{\max} 2(w+h)}{wh} \left(d_h \left(\frac{0.6}{1 + 0.035\text{Re}_{\max}} + .056\text{Re}_{\max} \right) + L_{\text{measure}} + L_{\text{ex}} \right) + \cdots \tag{D.43}$$

$$\frac{\rho K \left(\frac{h\dot{\gamma}_{\text{app}}}{6} \right)^2}{2} \Rightarrow \frac{1}{h}(h + C_1 + C_2) \propto P$$

Through this we can see how the height affects the range and the pressure. Due to the fluid it is unwanted to reduce the gap too much. As the particles inside are in the range of 1 nm to 1 µm and form chains. Thus if the gap is too small the chains cannot form. For the Reynolds and Nahme number it is beneficial to reduce the gap as larger gap means more turbulence and more heat being generated. Furthermore decreasing the gap increases the required pressure.

D.1.7 Dimensions

The dimensions to determine are the entrance length, measurement length, exit lengths and the gap height and width of the channel. The entrance length is a function of the height, equation D.27. The measuring length is set to 1 mm. This length results in a clear pressure drop and visual separation between the channels. The exit length is set to 0.2 mm. This length allows the sensor channel strength. The gap height has a lower limit of 20 µm as the particles in the MR fluids are about 1 µm in diameter and the ratio between particles and gap height has to be at least 1:10, [48]. This gap height is also required to allow the fluid to form chains. With the measuring length and exit length determined, the remaining variables are the gap height and the width. The width is less significant to the system and mostly contributes to the flow rate and is only limited by the minimal aspect ration of 1:10,[[44], [45]]. Therefore the critical parameter is the gap height. The pressure and measuring range are calculated for a minimal gap height.

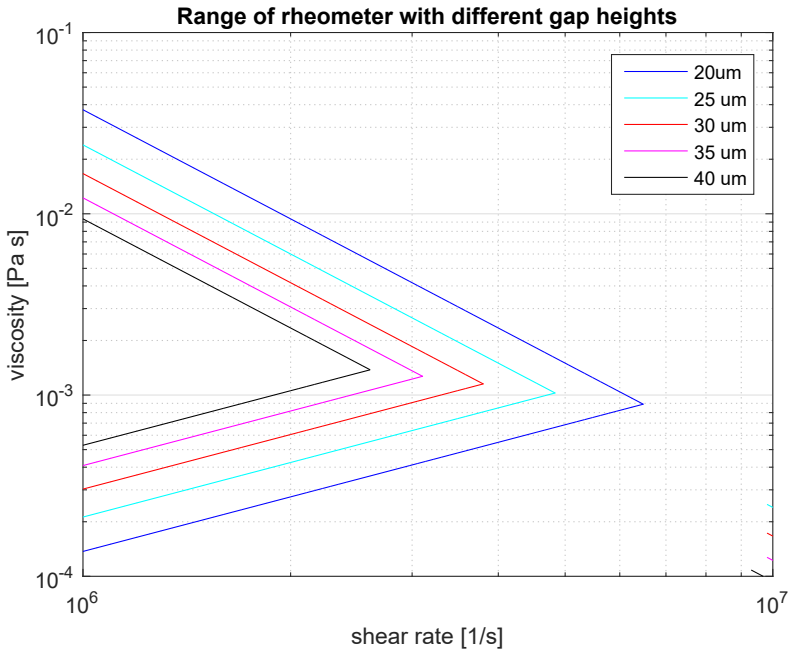

Figure D.4: Measuring range in the microchannel for different gap heights.

Gap height	Max pressure	η min at 10^6 s^{-1}	η max at 10^6 s^{-1}
20 µm	112.90 bar	0.14 mPas	37.5 mPas
25 µm	66.57 bar	0.21 mPas	24 mPas
30 µm	43.65 bar	0.30 mPas	16.67 mPas
35 µm	30.78 bar	0.41 mPas	12.25 mPas
40 µm	22.89 bar	0.53 mPas	9.37 mPas

Table D.1: Characteristic values.

The goal is to create a range of viscosities at the shear rate of $10^6\,s^{-1}$ while having reasonable pressures at the entrance. The choice is made to use a height of 35 µm. Lastly, the width of the channel determines the fluid flow required. These can be calculated with equation D.44.

$$Q = \frac{\dot{\gamma} w h^2}{6} = \frac{10^6 \times w \times \left(35 \times 10^{-6}\right)^2}{6} = 204.1667 \times 10^{-6} w \tag{D.44}$$

The fluid flow in equation D.44 has to be realised while applying the maximum required pressure. As the flow needs to be constant for a certain amount of time to let the dynamics damp out. The width of the channel is, therefore, connected to the actuation mechanism. The pumping mechanism is further detailed in section E.3.1. The resulting width of the microchannel is 0.5 mm. The dimensions are summarised in table D.2. The final working range of the rheometer can be seen in figure D.5

Dimension	**Size**
Channel cross section	500 µm × 35 µm
Entrance length	3.7 mm
Measuring length	1 mm
Exit length	0.2 mm

Table D.2: Final dimensions slit assembly.

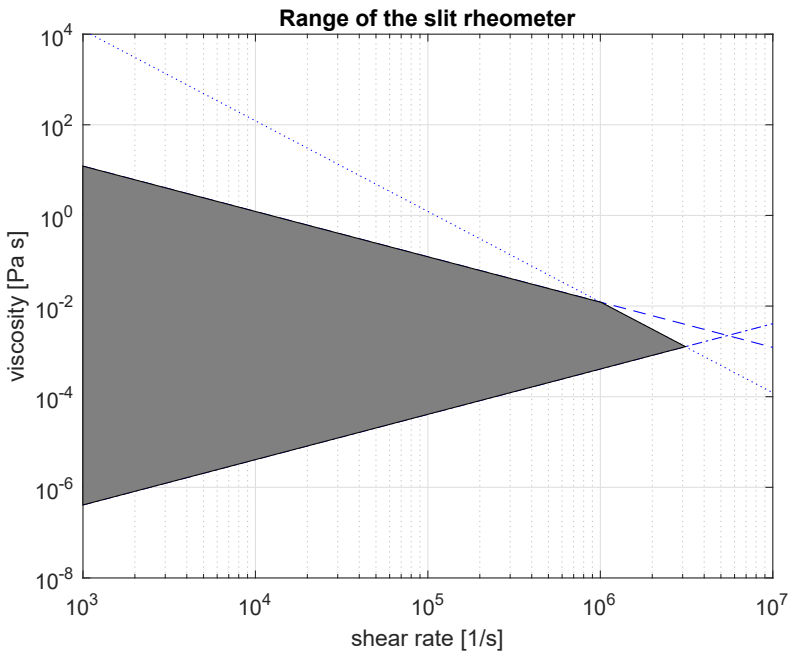

Figure D.5: Working range of the designed microslitrheometer.

D.2 Magnetic system design

To design the magnetic system a couple of requirements have to be met. The field must reach a magnetic field density of 1 T. Furthermore the field has to be homogeneous. The variation of the field must be less than 1 % over the measurement area. Lastly the generation of the field must not interfere with the measurement system. An example of an interference would be heating due to temperature raise of the magnetic system. In order to meet these requirements the design is set up in 5 stages.

1 Core design

2 Pole analysis

3 Coil design

4 Dimensions

5 Manufacturing

D.2.1 Core design

The function of the core is to guide the magnetic field and amplify it. Due to the small area requiring a magnetic field the core is used to focus the field. The core should allow for space to wind coils and must be made from soft magnetic material. The core can be set up in multiple ways. It is important to deliver a homogeneous magnetic field and a strong enough magnetic field. A factor in the homogeneity is symmetry. Multiple core designs have been considered.

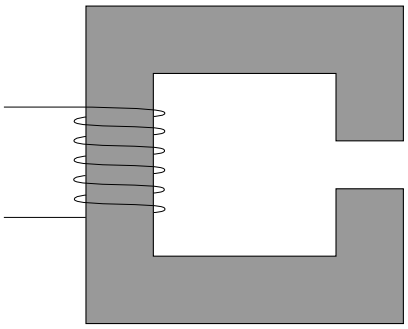

(a) C-core

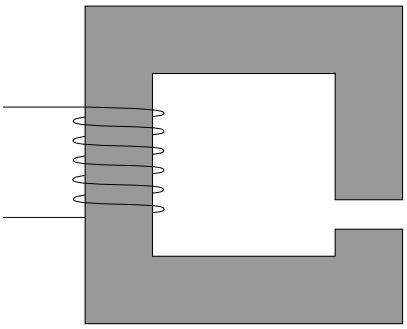

(b) C-core non symmetric

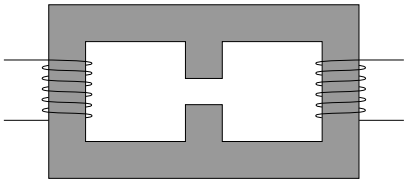

(c) E-core

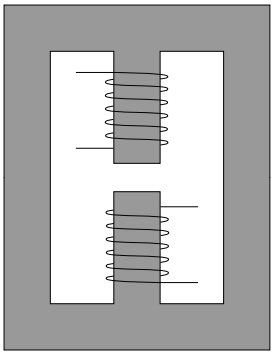

(d) E-core

A symmetric design is chosen as it provides a more homogeneous field. The coils are placed close to the target location to increase the field strength. This shape is commonly seen in transformers to create high field densities and reduce losses. These cores are generally more complex than the design in figure D.6d. The transformer cores are optimised for different load cases, figure D.7. The design of the cores will improve the field in the system, however the accessibility is reduced. Therefore, in the design of the prototype a simple E-core will be used to apply the magnetic field.

(a) E core (b) Pot core (c) PQ core

Figure D.7: Core types currently used in industry.

D.2.2 Pole analysis

The pole points have a large influence on the field emerging from it. By adding and removing material one can increase and decrease the density of the field. The general shape of the pole is a piece a flat area. The field emerging from such a pole piece can be seen in figure D.9a. As we can see in figure D.9a the field is reasonably homogeneous however it is slightly stronger in the centre and falls off along the edges. An optimization can be made of the strength of the field and the homogeneity. This has been done in [49] for a round pole piece of an MRI machine. The resulting shape can be seen in figure D.8. The field at the edges has been increased by reducing the reluctance between the pole pieces around the edges. The centre has a light inward curvature to generate a flat field density. An analysis is made in COMSOL Multiphysics to verify the potential benefit.

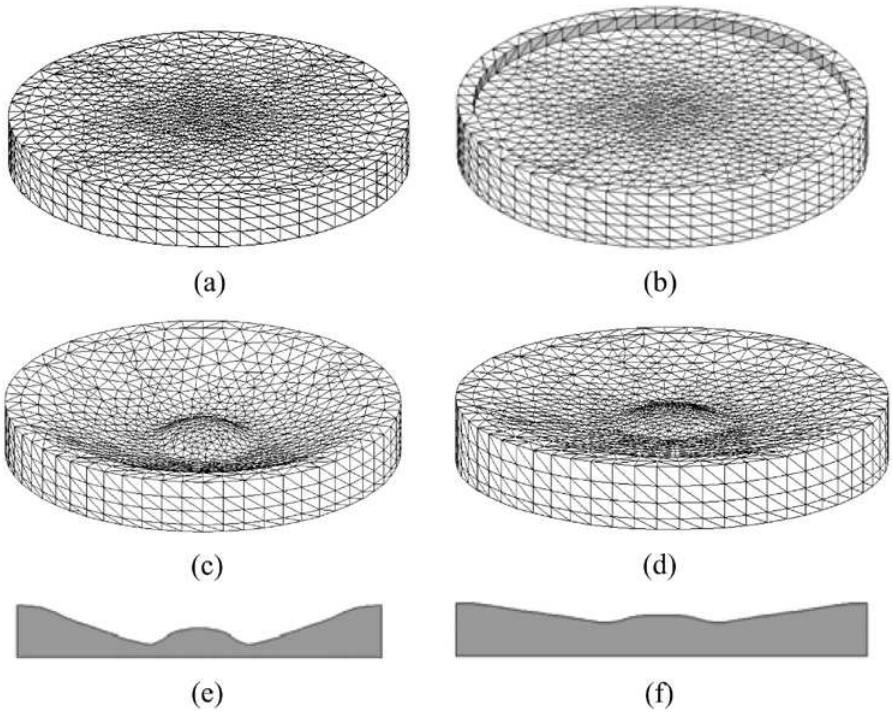

Figure D.8: Optimal profile with maximum homogeneity and field strength, (a) initial flat pole piece; (b) shimmed pole piece; (c) linear optimized pole piece; (d) non-linear optimized pole piece; (e) cross-sectional view of (c); (f) cross-sectional view of (d); [49]

This shape has been copied and simulated to see potential improvement for different height differences. The shape does effect the homogeneity, however, the extra effort required to form the pole pieces does not outweigh the improvement of the field. As the field fluctuation is below 1 % the choice is made to keep the surface flat. If further homogeneity is required the poles can be adjusted.

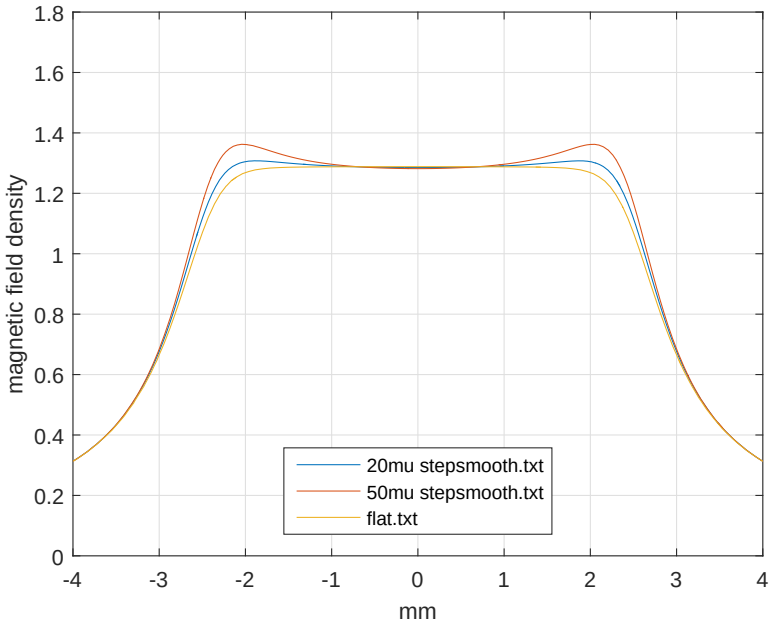

(a) Magnetic field density on the centreline of the gap for different pole profiles.

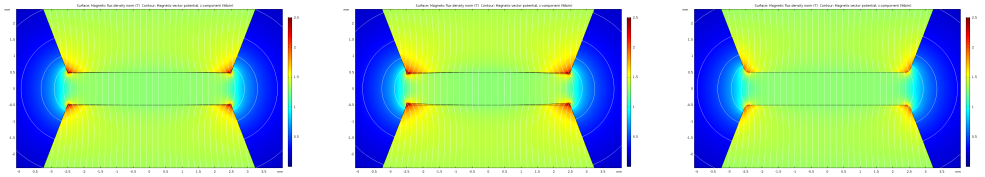

(b) Magnetic field density of a 20 µm pole piece.

(c) Magnetic field density of a 50 µm pole piece.

(d) Magnetic field density of a flat pole piece.

Figure D.9: Magnetic field density of different pole pieces 2D COMSOL simulation.

From figure D.9a it is clear the flat pole results in a flat field density in the centre. By designing the core larger than the microchannel will result in a homogeneous field over the microchannel. The small adjustment of 20 µm does improve the homogeneity. To complete the pole analysis the effect of the microchannel filled with magnetic particles is researched. The magnetic particles in the microchannel will have an influence on the field in the channel as the magnetic particles guide the field. A simulation is made to analyse the effect. The simulation uses an exaggeration of the iron particles by replacing the channel with an iron plate in the same dimensions. In figure D.10a the effects of the iron plate can be seen for the different pole profiles.

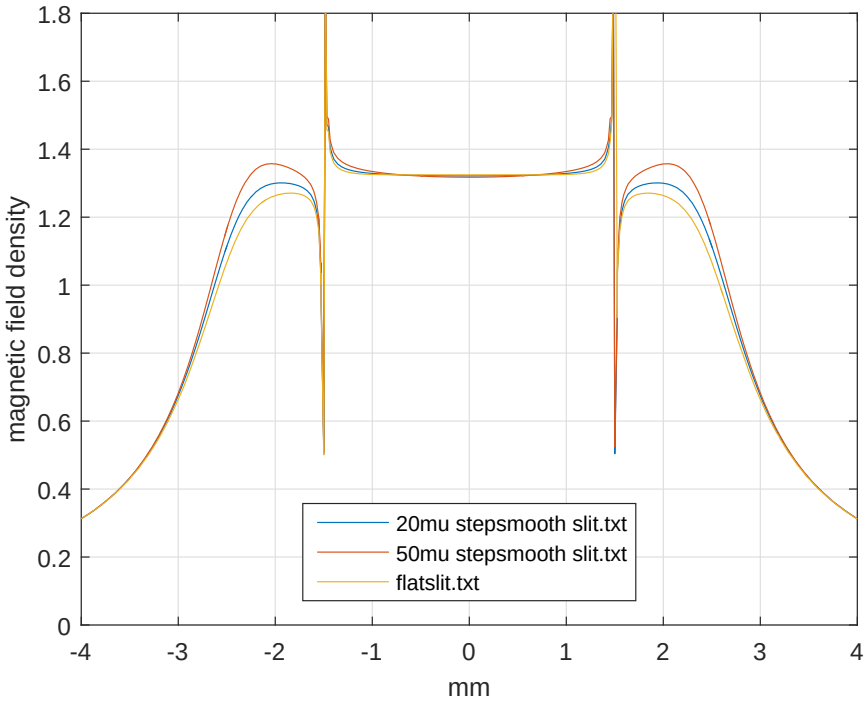

(a) Magnetic field density on the centreline of the gap for different pole profiles with iron slit.

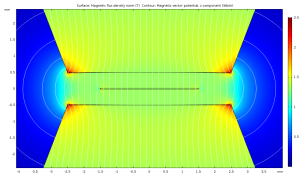

(b) Magnetic field density of a 20 µm pole piece.

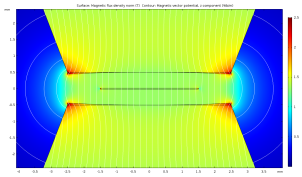

(c) Magnetic field density of a 50 µm pole piece.

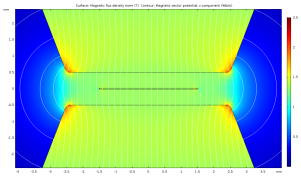

(d) Magnetic field density of a flat pole piece.

In figure D.10a, two points of irregularity can be seen. These peaks are caused by the iron plate having sharp edges. In reality these are rounded which will reduce the peaks. Furthermore the simulation is 2D which exaggerates the discontinuity. On the area represented by the microchannel the standard deviation is about 0.008 T which shows the field is homogeneous over the area in the microchannel, figures [D.11a,D.11c,D.11e]. A 3D simulation is made to verify the homogeneity over the entire measuring length.

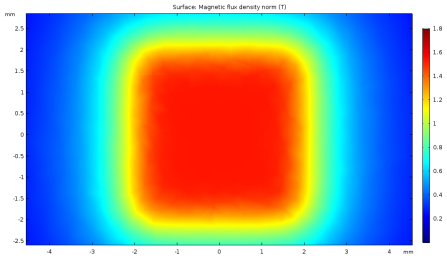

(a) Magnetic field density in the xy plane

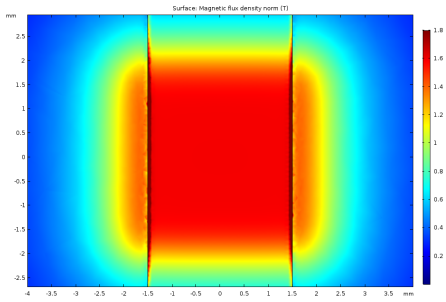

(b) Magnetic field density in the xy plane with microchannel.

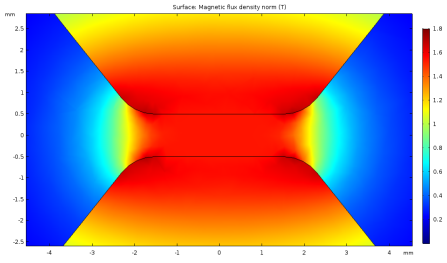

(c) Magnetic field density in the xz plane

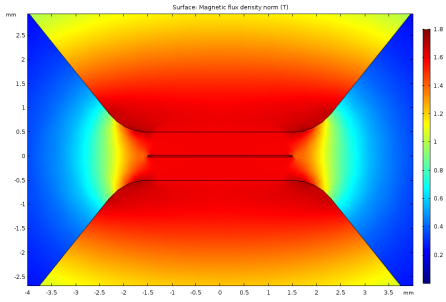

(d) Magnetic field density in the xz plane with microchannel.

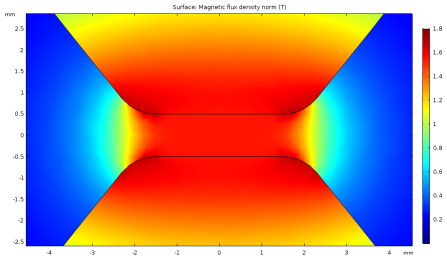

(e) Magnetic field density in the yz plane.

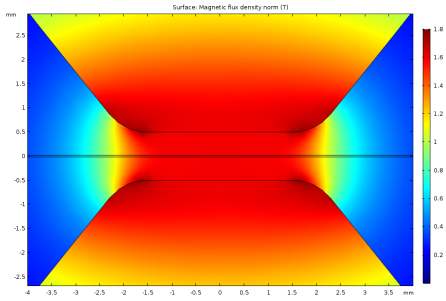

(f) Magnetic field density in the yz plane with microchannel.

Figure D.11: Magnetic field density of a 3D COMSOL simulation. Figures D.11aD.11c D.11e are simulated without microchannel.

The results of the 3D simulation can be seen in figures [D.11b, D.11d, D.11f]. The microchannel does have an influence on the field. Along the edges located in the field a discontinuity is visible. This further visualised in figure D.12. The region after this discontinuity is smooth. In the measuring principle the aspect ratio of the slit was made sufficiently large, section D.1, to make the edge effects negligible. This is the same area where the field is not homogeneous, and therefore will not influence the measurement as this area already doe not have an effect on the flow. The standard deviation on the slit surface is 0.15 T. When neglecting the discontinuity and only taking into account the measuring surface reducing the x area by 200 µm, the standard deviation is reduced to 0.0023 T. From the simulations it can be concluded that the flat profile is sufficiently distributing the field. Furthermore, the area of

the pole piece should be larger than the microchannel. This results in a homogeneous field over the channel.

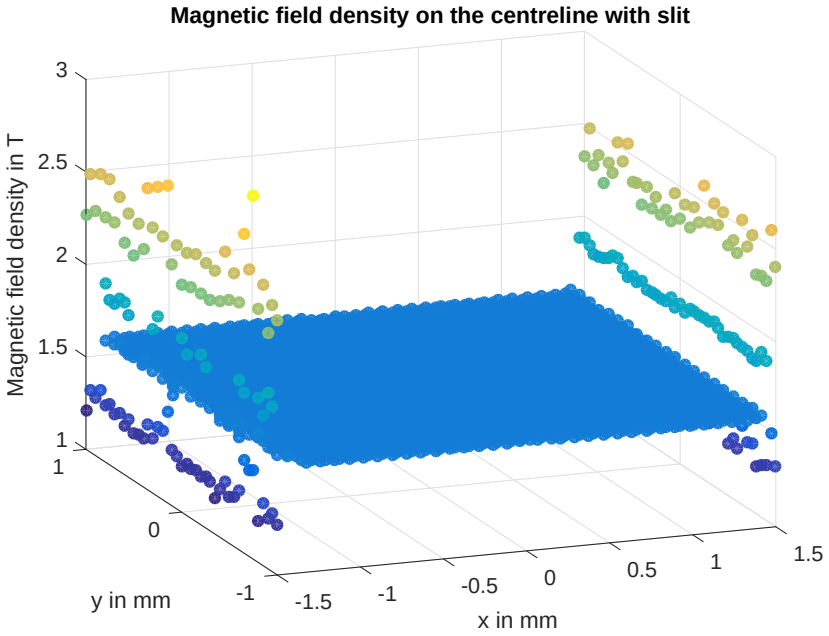

Figure D.12: Magnetic field density data points on centreline with iron slit.

D.2.3 Coil design

Now the shape of the core has been determined. The actuation of the core has to be designed. The dimensions of the coils need to be found. The coils are required to provide a field of 1.5 T over the microchannel. This must minimally be provided by the coil. There are magnetic losses in the core. These need to be compensated by the coil to provide enough magnetic field to the slit. An important factor in the design of the coil are temperature due to Joule heating and the required electrical power. The field in a coil can be found by the enclosed current. The generated field can be related to the electrical losses for a fixed volume, equation D.45. The long solenoid equation is used as the solenoid used is about 40 mm long.

$$B = \frac{(\mu_0 \mu_r N I_{\text{enc}})}{l} \tag{D.45}$$

$$\text{Magnetomotive force} = \mathscr{F} = NI = \Phi R = HL \tag{D.46}$$

$$P_{\text{loss}} = RI^2 = \frac{U^2}{R} \tag{D.47}$$

$$R = \frac{(\rho_{\text{res}} l)}{A_{\text{wire}}} = \frac{(\rho_{\text{res}} 2\pi R_{\text{coil}})}{A_{\text{wire}}} \tag{D.48}$$

$$V_{\text{wire}} = 2\pi R_{\text{coil}} A_{\text{wire}} N \tag{D.49}$$

$$R_{\text{fixed volume}} = \frac{\rho_{\text{res}} (2\pi R_{\text{coil}} N)^2)}{V_{\text{wire}}} \tag{D.50}$$

$$\frac{\mathscr{F}}{P_{\text{loss}}} = \frac{NI}{RI^2} = \frac{N}{RI} = \frac{N}{U} \tag{D.51}$$

$$\tag{D.52}$$

This shows that to increase the magnetic field inherently means increasing the heating of the system. The main variables in this balance are the amount of windings N, the current I and the electrical resistance R. To find the values of variables an approximation of the total system is needed. To approximate the distribution of the field an electric circuit equivalent can be created where the flux is the current and magneto motive force is the voltage sources. The reluctance can be seen as the resistances. This has been visualised in figure D.13.

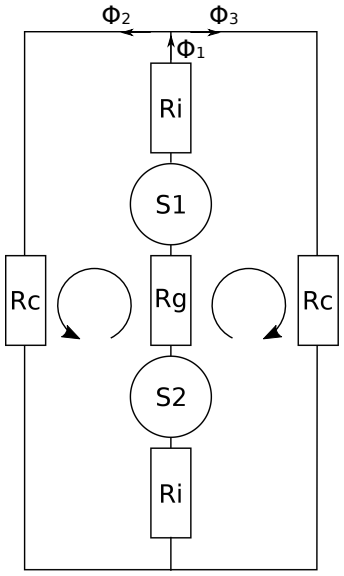

Figure D.13: Magnetic circuit.

$$\mathscr{F} = S = \Phi \mathscr{R} \tag{D.53}$$

$$R = \frac{1}{(\mu_0 \mu_r)} \frac{l}{A} \tag{D.54}$$

$$\Phi = B_{\text{field}} A \tag{D.55}$$

Figure D.14: Electrical equivalent of magnetic field density through a yoke.

The resistances and sources can be calculated and the flux in the gap is prescribed. Therefore the magneto motive force can be determined. The relative permeability is taken of iron as 5000.

$$B_{\text{gap}} = 1.5\,\text{T} \tag{D.56}$$

$$A_{\text{gap}} = 4\,\text{mm} \times 2\,\text{mm} = 8\,\text{mm}^2 = 8 \times 10^{-6}\,\text{m}^2 \tag{D.57}$$

$$A_{\text{core}} = 20\,\text{mm} \times 30\,\text{mm} = 600\,\text{mm}^2 = 600 \times 10^{-6}\,\text{m}^2 \tag{D.58}$$

$$R_c = \frac{1}{(\mu_0\mu_r)}\frac{l}{A_{\text{core}}} = \frac{1}{(4\pi \times 10^{-7})5000}\frac{0.2020}{6 \times 10^{-4}} = 8.0373 \times 10^4\,\text{H}^{-1} \tag{D.59}$$

$$R_i = \frac{1}{(\mu_0\mu_r)}\frac{l}{A_{\text{core}}} = \frac{1}{(4\pi \times 10^{-7})5000}\frac{0.070}{6 \times 10{-}4} = 1.3754 \times 10^4\,\text{H}^{-1} \tag{D.60}$$

The reluctance of the air gap is more complicated as fringe fields occur around the gap. To approximate the fringe fields equation D.61 is used from [50].

$$R_g = \frac{1}{\mu_0}\frac{1}{\frac{A_{\text{gap}}}{l_{\text{gap}}} + \frac{2w}{\pi}\left(1 + \ln\frac{\pi h}{2l_{\text{gap}}}\right)} = \frac{1}{4\pi \times 10^{-7}}\frac{3 \times 10^{-3}}{2.7 \times 10^{-5}} = 6.7655 \times 10^7\,\text{H}^{-1} \tag{D.61}$$

Using Kirchof rules the flux can be determined.

$$\left.\begin{aligned} \Phi_2 R_c + (2R_i + R_g)\Phi_1 &= S_1 + S_2 \\ \Phi_3 R_c + (2R_i + R_g)\Phi_1 &= S_1 + S_2 \\ \Phi_1 &= \Phi_2 + \Phi_3 \end{aligned}\right\} \Phi_2 R_c + (2R_i + R_g)\Phi_1 = 2S_1 \tag{D.62}$$

$$\left.\begin{aligned} \Phi_1 = B_{gap}A_{gap} &= 1.2 \times 10^{-5}\,\text{Wb} \\ \Phi_2 &= 0.5\Phi_1 \\ \Phi_2 R_c + (2R_i + R_g)\Phi_1 &= 2S_1 \end{aligned}\right\} (0.5R_c + 2R_i + R_g)\Phi_1 = 2S_1 = 813.8672\,\text{A} \tag{D.63}$$

$$S_1 = 406.9 = NI = \mathscr{F} \tag{D.64}$$

$$I = 1A \tag{D.65}$$

$$N = 407 \tag{D.66}$$

The model made underestimates the reality. The model uses a fixed permeability and does not take into account saturation of the material. Furthermore, the model does not reflect the core losses. Therefore, the amount of windings is set to 400 and the current source used provides up to 3 A. This results in a full system design which can be simulated in COMSOL Multiphysics.

One important factor with the coils is that they generate heat. Due to the resistance in the wires the temperature can increase significantly. Therefore, the heat generation is calculated and simulated to determine what effect the field has. The surface heat transfer coefficients are calculated and solved for different times. Firstly the heat generation is calculated. Equation D.67 shows the resistance of the coil wire. The resistance loses its energy by heat. Therefore, the heat generation is the power put into the resistance.

$$R_e = \frac{l_{\text{wire}}\rho_{\text{e}}}{A_{\text{wire}}} \tag{D.67}$$

$$R_e = \frac{2\pi R_{\text{coil}}\rho_{\text{e}}}{\pi R_{\text{wire}}^2} \tag{D.68}$$

$$P_{\text{heat}} = R_e I^2 \tag{D.69}$$

With 400 windings and a wire diameter of 0.5 mm the heat generated at 1 A is 3.5 W. The heating is cooled naturally by air flowing around the coil. The formulas for the heat transfer around the core are listed in equation D.70. σ_s is the Stefan–Boltzmann constant.

$$\rho c \frac{dT}{dt} = \dot{Q}_{\text{transfer}} + \dot{Q}_{\text{generation}} \tag{D.70}$$

$$\dot{Q}_{\text{transfer}} = q_{\text{convection}} A + q_{\text{conduction}} A + q_{\text{radiation}} A \tag{D.71}$$

$$q_{\text{convection}} = h_t \Delta T \tag{D.72}$$

$$q_{\text{conduction}} = k \frac{dT}{dx} \tag{D.73}$$

$$q_{\text{radiation}} = \epsilon \sigma_b \left(T_a^4 - T_b^4\right) \tag{D.74}$$

$$\text{Ra}_l = \text{GrPr} \tag{D.75}$$

The heat transfer is natural convection on differently orientated walls. vertical or inclined (ϕ) wall:

$$h_t = \begin{cases} \frac{k}{l}\left(0.68 + \frac{0.67(\cos(\phi))\text{Ra}_l^{\frac{1}{4}}}{\left(1+\left(\frac{0.492k}{\mu c_p}\right)^{\frac{9}{16}}\right)^{\frac{4}{9}}}\right) & \text{if } \text{Ra}_l \leq 10^9 \\ \frac{k}{l}\left(0.825 + \frac{0.387\text{Ra}_l^{\frac{1}{6}}}{\left(1+\left(\frac{0.492k}{\mu c_p}\right)^{\frac{9}{16}}\right)^{\frac{8}{27}}}\right) & \text{if } \text{Ra}_l \geq 10^9 \end{cases} \tag{D.76}$$

(D.77)

Horizontal plate upside:

$$h_t = \begin{cases} \frac{k}{l}0.54\text{Ra}_l^{\frac{1}{4}} & \text{if } T > T_{\text{ext}} \text{ and } 10^4 \leq \text{Ra}_l \leq 10^7 \\ \frac{k}{l}0.15\text{Ra}_l^{\frac{1}{3}} & \text{if } T > T_{\text{ext}} \text{ and } 10^7 \leq \text{Ra}_l \leq 10^{11} \\ \frac{k}{l}0.27\text{Ra}_l^{\frac{1}{4}} & \text{if } T \leq T_{\text{ext}} \text{ and } 10^5 \leq \text{Ra}_l \leq 10^{10} \end{cases} \tag{D.78}$$

(D.79)

Horizontal plate downside:

$$h_l = \begin{cases} \frac{k}{l} 0.54 \mathrm{Ra}_l^{\frac{1}{4}} & \text{if } T \leq T_{\text{ext}} \text{ and } 10^4 \leq \mathrm{Ra}_l \leq 10^7 \\ \frac{k}{l} 0.15 \mathrm{Ra}_l^{\frac{1}{3}} & \text{if } T \leq T_{\text{ext}} \text{ and } 10^7 \leq \mathrm{Ra}_l \leq 10^{11} \\ \frac{k}{l} 0.27 \mathrm{Ra}_l^{\frac{1}{4}} & \text{if } T > T_{\text{ext}} \text{ and } 10^5 \leq \mathrm{Ra}_l \leq 10^{10} \end{cases} \tag{D.80}$$

(D.81)

After applying these equations to the system, the equation can be solved for the temperature at different times and the steady state temperature, figure D.15.

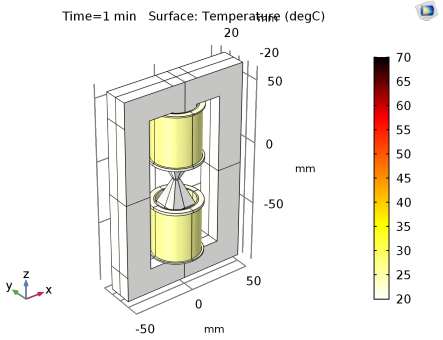

(a) Temperature distribution after 1 minute.

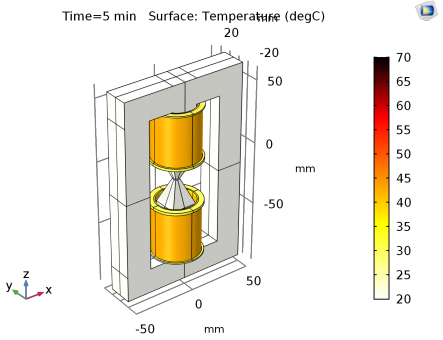

(b) Temperature distribution after 5 minute.

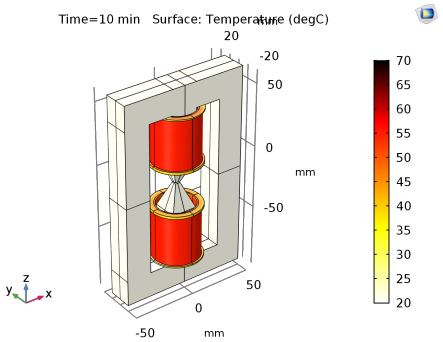

(c) Temperature distribution after 10 minute.

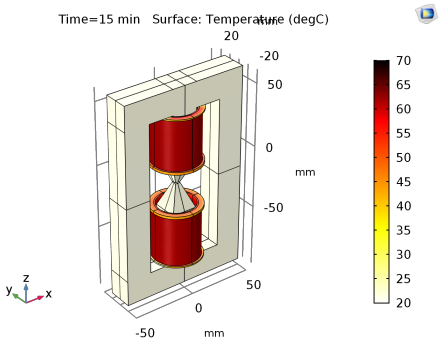

(d) Temperature distribution after 15 minute.

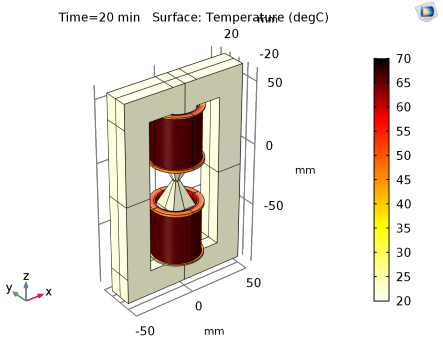

(e) Temperature distribution after 20 minute.

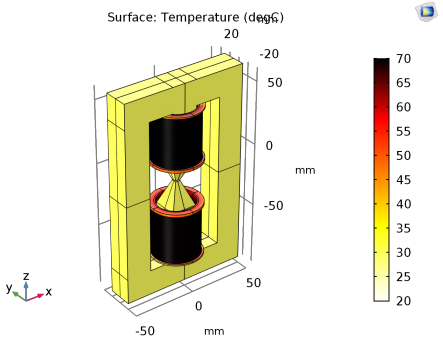

(f) Temperature distribution steady state

Figure D.15: Temperature distribution in the magnetic core due to the coils at different times.

The temperature at the chip at the steady state is 29.8 °C. This is at the steady state. The temperature change after 1 minute which is about the time for one measurement is 20 °C. The temperature at the different time intervals is given in table D.3.

Time	Temperature
60 s	20.006 °C
300 s	20.266 °C
600 s	20.794 °C
900 s	21.419 °C
1200 s	22.073 °C

Table D.3: Temperatures at different times when the coils are at full power.

As long as the coils are not used at full power constantly the temperature should not effect the measurement. The simulation assumes natural convection. In practice more airflow is present increasing the heat transfer coefficient. Furthermore the area dissipating the heat is assumed flat. The wires create a larger surface area giving more area to dissipate heat. Therefore, more heat can be transferred out of the system.

D.2.4 Dimensions

The dimensions of the designs are partly chosen and partly derived. Limitations in production techniques requires certain dimensions and will be highlighted in this section. Firstly, the dimensions of the core were chosen. From the equations D.56 a large core size results in lower reluctance which enables lower amount of magnetomotive force, which means less current or windings required. However, this is balanced by the larger size means more wire per winding and thus more resistance and thus heating. Furthermore, a small area was required at the gap due to the flux, equation D.62, as this reduces the required flux and is dominant over the smaller area and thus smaller reluctance at the gap. The coils have to be fitted around the coil. The coil radius is therefore 15 mm as to fit snugly around the core. A bobbin is used to support the coil therefore the radius of the windings is 16 mm. To fully use the field generated by the coils the shape of the the core in the coil is made round. The final dimensions are in table D.4 and a 3D drawing of the core can be seen in figure E.24a.

Dimension	Size
Pole size	2 mm × 4 mm
Core cross section	20 mm × 30 mm
Gap size	3 mm
Core width	100 mm
Core height	162 mm
Coil length	40 mm
Coil diameter	32 mm
Coil wire core diameter	0.5 mm
Coil wire diameter	0.553 mm

Table D.4: Final dimensions magnetic core.

D.3 Design

To demonstrate the concept, a prototype is built. The prototype will only measure part of the designed range of the concept as the available pump is limited in pressure, section E.3.1. The limited pump pressure results in the measuring range shown in figure D.16.

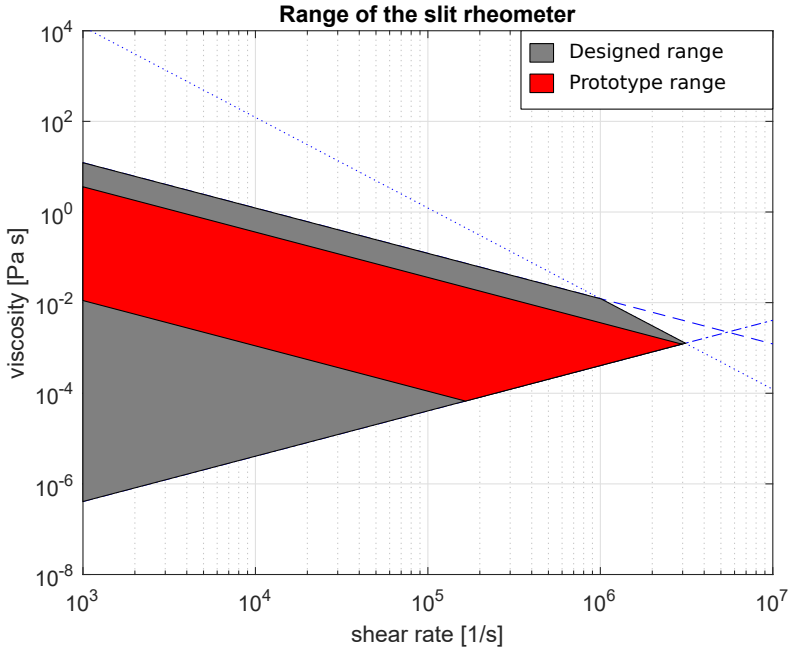

Figure D.16: Prototype working range.

The sensors have to be connected to the microchannel. This is complicated due to the designed core limiting the accessibility. Furthermore, the manufacturing techniques have to allow for the connections to be made, section E.1. The manufacturing results in a layered design, with 1 mm thickness, which means the connections are to be made out of plane. The thickness of 1 mm is chosen as this is the thinnest PMMA sheets available. To create space for these connection sensor channels have been added to the microchannel, figure D.17. The openings into the measuring channel are made square to restrict disruption of the flow in the channel. The openings to the sensor channel slightly distort the flow. The sensor channels are placed on either side of the channel in order to have clean unaffected flow passing the sensor channels, figure D.17.

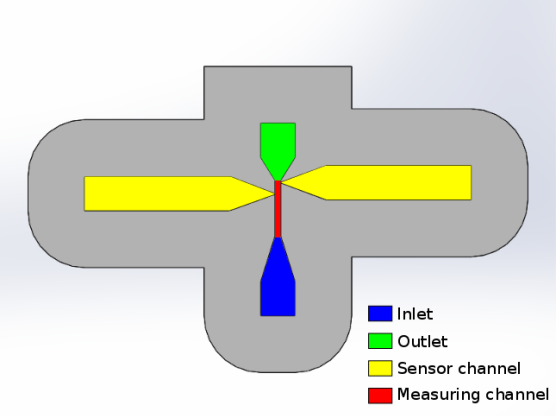

Figure D.17: CAD design of the chip.

The sensor channels cannot be as thin as the microchannel itself as this would create a large pressure drop when fluid flows through it. Therefore, the sensor channels are cut out of the sealing layer 2. A third layer is added on top to seal the sensor channels. The sensor channels will be 1 mm high. A fourth layer is added to create contact area for the connectors. A hole is cut out in this layer to allow the magnetic core to be close to the measuring channel and to function as a positioning guide. The resulting layered design can be seen in figure D.18 as an exploded view.

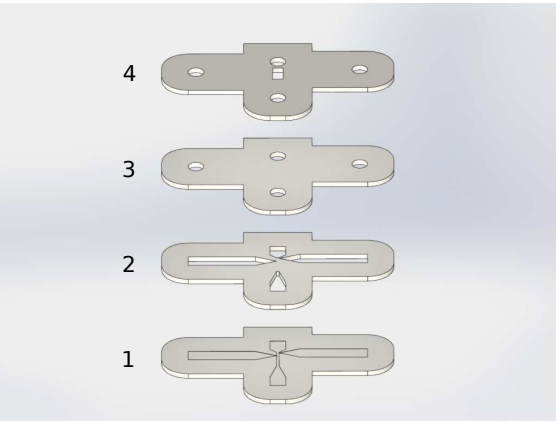

Figure D.18: 3D CAD exploded view of the chip.

The chip is actuated by a syringe pump. The sensing is done by two external sensors. A 3D model of the prototype setup is presented in figure D.19.

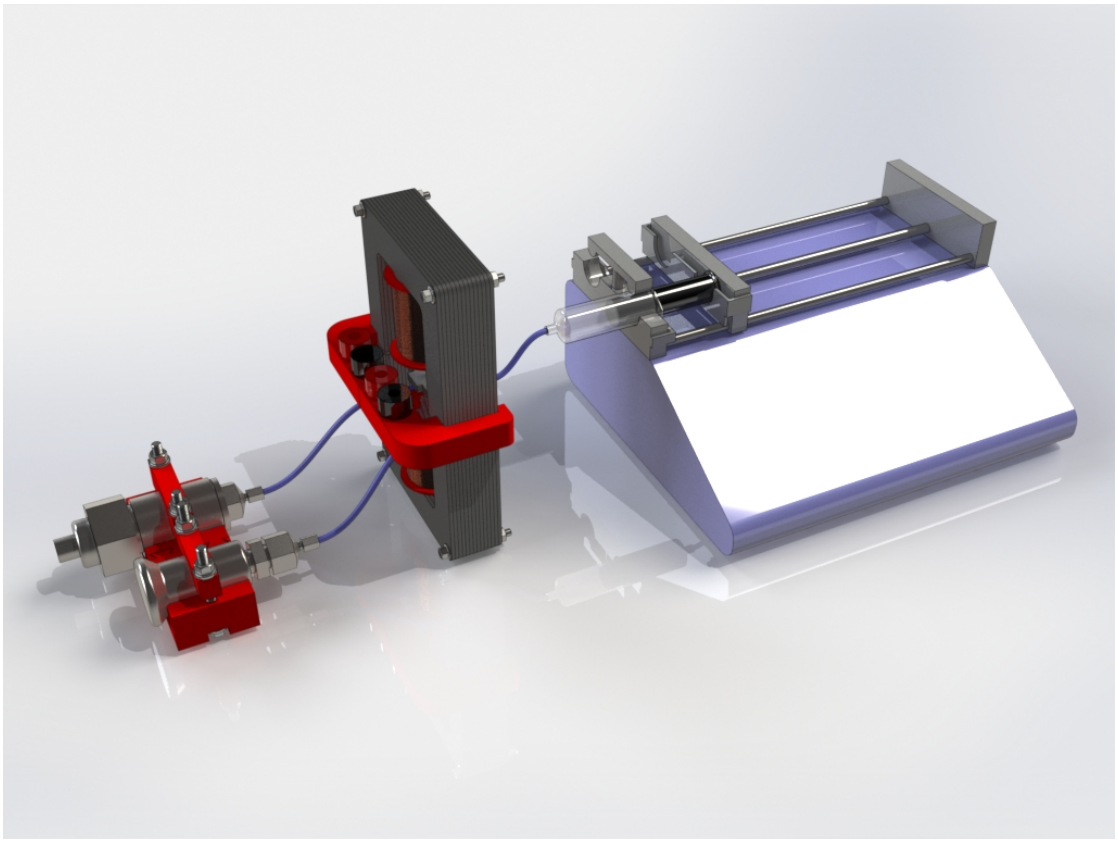

Figure D.19: 3D CAD render of total test setup.

Appendix E

Manufacturing

E.1 Chip manufacturing

Due to the multilayer design, a fabrication technique is required where the layer can be bonded to each other. A commonly used technique for fast prototyping of microfluidics devices is hot embossing. Hot embossing consists of a pressing a stamp(master) into a polymer material. The polymer forms a negative of the stamp. The polymer can then be bonded to another layer. Using hot embossing results in a cost effective way to quickly prototype. The fabrication of the chip contains three parts.

a. Master fabrication

b. Hot embossing

c. Bonding

E.1.1 Master fabrication

Manufacturing using common machining techniques does not meet the required length scales. Therefore, micromachining techniques are required. There are two types of masters: hard and soft masters. A hard master is made of a strong material such as silicon, glass or metals. The hard master maintains its shape during the embossing process. A soft master deforms during the embossing process. A common way to manufacture hard masters is chemical etching in silicon, [51]. In this technique lithography is used to determine the to be chemically etched features. The etching is done with acids such as potassium hydroxide or using plasma etching. A common soft master is SU-8, a photoresist layer,[31]. The SU-8 is spincoated on the substrate to the thickness required. The photoresist is developed in the pattern required using lithography and cured. The excess photoresist is etched away.
The first challenge in manufacturing a master is to create the channel depth of 35 µm. The lithography and etching processes are cumbersome, expensive and mostly used for large batch production. Another upcoming technique is micro machining. Micro machining is the removal of material on very small scale. A field showing potential is laser etching. By using picosecond pulses material is ablated from the surface. This method could potentially remove the material and create the microchannel,[30]. Due to the availability of the laser and the repeatability of the process the laser

etching of the master is researched. Since the master is used to replicate its inverse pattern, the etched surfaces are the bonding surfaces. This means that the surface is not limiting the quality of the microchannel. The microchannel is embossed with the polished silicon surface. For the bonding: the smoother the surface, the easier the bonding.

Laser etching channel The laser is a SpectraPhysics Q-switched Talon laser 355-15 with maximum output of 15 W at 50 kHz repetition frequency and with 13 W at 100 kHz. The maximum frequency is 500 kHz with a pulse width of 35 ns. Firstly the laser etching is tested to find the parameters to reach the 35 µm depth with low roughness. A line pattern is programmed and cut, figure E.1. The parameters varied are laser power and repetitions. The pattern is then cleaned in an ultrasonic cleaner.

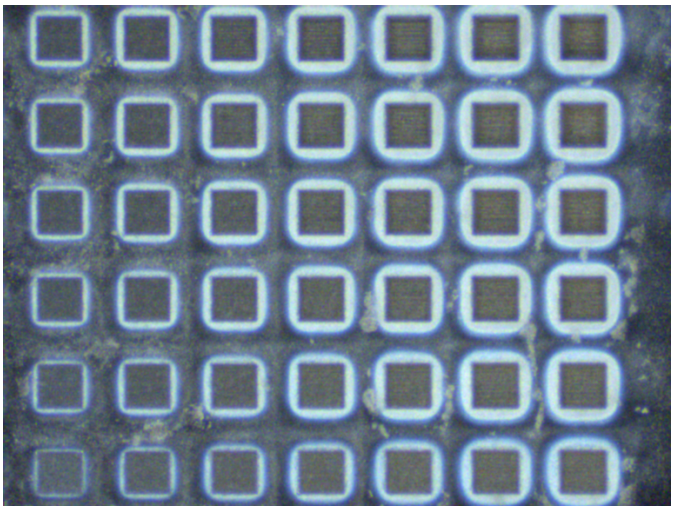

Figure E.1: Laser etched squares from left to right increasing laser power from 20-100% in steps of 10%. From bottom to top increasing repetitions, from 1 to 30 in steps of 5 repetitions.

By visually scanning the surface a starting point is chosen. In this case 15 repetitions is chosen with 50% power. The resulting depths are analysed using a white light interferometer. Four squares were analysed to determine the relations between the parameters. Firstly the influence of the laser power was determined, figures [E.2a, E.2c, E.2e]. The roughness of the etch is determined using arithmetic mean deviation, equation E.1. In figures [E.2b, E.2d, E.2f] one can see that the result is not deep enough and the surface quality has deviations of around 6 µm. One can clearly see the lines made by the laser.

$$\mathrm{Ra}_s = \frac{1}{n}\sum_{i=1}^{n} |z_i| \tag{E.1}$$

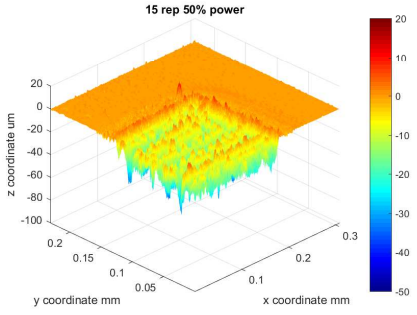

(a) Average depth:−12.33 µm, R_a:5.37 µm.

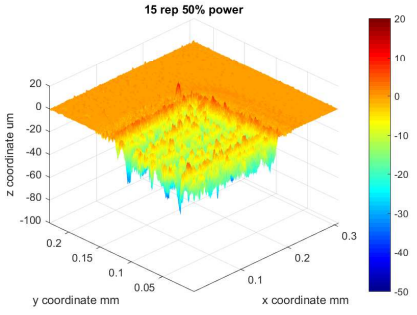

(b) Average depth:−12.33 µm, R_a:5.37 µm.

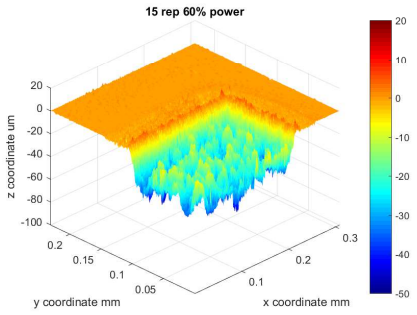

(c) Average depth:−23.88 µm, R_a:5.73 µm.

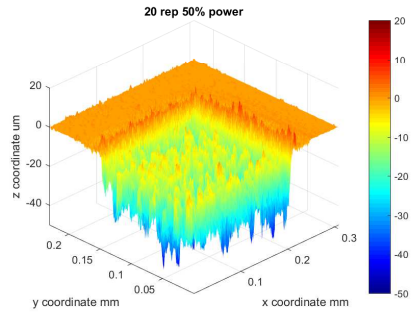

(d) Average depth:−17.34 µm, R_a:5.98 µm.

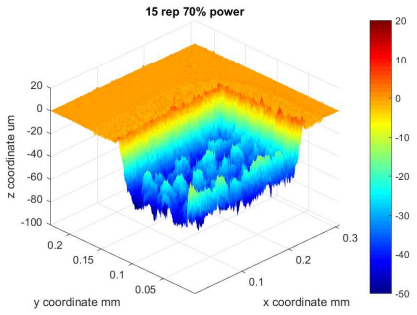

(e) Average depth:−36.16 µm, R_a:6.68 µm.

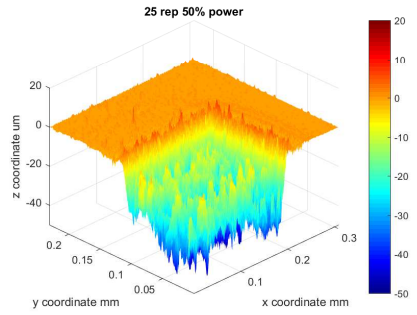

(f) Average depth:−22.69 µm, R_a:7.02 µm.

Figure E.2: White light interferometry images with varying repetitions and power. Figures [a,c,e] show the effect of increasing the power. Figures [b,d,f] show the effect of increasing the repetitions.

From the variation of repetition and the variation in power, we can see a relation between repetition, power and depth. Increasing the amount of repetitions increases the depth. Furthermore the roughness increases with more repetitions. Compared to the increase in power the increase in repetition has a higher increase in roughness relative to the increase in depth. The use of 100% power is therefore analysed. In figure E.2 one can see the clear lines created by the laser. There is material left between the laser paths which create ridges. To create a smooth surface the etching pattern must be closer together or in a different shape. First the effect of reducing the line spacing is examined.

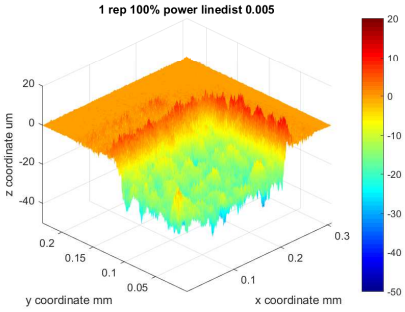

(a) Average depth: −15.68 µm, R_a:3.06 µm.

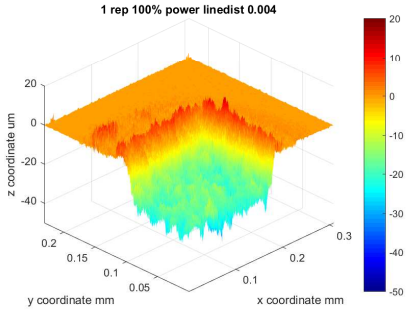

(b) Average depth:−18.61 µm, R_a:2.47 µm.

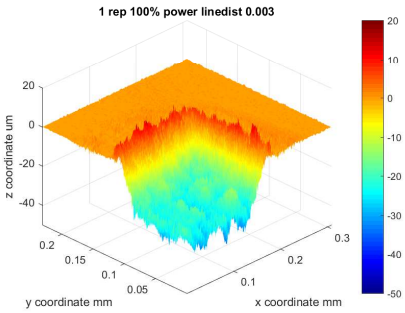

(c) Average depth: −22.58 µm, R_a:2.77 µm.

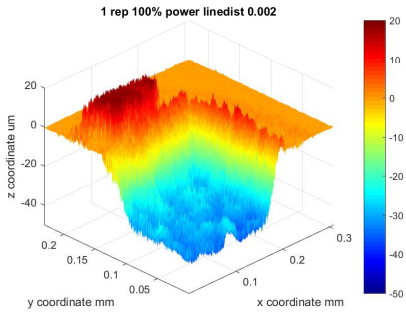

(d) Average depth: −30.11 µm, R_a:2.45 µm.

Figure E.3: White light interferometry image with varying line spacing.

The closer the lines, the better surface roughness however the depth is increased as well. The downside of having the lines closer together is that the machining time is greatly increased. In figure E.4 the resulting surfaces of different etching patterns is shown.

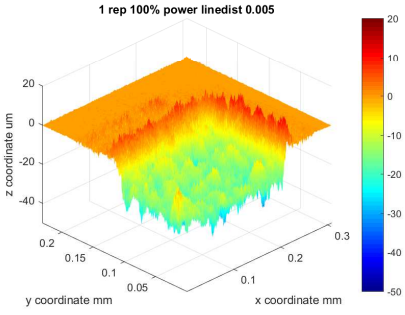

(a) Average depth: -15.68 µm, R_a:3.06 µm.

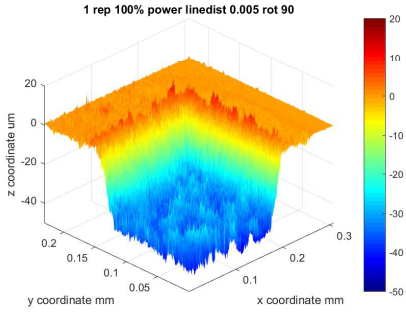

(b) Average depth:-33.98 µm, R_a:2.79 µm.

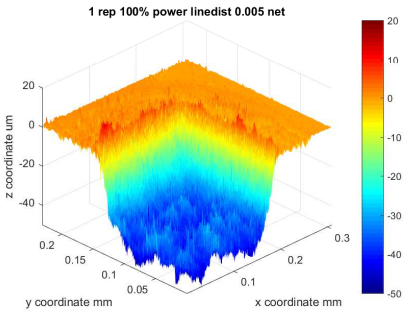

(c) Average depth: -38.08 µm, R_a:3.11 µm.

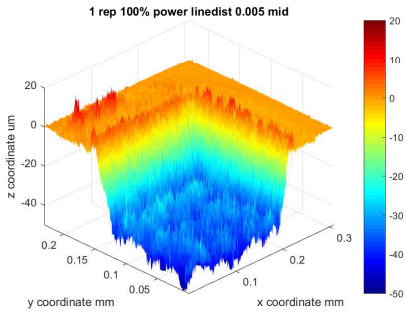

(d) Average depth: -36.00 µm, R_a:3.48 µm.

Figure E.4: white light interferometry image with varying etch patterns.

The net etch pattern provides a depth of 38 µm with low roughness. The extra depth is needed as during the bonding a small reduction of the depth is created. The net etch pattern is chosen for the manufacturing of the master. The line distance is set to 5 µm to create a reasonable machining time. The master design is etched into the silicon. The machining time is 7 hours and a half hour. The resulting master can be seen in figure E.5a. The master is cleaned using an ultrasonic cleaner, figure E.5b.

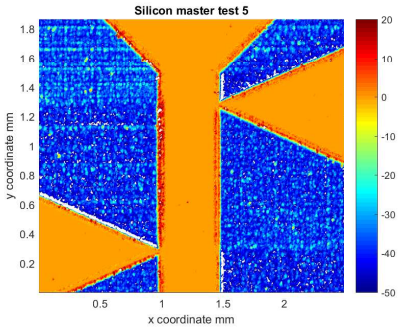

(a) White light interferometry image directly after laser etching.

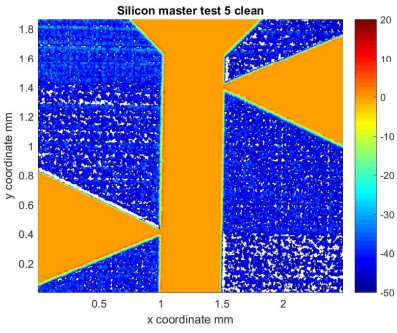

(b) White light interferometry ultra sonic cleaned.

Figure E.5: Effect of cleaning the master in the ultrasonic cleaner.

In figure E.5b one can see regions where the etching is not fully even. This is caused by the laser path planning. The etching pattern is therefore rotated 45° in the repetition to reduce the height difference caused by the laser path planning. The resulting master is shown in figure E.6.

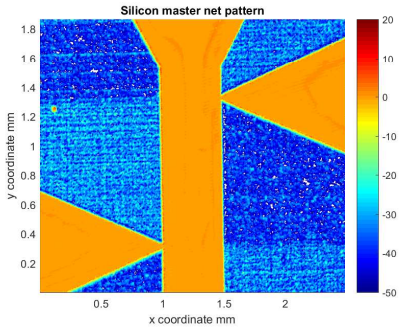

(a) Net pattern.

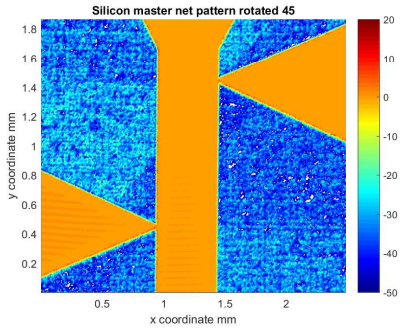

(b) Net pattern rotated 45° in the repetition.

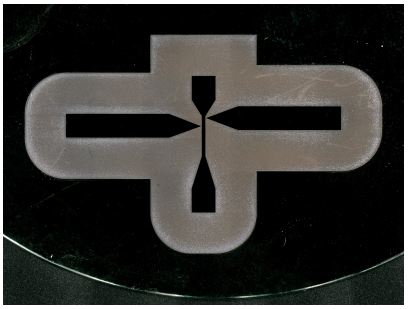

(c) Microscope image of a master with net pattern.

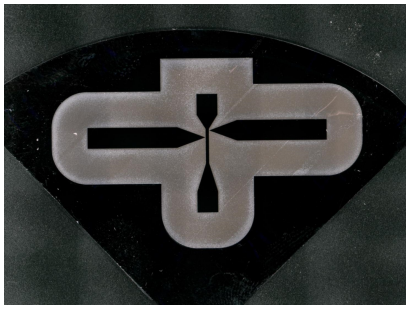

(d) Microscope image of the final master with net pattern rotated 45° in the repetition

Figure E.6: Final master.

E.1.2 Hot embossing

Hot embossing, material

After the production of the master, the master has to be pressed into a polymeric material. Firstly the polymeric material has to be chosen. The material needs to be cheap, as to keep manufacturing costs low. It must to be able to bond to other layers of the same material. It must be strong enough to retain the shape of the channel under pressure ranging to 10 bar. The material must have a large chemical compatibility. Preferably, the material has to be transparent, as to be able to visually check the fluid do not flow between layers. The following polymeric materials can be used:

- PolyCarbonate, (PC)
- PolyMethylMethAcrylate, (PMMA)
- CyclicOlefinCopolymer, (COC)
- PolyDiMethylSiloxane, (PDSM)
- PolyEtherEtherKetone, (PEEK)

- PolyOxyMethylene,(POM)

The material chosen is PMMA. PMMA is often used in hot embossing for microfluidic devices. PMMA is transparent and has high stiffness. The transparency will help assess the performance of the microchannel as well as indicate leakages. The PMMA used are cast sheets of 1 mm thickness. The sheets are laser cut into the designed shapes. PMMA has a low glass transition temperature making it easy to emboss. Lastly PMMA has a high chemical compatibility meaning many different types of fluid can be measured without damaging the system.

Hot embossing, press

To hot emboss the fabricated master into the PMMA a tool is needed. The tool required is in essence a heated mechanical press. There are commercial available hot embossers. These systems have high controllability in the applied force and the temperature control. An embossing tool is constructed as no commercial embossers are available within the department. The tool needs to be able to apply an evenly distributed pressure and heat the PMMA to the embossing temperature. To apply the pressure a simple bolt tightened press is made from cast steel and bolts. Two pieces of cast steel are used to further distribute the force. Two strips of aluminium are used to create a smooth support surface. An additional piece of silicon is used as a counter surface to keep a low surface roughness and thus transparency. The press assembly is put in an oven to heat the system. The pressure on the system is determined through bolt calculation, equation E.2.

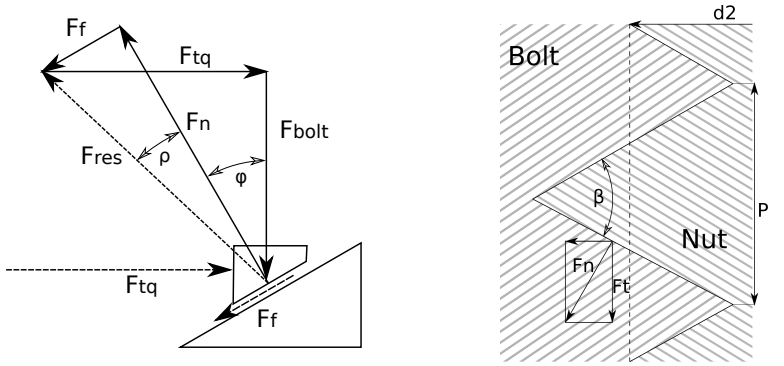

(a) Force balance bolt nut interaction.

(b) Side cut of a bolt and a nut.

Figure E.7: Forces acting in a single bolt.

$$M = d_2 * F_{\text{tq}} + F_{\text{bolt}} \mu_h \frac{d_h}{2} \tag{E.2}$$

$$F_{\text{tq}} = F_{\text{bolt}} * \frac{d_2}{2} \tan(\phi + \rho') \qquad F_{\text{bolt}} = \frac{\sigma A}{A_{\text{bolt}} n} \tag{E.3}$$

$$\rho' = \arctan\left(\frac{\mu}{\cos\left(\frac{\beta}{2}\right)}\right) \quad d_h = \frac{d_{\text{bolthead}} + d_{\text{hole}}}{4} \tag{E.4}$$

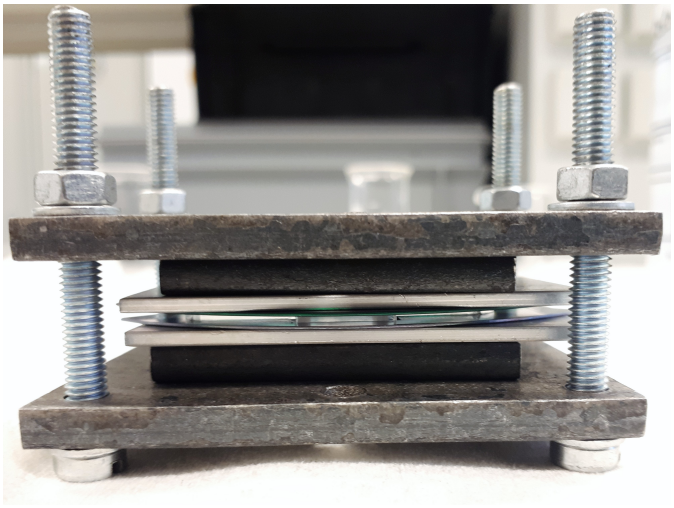

Figure E.8: Assembled press.

Hot embossing, process

The hot embossing process consist of four steps:

1 Heating of the assembly to the embossing temperature.

2 Embossing the PMMA through an applied pressure.

3 Cooling of the assembly to the de-embossing temperature.

4 De-embossing the PMMA.

These steps result in the temperature and pressure profile in figure E.10. The variables in this profile are: embossing temperature, applied pressure, embossing time and de-embossing temperature, pressing velocity, cooling and heating time. To hot emboss a design the material has to be heated to the embossing temperature. The embossing temperature is the area in the temperature reaction of the material where it is replacing its elastic behaviour for viscous behaviour. The material flows due to the pressure into the required shape, copying the master design. After the shape has been copied the temperature is reduced to the glass transition zone. In the glass transition zone the assembly is de-embossed as the behaviour of the PMMA is elastic. This gives the opportunity to release the master while maintaining the copied geometry. The temperature behaviour of PMMA can be characterised by figure E.9.

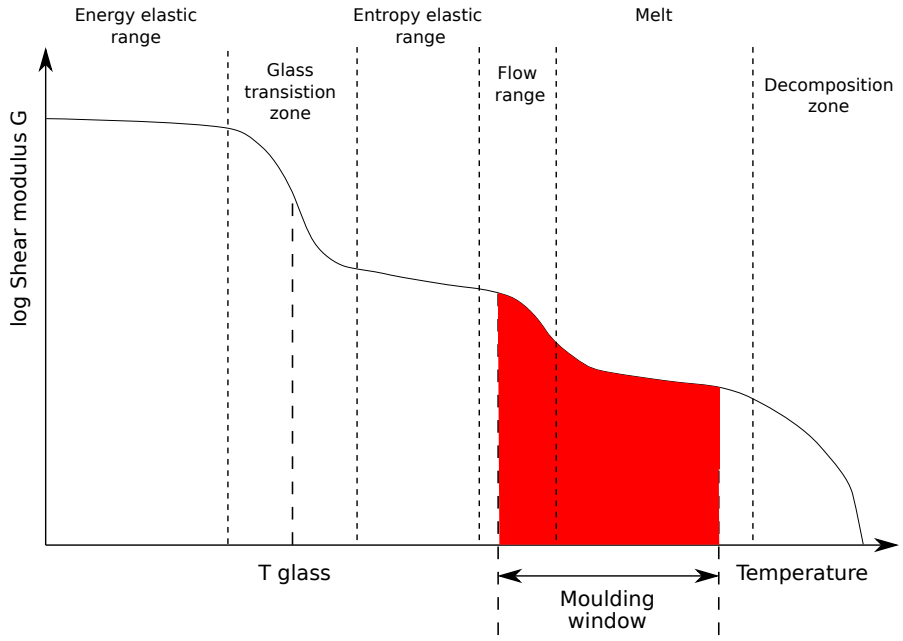

Figure E.9: Thermal moulding windows for hot embossing, [52].

The glass temperature of PMMA is between 80 °C to 110 °C. The initial values for the hot embossing process were taken form [31]. These were varied to obtain the optimal parameters for this application. The initial and final parameters are in table E.1. The lower pressure and temperature reduce the sticking effect. The full embossing protocol used can be found in appendix H.

	Temperature	Pressure	time
Initial	160 °C	1.2 MPa	20 min
Final	145 °C	0.8 MPa	20 min

Table E.1: Hot embossing parameters.

In figure E.10 the temperature and pressure profile used can be seen.

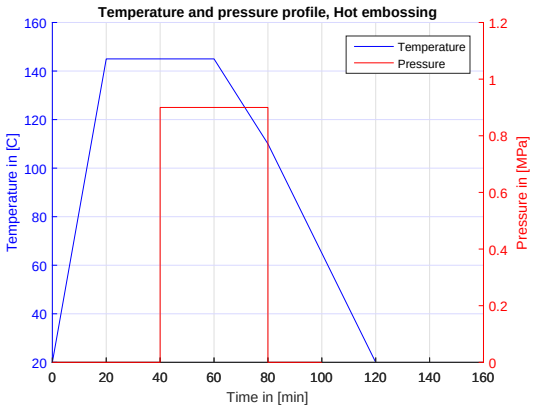

Figure E.10: Temperature in the oven and pressure on PMMA against time.

In the first attempts at embossing the channel an issue occurred with the de-embossing. Due to the rough surface of the laser etched areas the PMMA stuck to the silicon master. Removing the PMMA resulted in fracturing of the brittle silicon master. Furthermore, as the PMMA stuck to the silicon removing it from the oven caused the PMMA to shrink, bending the silicon master until it fractured, figure E.11.

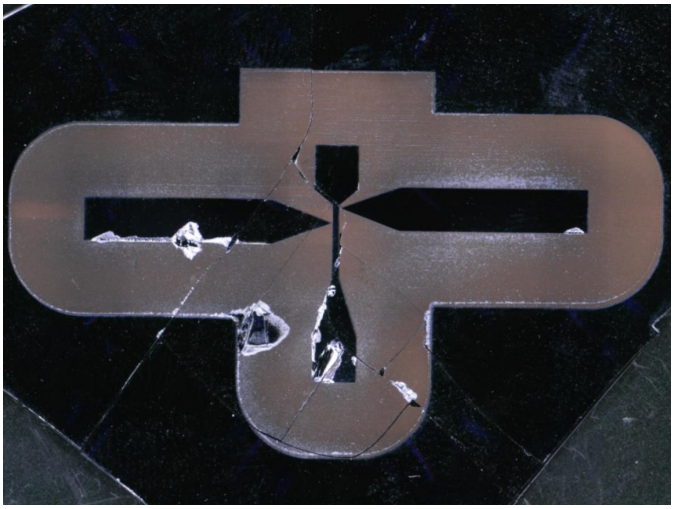

Figure E.11: Fractured master

There are different methods to resolve this issue. One is to prevent sticking, the other to let it release itself. An attempt is made to de-emboss using a chemical to make the PMMA slightly swell at the edges making it push off from the silicon and thus releasing itself. The chemical used is Propanol-2. When attempting this release technique the PMMA the silicon fractured. The de-embossing temperature is too high for the Isopropanol to have the desired effect. Remarkably, the area that was not affected by Isopropanol did not stick to the silicon. The result is unusable and Isopropanol will not be used to release the PMMA, figure E.12.

Figure E.12: Picture of PMMA being released with Isopropanol.

The second option is to spincoat the master with an anti stiction layer (ASL). This is a simple procedure. The anti stiction layer used is a Methyl nonafluorobutyl ether named EVGNIL ASL from EV Group GmbH . The anti stiction layer creates a monolayer on top of the silicon. Together with lower temperature and pressure, removal of the PMMA without breaking the silicon master is achieved. This process is repeated 4 times without any impact on the silicon master in figures [E.6a,E.6c].

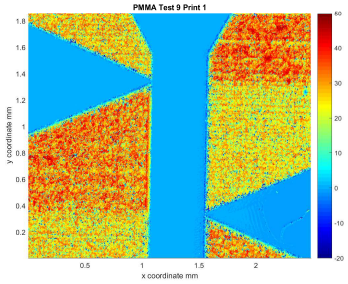

(a) White light image of embossed PMMA print 1.

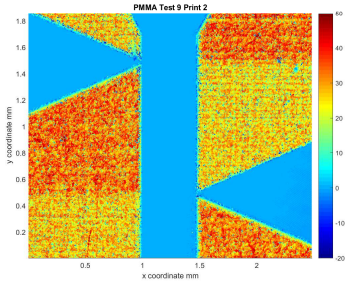

(b) White light image of embossed PMMA print 2.

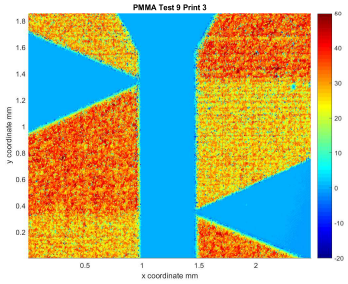

(c) White light image of embossed PMMA print 3.

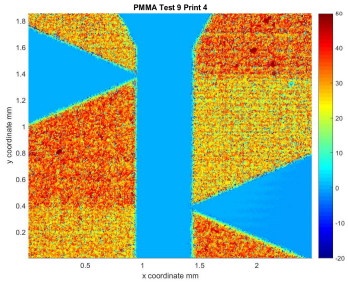

(d) White light image of embossed PMMA print 4.

Figure E.13: Four different prints of PMMA made with one silicon master.

Bonding

Bonding is required to seal the channel. Two binding techniques are commonly used, [53]. Thermal fusion bonding and adhesive bonding. Adhesive bonding uses a high viscosity adhesive which forms a bond after curing by UV light. The downside of this bonding technique is the addition of a layer of adhesive which increases the gap height. Film heights are in the range of 40 µm. This is already more than the gap height designed. Thermal fusion bonding uses the thermal properties of the substrate material. By heating the polymer to the glass transition zone the polymers become slightly mobile. By pressing the surfaces together interdiffusion of polymer chains creates a strong bond, possibly as strong as the bulk material. This process is first tested on the layers without any embossed structure. The bonding process is similar to the embossing step but requires a lower temperature to inhibit deformation of the geometry. The 4 layers are aligned and assembled in the press. For a smooth counter surface, silicon wafers are placed on either side. The press is tightened to 0.57 MPa and placed in an oven preheated to 110 °C. The assembly is left in the oven for 90 minutes and then slowly cooled to room temperature. The pressure is removed and the press is disassembled. The result can be seen in figure E.14.

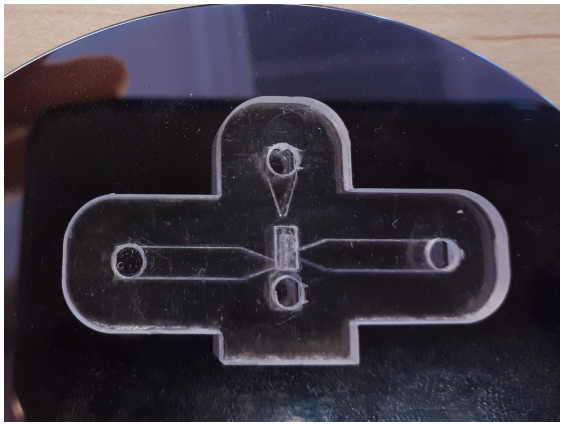

Figure E.14: Bonding test binding all layers together.

The result shows full bonding with transparent layers. The process is used to bond layers 2,3 and 4, figure D.18. The bonding with an embossed structure is more challenging as the surface is less smooth resulting in reduced contact between the layers. Furthermore the embossed channel must be preserved. The first test attempting to bond the layers with an embossed structure showed swelling in the channels causing them to be blocked as well as insufficient bonding, figure E.15.

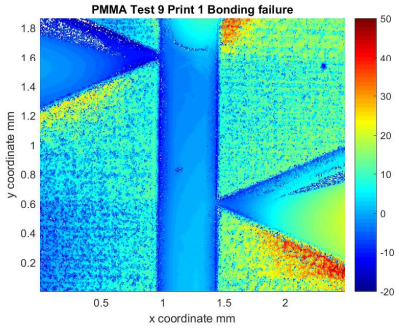

Figure E.15: Bonding failure.

The bonding parameters were adjusted and some successful bonding was achieved, however full sealing of the channel was problematic due to height differences in the embossed structure. These height differences were caused by the master. To resolve this issue an intermediate flattening stage was introduced and eventually the master laser pattern was adjusted, see section E.1.2.

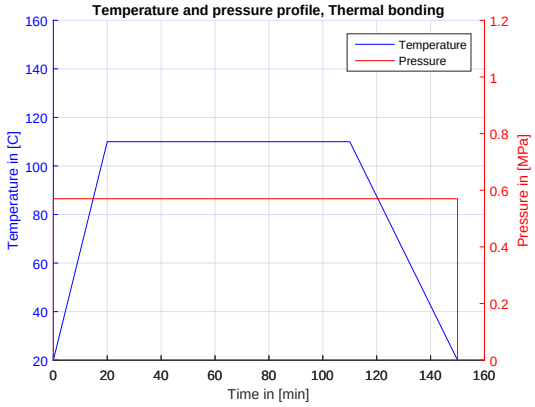

Figure E.16: Temperature in the oven and pressure on PMMA against time.

Flattening

The uneven surface on the PMMA, due to the laser etched surface, is subjected to flattening stages. As a result of these steps, the bonding is improved and a sealed channel is obtained. The embossed PMMA is put in between two layers of silicon and assembled in the press. By heating the assembly to around the glass temperature the peaks on the PMMA can be flattened to create a smooth bonding surface. Initially the flattening was done in multiple steps to find the correct parameters for this process.

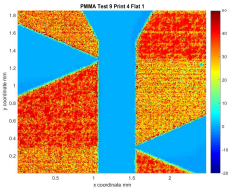

(a) Print 4 flattened 1 time.

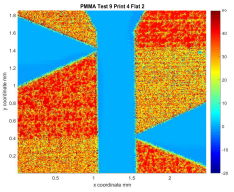

(b) Print 4 flattened 2 times.

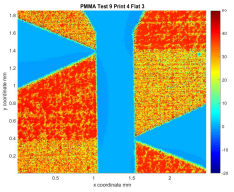

(c) Print 4 flattened 3 times.

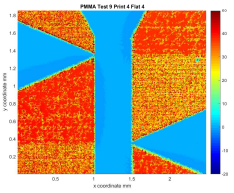

(d) Print 4 flattened 4 times.

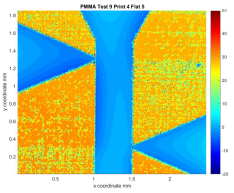

(e) Print 4 flattened 5 times

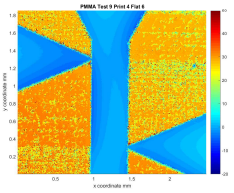

(f) Image print 4 flattened 6 times.

Figure E.17: Flattening progress.

From figure E.17 we can see the effect of the flattening stages. The peaks are attenuated. The downside of the flattening stage is the swelling of the channels. The channel is unsupported resulting in rising of the centre of the channel. Furthermore, due to the flattening the height of the channel is slightly reduced. The flattening stages were performed on the rotated master as well, figure E.18.

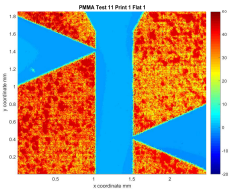

(a) Print 1 flattened 1 time.

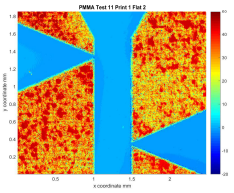

(b) Print 1 flattened 2 times.

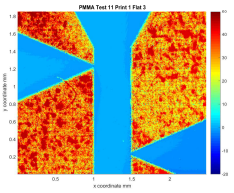

(c) Print 1 flattened 3 times.

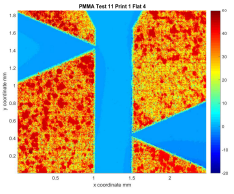

(d) Print 1 flattened 4 times.

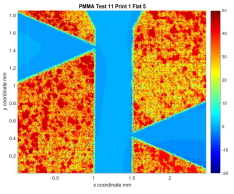

(e) Print 1 flattened 5 times

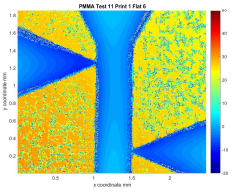

(f) Print 1 flattened 6 times

Figure E.18: Flattening progress test 11.

The final procedure uses a single flattening step at a temperature of 110 °C, pressure of 0.57 MPa for 55 min. By cooling the assembly faster after the flattening the thermal stress reduces the swelling of the channel. The final flattening stage is illustrated in figure E.19. The resulting flattened embossed PMMA has much better contact surface for bonding to the remaining PMMA layers.

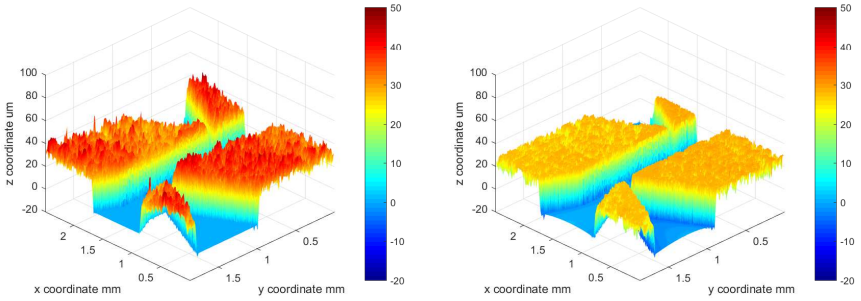

(a) before flattening.

(b) After flattening.

Figure E.19: White light interferometry images of PMMA surface before and after the final flattening process.

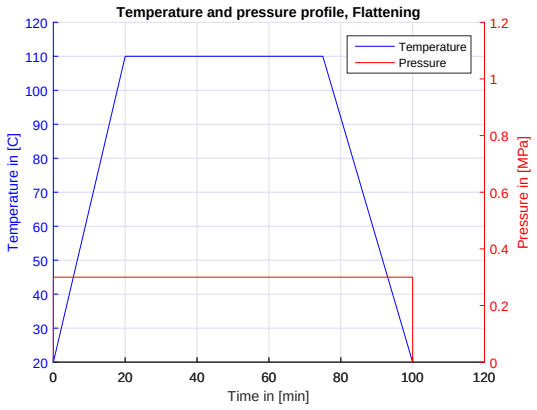

Figure E.20: Temperature in the oven and pressure on PMMA against time.

Bonding embossed

After the flattening stage, the bonding improved. However, due to the swelling of the channel and the heat in the bonding stage the channels would seal themselves. Resulting in a closed channel. The conclusion from this was that thermal bonding caused too much damage to the channel to be used as a bonding technique to bond to the other layers. Therefore, another technique is applied. Chemical enhanced bonding brings the advantage of bonding at lower temperatures and pressure, [32]. A chemical agent softens the bonding surfaces and while it evaporates from the surface activates the polymer chains at the surface to interdiffuse to the counter surface, creating a bond, [54]. The solvent used is 70 % Isopropanol. The solvent is distributed on top of the embossed PMMA. The remaining layers are placed on top. The assembly is pressed together and excess solution removed. While under slight pressure the layers are aligned. The press is hand tightened and placed in a preheated oven of 68 °C. The press is left for 15 minutes. The press is removed and slowly cooled to room temperature. Once cooled the pressure is removed. The temperature and pressure are sketched in figure E.21b. If the bond is incomplete the process can be repeated without damaging the channel geometry. The final assembled chip can be seen in figure E.21a.

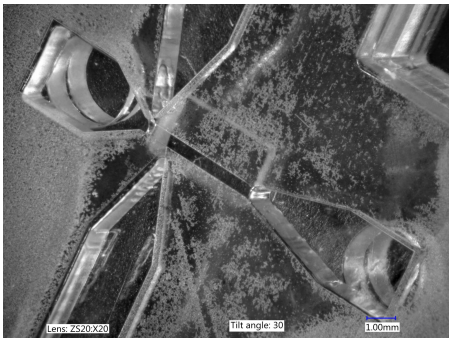

(a) The assembled chip.

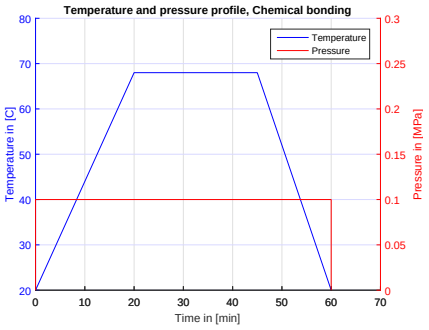

(b) Temperature in the oven and pressure on PMMA against time.

Figure E.21: Final bonded chip and the temperature and pressure profile of chemical bonding.

E.1.3 Preliminary test

After all the layers have been bonded, the chip is tested for leakages before the connectors are attached. If a leakage is present, the chemical bonding can be repeated or the leakage can be sealed. To determine the location of potential leakages, the chip is submerged and air pumped into the entrance channel to show the escaping air, figure E.22a.

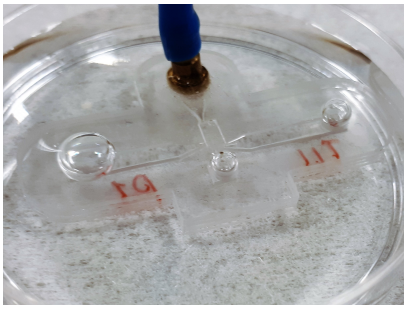

(a) Preliminary air test, showing leakages.

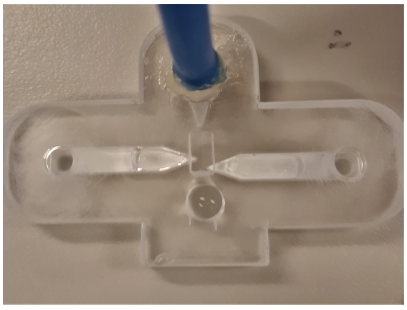

(b) Preliminary water test, showing blockages.

After the air test a water test is performed to check flow is possible through all the channels. If the channel is blocked the pressure can not be measured. The flow can be seen by the meniscus moving through the channel, figure E.22b.

E.1.4 Final assembly

The final step is to glue in place the connectors for the tubing. The connectors are made from Festo piping and adjusted to fit the into the chip. The glue used is Bison plastic combi epoxy. The final chip with connectors is presented in figure E.23.

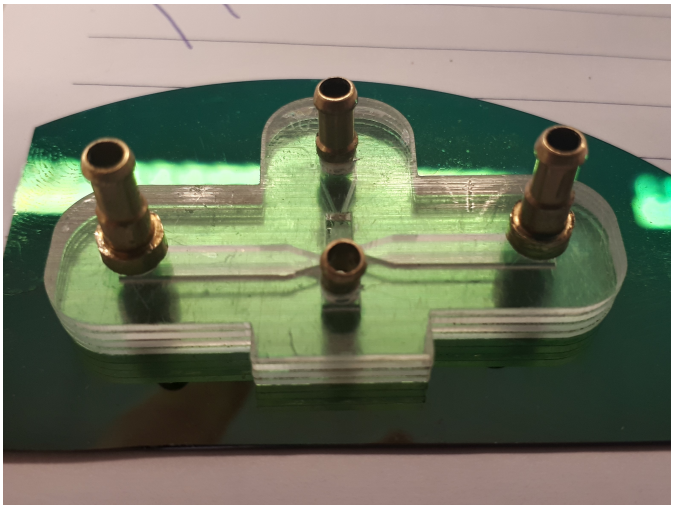

Figure E.23: Completed chip.

E.2 Core manufacturing

To facilitate the manufacturing of the core a layered design is chosen. This means only laser cutting is required to get the complex shape of the core. Furthermore the layered design reduces eddy currents in case a alternating field is applied. The round shape is approximated by layers of 2 mm. The layer thickness has been chosen to easily fill the pole. The resulting core design can be seen in figure E.24a. The core is separated into a top half and a bottom half. This is to give the possibility to place the measuring chip as well as to measure electrorheological fluids by simply attaching the electrodes to the separated core halves. The bobbin is 3D printed and wined with magnetic copper wire. A picture of the resulting coils can be seen in figure E.24b.

(a) Magnetic core.

(b) Magnetic core with coil.

Figure E.24: Magnetic core design

The laser cutting results in low edge quality. Therefore, the excess material has been filed off. The contacting parts of the top and bottom half have been milled down together with the central tip to ensure an accurate gap between the core halves and to create a flush contact. The manufactured core can be seen in figure E.25.

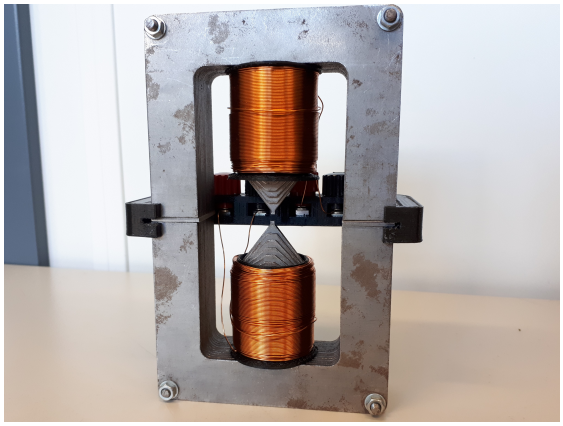

Figure E.25: Fabricated magnetic core

E.2.1 Preliminary test

The magnetic core has been tested for its performance. The magnetic field density was measured for different actuation currents on the coils. The coils received the same actuation current which was measured with multimeters. The power is provided by a Voltcraft power supply in current source mode. The results are shown in figure E.26.

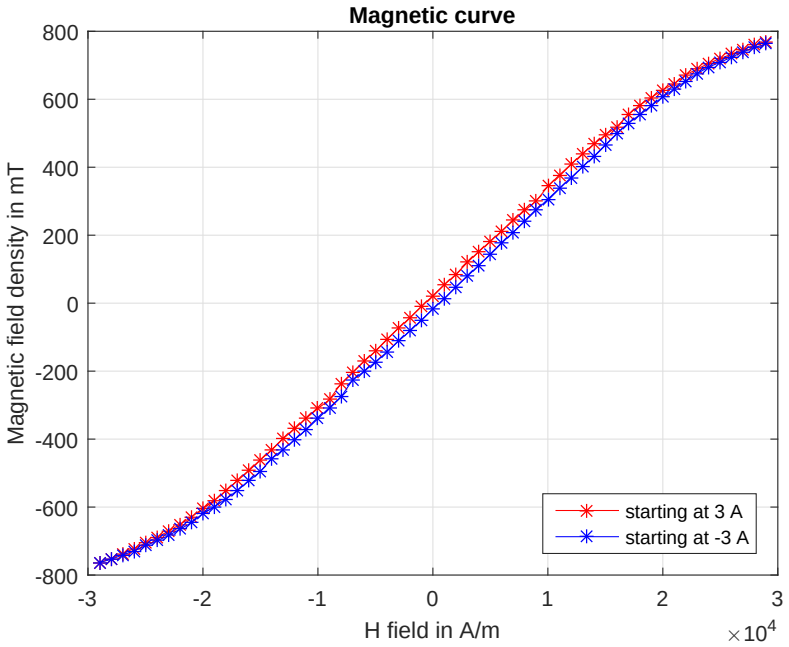

Figure E.26: Magnetic curve of the magnetic core.

In the figure we can see that the material saturates around the 1 T. Furthermore we see a small coercivity of less than 690 $A\,m^{-1}$. The remanence of the steel is around 22 mT. Due to the low saturation more power is required to reach the high fields which means more heat is developed in the system. Therefore it is not possible to run the magnetic system for prolonged periods of time at maximum field density. The resulting permeability is 31.8 $mH\,m^{-1}$. The relative permeability is 25300. In the measurements the core starts in a demagnetized state and will only use limited currents as the tested fluid magnetic saturation is around 50 mT. Therefore the core is measured for the measurement states used in the fluid measurements, table E.2.

Current	B-field	Current	B-field
0	9	0.4	109
0.1	34	0.3	85
0.2	57	0.2	59
0.3	83	0.1	35
0.4	109	0	9

Table E.2: Magnetic field for fluid measurements.

E.3 External systems

Next to the chip and the core, two more systems are needed. A flow actuation system is required as well as a data acquisition system. These systems are chosen for the requirements of the designed prototype.

E.3.1 Actuation

The actuation needs to provide constant fluid flow of $10\,\mu L\,min^{-1}$ to $5\,mL\,min^{-1}$. A commonly used device for these applications is a syringe pump. These pumps provide a pulsation free flow which can be programmed. The pump uses a syringe filled with the to be measured fluid which is pressed by the linear stage. The pump used is a Kd Scientific Legato 111 double syringe programmable infusion and withdrawal pump. The specification of the syringe pump can be found in table E.27.

Syringes	0.5 µL - 10 mL
Max force	133 N at max force selection
Min travel rate	$0.15\,\mu m\,min^{-1}$
Max travel rate	$159\,mm\,min^{-1}$
Min flow rate	$1.26\,pL\,min^{-1}$ (0.5 µL syringe)
Max flow rate	$25.99\,mL\,min^{-1}$ (10 mL syringe)

Figure E.27: KDS Scientific syringe pump specifications

The syringe used with the pump is a 10 mL Terumo syringe. With this syringe a long measuring time can be acquired and the required flow rates to reach the ultra high shear rates. The maximum pressure applied by the pump with the syringe is 6.7 bar, equation E.5.

$$P_{max} = \frac{F_{max}}{\pi R^2_{plunger}} \tag{E.5}$$

For future applications using higher viscosity fluids a stronger syringe pump and syringes will be required. Stainless steel syringes are available as well as syringe pumps which provide pressures up to 240 MPa, figure E.28.

(a) Mid Pressure Syringe Pump neMESYS 1000N

(b) Stainless steel syringes

Figure E.28: Potential actuation system

E.3.2 Data acquisition system

As the syringe pump has been chosen, the sensors can be determined. The sensors are required to measure the pressure at two points. The maximum pressures each sensor has to measure can be derived from the maximum pressure at the entrance, figure E.29. The maximum pressure the syringe pump can deliver is 7 bar. The resulting pressures at the sensor locations give the maximum required limits of the sensors. The limits are:2 bar and 300 mbar.

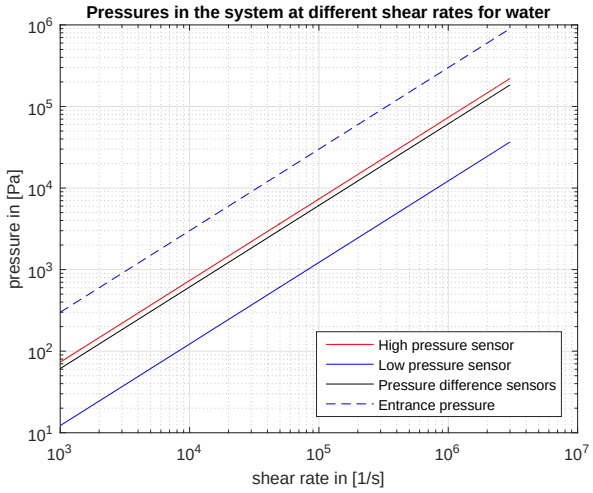

Figure E.29: Pressure development for the designed prototype at different shear rates for water.

Two sensors have been selected with the maximum pressure limit required. The sensors use a current output to limit the interference of the magnetic field on the measurement. The sensors are RS PRO gauge pressure sensors, figure E.30. The accuracy of the sensors determines the minimum pressure measurable. The accuracy of the sensors is $< \pm 0.25\,\%$ of the full scale range.

(a) High pressure sensor.

(b) Low pressure sensor.

Figure E.30: RS Pro sensors.

The sensors are connected to a National Instruments DataQ system and records every 400 ms. The

data is stored on a PC together with the time stamp. The event data, flow rates and current, are manually logged with the time stamp of the events.

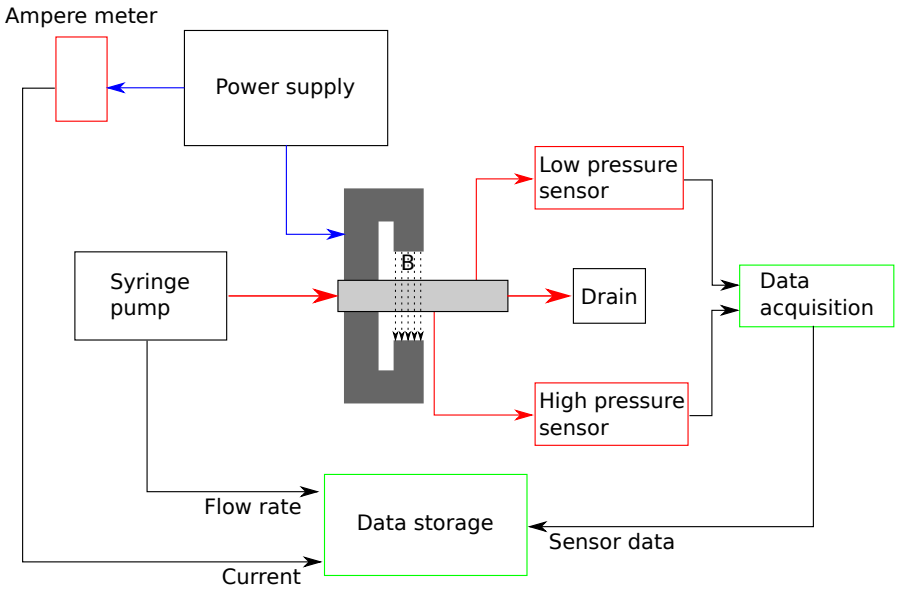

Figure E.31: Data collection scheme.

E.4 Data processing

Firstly a calibration file is made. 200 data points are taken without ant flow or magnetic field. The calibration file is needed to determine the base state of the system. After the calibration file the measurement is started. First 100 data points are taken without any flow or field. Then the syringe pump is turned on. The measured pressures climb to a steady state. Once the steady state is stable the time stamp is logged in the event file. Then the field or flow rate are changed and the process is repeated. The logged data of a measurement can be seen in figure E.32.

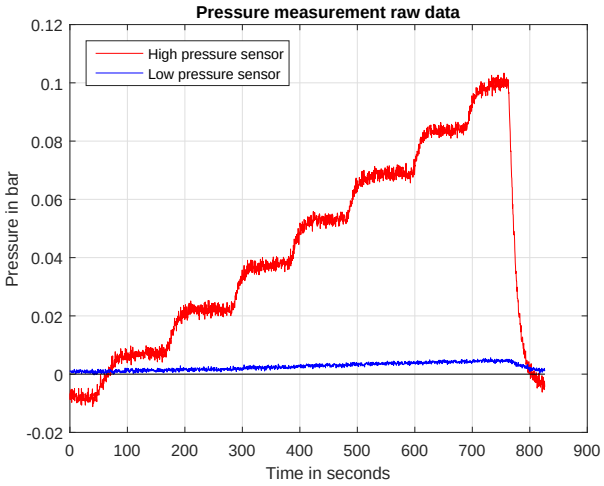

Sample #	Flow rate
0	$0\,\mu L\,min^{-1}$
100	$100\,\mu L\,min^{-1}$
400	$200\,\mu L\,min^{-1}$
700	$300\,\mu L\,min^{-1}$
950	$400\,\mu L\,min^{-1}$
1200	$500\,\mu L\,min^{-1}$
1500	$600\,\mu L\,min^{-1}$
1720	$700\,\mu L\,min^{-1}$
1900	$0\,\mu L\,min^{-1}$

Figure E.32: Typical measurement with event data

The data is firstly zeroed. The first 100 data points of the measurement are taken of the high pressure sensor and low pressure sensor as the zero pressures. The offset is added to all data points in the measurement. The data is selected which represent the measurement points. These are selected as the last 100 data points before the next event logged. The zeroed and selected data of the measurement is presented in figure E.33.

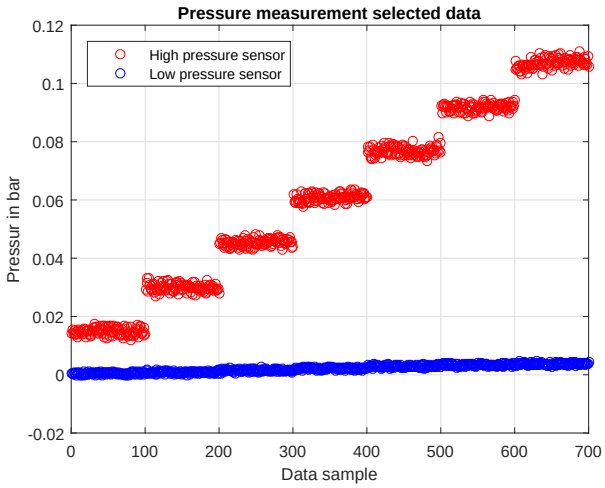

Figure E.33: Selected data.

The data points of each event are averaged and converted into shear stress using equations D.1. The shear rates are calculated form the flow rates using equation D.15. The shear stress and shear rate couples are used to calculate the apparent viscosity using equation A.1.

Appendix F

Results

To determine the performance of the rheometer the viscosity was measured of 3 different fluids: deionized water, Shell Tellus S2 VX15 hydraulic oil and Ferrotech EFH1. For comparison, the same fluids were measured in a commercial rheometer, Anton Paar MCR 302 with a magnetic insert to measure MR fluids, F.1. The shear rates on the Anton Paar are limited to 10^4 s^{-1}.

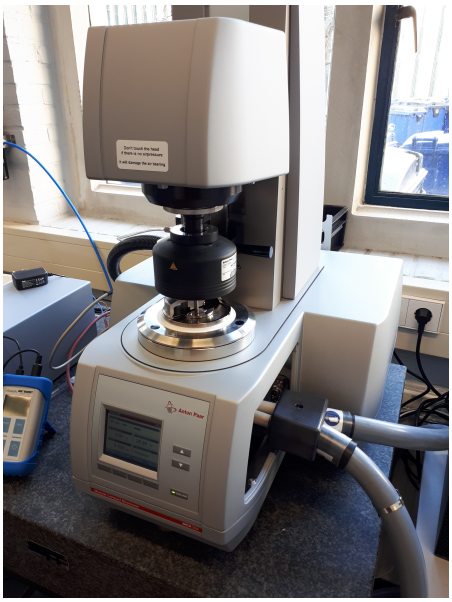

Figure F.1: Anton Paar MCR 302 with magnetic insert.

The plots of each fluid can be found in figure F.3 F.4 and F.6 for deionized water, Shell Tellus VX15 and EFH1 respectively.

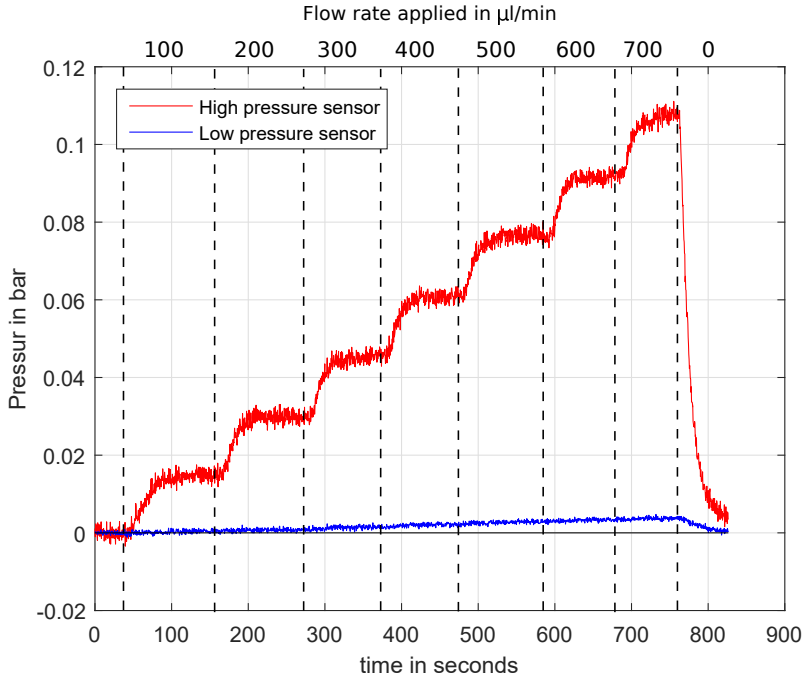

Figure F.2: Typical measurement of pressure against time at different flow rates.

Figure F.2 shows a typical measurement. The measurement is started in a steady state with zero flow. After 100 samples the measurement is started. These sample points are used as zero measurement for the sensors. A flow rate is applied. Once the measured pressure has reached a steady state the flow rate is increased. This process is repeated until the syringe is empty. As the flow is stopped the pressures quickly return to their zero value. 4 chips have been successfully produced and tested. The chip parameters are listed in table F.1.

Chip	Height	Exit length
T9P5	25.8 µm	0.04 mm
T13P1	30.1 µm	0.015 mm
T13P3	29.7 µm	0.2 mm
T14P1	33.5 µm	0.33 mm

Table F.1: Measured chip parameters.

The measured pressures and flow rates are converted into shear stresses and shear rates through the geometrical model, equation [3.5,3.6], respectively. The resulting data is plotted for the measured fluids, figures [F.3,F.4,F.6]

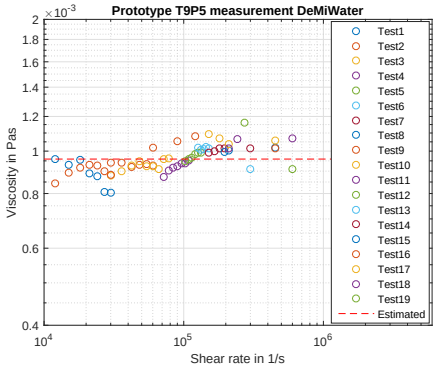

(a) Viscosity of demineralized water at different shear rates.

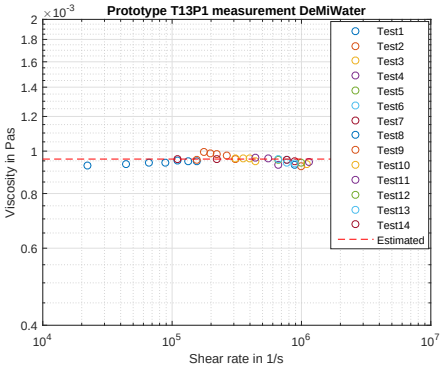

(b) Viscosity of demineralized water at different shear rates.

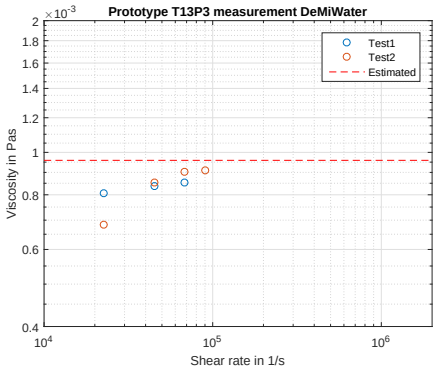

(c) Viscosity of demineralized water at different shear rates.

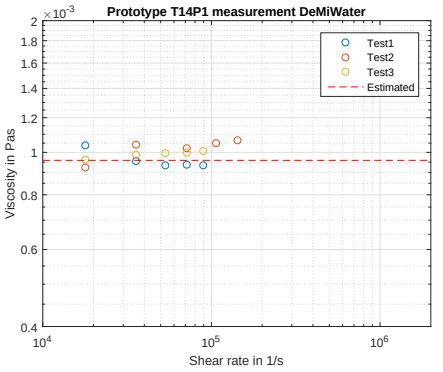

(d) Viscosity of demineralized water at different shear rates.

Figure F.3: Viscosity of deionized water for each tested chip.

The resulting viscosities at different shear rates are compared to the viscosity of water at 21.8 °C, 0.96 mPa s,[33]. The maximum shear rate measured was $1.16 \times 10^6\,s^{-1}$. Higher shear rates were not measured as the pump engine stalled.
The chip was cleaned and filled with Shell Tellus S2 VX15. The resulting viscosities can be seen in figure F.4.The expected viscosity is taken from the data sheet provided by Shell. The viscosity expected is 23 mPa s. The measurements from the Anton Paar rheometer have been added.

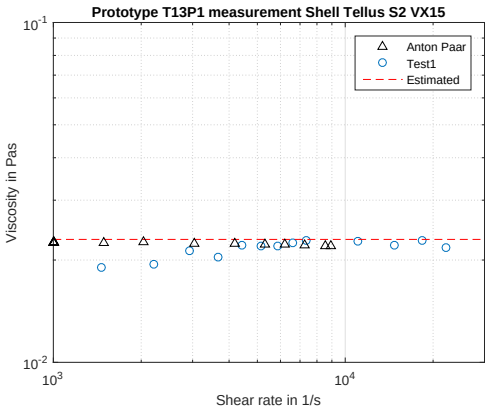

Figure F.4: Viscosity of Shell Tellus S2 VX15 at different shear rates.

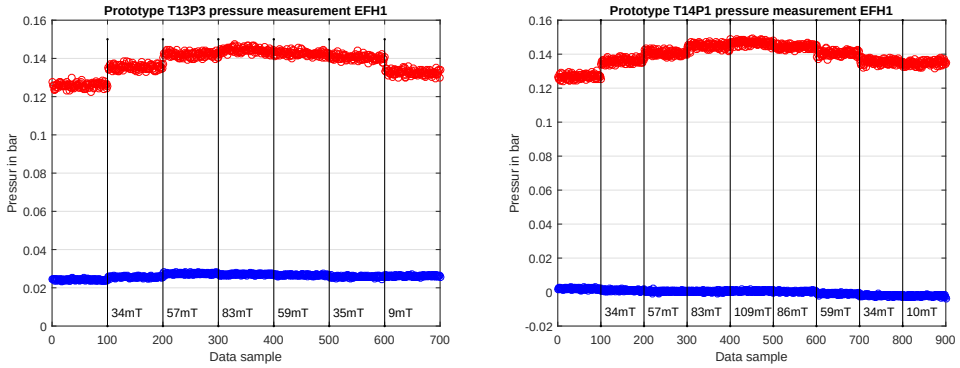

(a) Pressure measurement T13P3 for EFH1 at different magnetic fields and $100\,\mu L\,min^{-1}$.

(b) Pressure measurement T14P1 for EFH1 at different magnetic fields and $100\,\mu L\,min^{-1}$.

Figure F.5: Pressures measured for EFH1 in each tested chip.

Lastly, Ferrotec EFH1 has been measured to show the magnetorheological effect. The measurement was performed at a constant flow rate. Firstly, the flow is stabilised without magnetic field. Once this steady state is reached the magnetic field is applied. The current is increased in steps of 0.1 A to a maximum current of 0.4 A. The current is then reduced in the same steps. In figure F.5 the measured pressures are displayed. The pressures measured show a clear increase with increasing magnetic field. The calculated viscosities can be seen in figures [F.6a, F.6b].

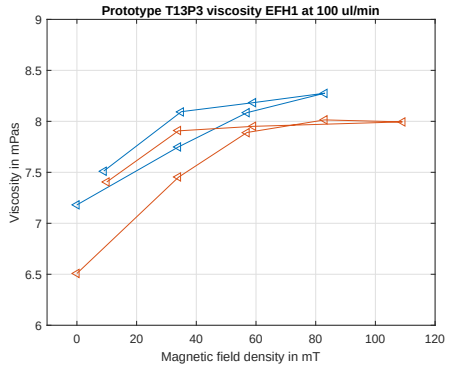

(a) Viscosity of EFH1 at different magnetic fields.

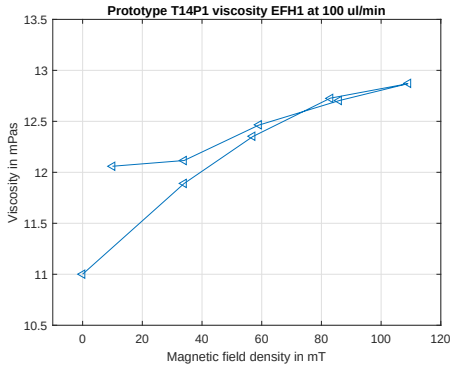

(b) Viscosity of EFH1 at different magnetic fields.

Figure F.6: Viscosity of EFH1 at different magnetic fields.

Appendix G

Navier Stokes equations

Navier Stokes Equation for incompressible fluids in Cartesian coordinates.

$$\rho \begin{bmatrix} \frac{\partial u_x}{\partial t} \\ \frac{\partial u_y}{\partial t} \\ \frac{\partial u_z}{\partial t} \end{bmatrix} + \rho \begin{bmatrix} u_x \frac{\partial u_x}{\partial x} + u_y \frac{\partial u_x}{\partial y} + u_z \frac{\partial u_x}{\partial z} \\ u_x \frac{\partial u_y}{\partial x} + u_y \frac{\partial u_y}{\partial y} + u_z \frac{\partial u_y}{\partial z} \\ u_x \frac{\partial u_z}{\partial x} + u_y \frac{\partial u_z}{\partial y} + u_z \frac{\partial u_z}{\partial z} \end{bmatrix} = \begin{bmatrix} \frac{\partial p}{\partial x} \\ \frac{\partial p}{\partial y} \\ \frac{\partial p}{\partial z} \end{bmatrix} + \eta \begin{bmatrix} \frac{\partial^2 u_x}{\partial x^2} + \frac{\partial^2 u_x}{\partial y^2} + \frac{\partial^2 u_x}{\partial z^2} \\ \frac{\partial^2 u_y}{\partial x^2} + \frac{\partial^2 u_y}{\partial y^2} + \frac{\partial^2 u_y}{\partial z^2} \\ \frac{\partial^2 u_z}{\partial x^2} + \frac{\partial^2 u_z}{\partial y^2} + \frac{\partial^2 u_z}{\partial z^2} \end{bmatrix} + \begin{bmatrix} f_x \\ f_y \\ f_z \end{bmatrix} \tag{G.1}$$

$$\frac{\partial u_x}{\partial x} + \frac{\partial u_y}{\partial y} + \frac{\partial u_z}{\partial z} = 0$$

Appendix H

Protocol

H.1 Embossing protocol.

1. Rinse with Isopropanol the surfaces in that are being pressed to make sure the surfaces are clean and can be in full contact with each other.
2. Rinse with deminiralerised water to remove the Isopropanol.
3. Dry the components.
4. Assemble the press layer by layer.
   (a) Align the PMMA with the silicon master.
   (b) Cover with polished silicon to create flat countersurface.
   (c) Cover with final press layer.
   (d) Manually press layers together while screwing on nuts.
   (e) Hand tighten nuts.
5. Place press in preheated oven.
6. When the components have heated to 140°C tighten bolts to the required torque.
7. Leave for 20 min.
8. Slowly cool to 110°C in the oven.
9. Release press.
10. Flip the device such that the master is on top.
11. Remove bolts.
12. Use a sharp tool such as scalpel to free the PMMA from the master.
13. Cool to room temperature in the oven.

H.2 Thermal bonding protocol

1. Rinse with Isopropanol the surfaces in that are being pressed to make sure the surfaces are clean and can be in full contact with each other.
2. Rinse with deminiralerised water to remove the Isopropanol.
3. Dry the components.
4. Assemble the press layer by layer.
   (a) Place silicon underlayer for a flat surface.
   (b) Align the PMMA layers with alignment tools.
   (c) Cover with polished silicon to create flat counter surface.
   (d) Cover with final press layer.
   (e) Manually press layers together while screwing on nuts.
   (f) Hand tighten nuts.
5. Tighten nuts to required torque
6. Place press in preheated oven.
7. Leave for 1.5 hour.
8. Slowly cool to room temperature in the oven.
9. Release press.

H.3 Chemical bonding protocol

1. Rinse with Isopropanol the surfaces in that are being pressed to make sure the surfaces are clean and can be in full contact with each other.
2. Rinse with deminiralerised water to remove the Isopropanol.
3. Dry the components.
4. Prepare the 70% Isopropanol solution.
5. Assemble the press layer by layer and inject the 70% Isopropanol solution.
   (a) Place silicon underlayer for a flat surface.
   (b) Placc the embossed PMMA layer on the silicon layer.
   (c) Apply thin layer of 70% Isopropanol solution.
   (d) Remove excess 70% Isopropanol solution.
   (e) Place the pre-bonded PMMA layers on top of the embossed PMMA layer.
   (f) Align the PMMA layers with alignment tools.
   (g) Cover with polished silicon to create flat counter surface.

(h) Cover with final press layer.

(i) Manually press layers together while screwing on nuts.

(j) Hand tighten nuts.

6. Tighten nuts to required torque
7. Place press in preheated oven.
8. Leave for 15 minutes.
9. Slowly cool to room temperature in the oven.
10. Release press.

Appendix I

References

[1] Xiaojie Wang and Faramarz Gordaninejad. Study of magnetorheological fluids at high shear rates. *Rheologica Acta*, 45(6):899–908, 2006.

[2] Deepak Baranwal and T S Deshmukh. MR-Fluid Technology and Its Application - A Review. *International Journal of Emerging Technology and Advanced Engineering*, 2(12):563–569, 2012.

[3] J. Rabinow. The magnetic clutch. *AIEE Trans.*, 67:1308–1315, 1948.

[4] R. Jacob. Magnetic fluid torque and force transmitting device, november 1951. US Patent 2,575,360.

[5] J Wang and G Meng. Magnetorheological fluid devices: principles, characteristics and applications in mechanical engineering. *Proceedings of the Institution of Mechanical Engineers, Part L: Journal of Materials: Design and Applications*, 215(3):165–174, 2005.

[6] J.D. Carlson and M.J. Chrzan. Magnetorheological fluid dampers, January 1994. US Patent 5,277,281.

[7] Juan de Vicente. Magnetorheology : a review. *Rheo-Iba*, 1:1–18, 2013.

[8] J. Huang, J. Q. Zhang, Y. Yang, and Y. Q. Wei. Analysis and design of a cylindrical magnetorheological fluid brake. *Journal of Materials Processing Technology*, 129(1-3):559–562, 2002.

[9] Stefan Georges Emile Lampaert. Planar Ferrofluid Bearings Modelling and Design Principles. Master's thesis, Technical University Delft, 2015.

[10] Dimitrios A. Bompos. *Tribological Design of Nano / Magnetorheological Fluid Journal Bearings*. PhD thesis, University of Patras, 2015.

[11] Anton Paar. *Application specific accessories for additional parameter setting*, 2016.

[12] TA Instruments. *Discovery Hybrid Rheometers Temperature Systems and Accessories*, 2014.

[13] F.D. Goncalves. *Characterizing the Behavior of Magnetorheological Fluids at High Velocities and High Shear Rates*. PhD thesis, Virginia Polytechnic Institute and State University in, January 2005.

[14] Ac Becnel, W Hu, and Nm Wereley. Measurement of magnetorheological fluid properties at shear rates of up to 25000 s-1. *Magnetics, IEEE Transactions*, 48(44):3525–3528, 2012.

[15] ACA systems OY. *ACAV runnability analyzers for coating colors and pigment slurries*. ACA systems OY, Outilantie 3 FIN-83750 Sotkuma Finland.

[16] RheoSense. *hts-VROC Viscometer, high temperature high shear viscosity*. RheoSense.

[17] TannasCo. *TBS 2100E-F, HTHS Tapered Bearing Simulator Viscometer*. Tannas Co.

[18] PCS Instruments. *Ultra Shear Viscometer*. PCS Instruments, 78 Stanley Gardens, London W3 7SZ UK.

[19] C F Dewey. Secondary flow and turbulence in a cone-and-plate device. *Journal of Fluid Mechanics*, 138:379–404, 1984.

[20] R. W. Connelly and J. Greener. High Shear Viscometry with a Rotational Parallel Disk Device. *Journal of Rheology*, 29(2):209–226, 1985.

[21] Keizo Watanabe, Shu Sumio, and Satoshi Ogata. Formation of Taylor Vortex Flow of Polymer Solutions. *Journal of Fluids Engineering*, 128(1):95, 2006.

[22] Frank M. White. *Fluid Mechanics*. McGraw-Hill, 7th edition edition, 2011.

[23] B. X. Wang and G. P. Peterson. Frictional flow characteristics of water flowing through rectangular microchannels. *Experimental Heat Transfer*, 7(4):249–264, 1994.

[24] N T Obot. Toward a Better Understanding of Friction and Heat / Mass Transfer in Microchannels a Literature Review. *Technology*, 3954:155–173, 2002.

[25] Dilhan M. Kalyon. Apparent slip and viscoplasticity of concentrated suspensions. *Journal of Rheology*, 49(3):621–640, 2005.

[26] Faith A. Morrison. *Understanding Rheology*. Oxford University Press, 2001.

[27] Christopher W. Macosko. *Rheology, Principles Measurements and Applications*. John Wiley & Sons, 1994.

[28] A. Costa, O. Melnik, and E. Vedeneeva. Thermal effects during magma ascent in conduits. *Journal of Geophysical Research: Solid Earth*, 112(12):1–16, 2007.

[29] R. Y. Chen. Flow in the Entrance Region at Low Reynolds Numbers. *ASME J. Fluids Eng.*, 1(95):153–158, 1973.

[30] Boran Jia. Evaluation of fast prototyping method of laser micromachining by thermal damage. Thesis, Delft University of Technology, september 2017.

[31] Alireza Shamsi, Ali Amiri, Payam Heydari, Hasan Hajghasem, Mansour Mohtashamifar, and Mehrnaz Esfandiari. Low cost method for hot embossing of microstructures on PMMA by SU-8 masters. *Microsystem Technologies*, 20(10-11):1925–1931, 2014.

[32] Arshya Bamshad, Alireza Nikfarjam, and Hossein Khaleghi. A new simple and fast thermally-solvent assisted method to bond PMMA to PMMA in micro-fluidics devices. *Journal of Micromechanics and Microengineering*, 26(6):065017, 2016.

[33] Viscosity of water. https://wiki.anton-paar.com/en/water/, 3 2018.

[34] Zenamarkos B. Sendekie and Patrice Bacchin. Colloidal Jamming Dynamics in Microchannel Bottlenecks. *Langmuir*, 32(6):1478–1488, 2016.

[35] J. O. Ojediran and A. O. Raji. Thin layer drying of millet and effect of temperature on drying characteristics. *International Food Research Journal*, 17(4):1095–1106, 2010.

[36] Jurgen Wilke, Holger Kryk, Jutta Hartmann, and Dieter Wagner. *Theory and Praxis of Capillary Viscometry - An Introduction*.

[37] Anton Paar. Stabinger viscometer. http://www.anton-paar.com/?eID=documentsDownload&document=1039&L=8, 1 2017.

[38] Chanyut Kolitawong and A. Jeffrey Giacomin. Dynamic response of a shear stress transducer in the sliding plate rheometer. *Journal of Non-Newtonian Fluid Mechanics*, 102(1):71–96, 2002.

[39] T Dealy J M Giacomin, A J Samurkas. A Novel Sliding Plate Rheometer for Molten Plastics. *Polymer Engineering and Science*, 29(8):499–504, 1989.

[40] Keiji Sakai, Taichi Hirano, and Maiko Hosoda. Electromagnetically spinning sphere viscometer. *Applied Physics Express*, 3(1):016602, 2010.

[41] Naoto Izumo. Physical quantity measurd by a vibration viscometer, 2006.

[42] K. L. McCarthy, R. J. Kauten, M. J. McCarthy, and J. F. Steffe. Flow profiles in a tube rheometer using magnetic resonance imaging. *Journal of Food Engineering*, 16(1-2):109–125, 1992.

[43] M. Spiga and G. L. Morino. A symmetric solution for velocity profile in laminar flow through rectangular ducts. *International Communications in Heat and Mass Transfer*, 21(4):469–475, 1994.

[44] Donald G. Baird and Dimitris I. Collias. *Polymer Processing : Principles and Design*. Wiley, 2 edition, 2014.

[45] Dianchuan Xing, Changqi Yan, Chang Wang, and Licheng Sun. A theoretical analysis about the effect of aspect ratio on single-phase laminar flow in rectangular ducts. *Progress in Nuclear Energy*, 65:1–7, 2013.

[46] Tariq Ahmad and Ibrahim Hassan. Experimental Analysis of Microchannel Entrance Length Characteristics Using Microparticle Image Velocimetry. *Journal of Fluids Engineering*, 132(4):041102, 2010.

[47] Sang-Youp Lee, Jaesung Jang, and Steven T. Wereley. Effects of planar inlet plenums on the hydrodynamically developing flows in rectangular microchannels of complementary aspect ratios. *Microfluidics and Nanofluidics*, 5(1):1–12, Jul 2008.

[48] F. Wang X Whiteley, J. Gordaninejad. Behavior of magneto-rheological fluids in microchannels. In *Electro-Rheological Fluids and Magneto-Rheological Suspensions*, pages 523–529, 2010.

[49] Jae Seop Ryu, Yingying Yao, Chang Seop Koh, and Young Jun Shin. 3-D optimal shape design of pole piece in permanent magnet MRI using parameterized nonlinear design sensitivity analysis. *IEEE Transactions on Magnetics*, 42(4):1351–1354, 2006.

[50] Arun Balakrishnan, William T. Joines, and Thomas G. Wilson. Air-gap reluctance and inductance calculations for magnetic circuits using a schwarz-christoffel transformation. *IEEE Transactions on Power Electronics*, 12(4):654–663, 1997.

[51] Mandy B. Esch, Sahil Kapur, Gizaida Irizarry, and Vincent Genova. Influence of master fabrication techniques on the characteristics of embossed microfluidic channels. *Lab on a Chip*, 3(2):121, 2003.

[52] Matthias Worgull. Chapter 3 - molding materials for hot embossing. In Matthias Worgull, editor, *Hot Embossing*, Micro and Nano Technologies, pages 57 – 112. William Andrew Publishing, Boston, 2009.

[53] Chia-Wen Tsao and Don L. DeVoe. Bonding of thermoplastic polymer microfluidics. *Microfluidics and Nanofluidics*, 6(1):1–16, Jan 2009.

[54] Sum Huan Ng, Ricky Tjeung, Z.F. Wang, A C. W. Lu, I Rodriguez, and N F. de Rooij. Thermally activated solvent bonding of polymers. *Microsystem Technologies*, 14(6):753–759, 2008.